

# Geometrical Structure of Small Scales and Wall-bounded Turbulence

Vom Fachbereich Maschinenbau an der Technischen Universität Darmstadt zur Erlangung des akademischen Grades eines Doktor-Ingenieurs (Dr.-Ing) genehmigte

DISSERTATION

vorgelegt von

Dipl.-Ing. Fettah Aldudak

aus Çermik, Türkei

Berichterstatter:	Prof. Dr.-Ing. Martin Oberlack
Mitberichterstatter:	Apl. Prof. Dr.-Ing. Suad Jakirlić
Tag der Einreichung:	31.01.2012
Tag der mündl. Prüfung:	20.03.2012

D17

Darmstadt, 2012



# Contents

<b>Nomenclature</b>	<b>10</b>
<b>1 Introduction</b>	<b>12</b>
1.1 Features of Turbulence . . . . .	12
1.2 Theory . . . . .	12
1.2.1 Richardson's Energy Cascade . . . . .	16
1.2.2 Kolmogorov's Theory . . . . .	17
1.3 Motivation . . . . .	22
<b>2 Direct Numerical Simulations</b>	<b>25</b>
2.1 Numerical Methods and Algorithms . . . . .	28
2.2 Simulations . . . . .	31
<b>3 Turbulent Channel Flow Statistics</b>	<b>32</b>
3.1 Velocity Profiles . . . . .	33
3.2 Turbulence Intensities . . . . .	38
3.3 Energy Dissipation Rate . . . . .	41
<b>4 Instantaneous Fields</b>	<b>44</b>
4.1 Vorticity . . . . .	44
4.2 Second Invariant of the Velocity Gradient . . . . .	45
<b>5 Length Scales in Turbulent Channel Flow</b>	<b>53</b>
5.1 Kolmogorov Length Scale . . . . .	55
5.2 Taylor Length Scale . . . . .	57
<b>6 Dissipation Element Analysis</b>	<b>59</b>
6.1 Plane Turbulent Channel Flow and Lie Group Analysis . . . . .	63
6.1.1 Validation of the Dissipation Element Scaling Laws . . . . .	68
6.1.2 Log-normal Pdf Model . . . . .	82
6.1.3 Conditional Mean of Scalar Differences . . . . .	87
6.2 Turbulent Channel Flow with Wall-normal Rotation . . . . .	93
6.3 Turbulent Channel Flow with Streamwise Rotation . . . . .	97
6.4 Turbulent Channel Flow with Wall Transpiration . . . . .	103

<b>7</b>	<b>Streamline Segments</b>	<b>108</b>
7.1	Numerical Algorithm . . . . .	108
7.2	Streamline Segment Statistics . . . . .	111
7.3	Conditional Mean Velocity Differences . . . . .	114
<b>8</b>	<b>Summary</b>	<b>118</b>
<b>A</b>	<b>Lie theory for dissipation elements in wall-bounded shear flows</b>	<b>121</b>
<b>B</b>	<b>Bibliography</b>	<b>123</b>

## ERKLÄRUNG

Hiermit erkläre ich, dass ich die vorliegende Arbeit, abgesehen von den in ihr ausdrücklich genannten Hilfen, selbstständig verfasst habe.

Fettah Aldudak

## Acknowledgements

The present thesis is a result of the research which has been conducted during my employment as a PhD student at the Chair of Fluid Dynamics at the TU Darmstadt, in the period of 2007 to 2011. Looking back at the time, I remember a beautiful era with nice colleagues from whom I benefited in many respects.

First of all, I would like to thank my supervisor Prof. Dr.-Ing. habil. Martin Oberlack for not only giving me the opportunity to work in a competent and pleasant environment and his great support but also for providing me enough freedom to follow my own ideas. Special thanks go to Apl.-Prof. Dr.-Ing. Suad Jakirlić for the willingness to be my co-referee.

I gratefully acknowledge the funding from the Deutsche Forschungsgemeinschaft (DFG) under grant number *OB96/19 – 1* within the research collaboration group *Geometric structure of small-scale turbulence*.

I want also thank Dr.-Ing. Sergio Hoyas for the great help with the DNS code and the hospitality during my stay in Valencia. Furthermore, I want to mention that I appreciate the constructive cooperation with Dr.-Ing. Lipo Wang and Jens Henrik Göbbert within the framework of the research collaboration. I also thank Ameeya Sharma for proofreading this manuscript.

I would like to offer my warmest thanks to my wonderful family. My parents deserve special mention for their priceless support I am blessed with ever since I can remember. Finally, I want to express my appreciation to my wife and my little daughter for their patience and constant support.

# Abstract

## English

Turbulence is observed in most technical and natural environments involving fluid motion. However, the theory behind is still not fully understood. Due to the irregular, complex character of turbulence, it is treated statistically since a deterministic approach is usually not possible.

Spatial structures in turbulence, known as eddies, are essential to describe the turbulent flow. In this thesis, a new method proposed by Wang & Peters (2006) is employed to decompose turbulent scalar fields completely and uniquely into small spatial sub-units. The approach is called Dissipation Element method. Gradient trajectories in the scalar field are traced in ascending and descending directions where they inevitably reach a minimum and a maximum point, respectively. All trajectories leading to the same pair of extremal points define a dissipation element (*DE*).

In the present work, *DE* analysis is extended to the canonical wall-bounded turbulent channel flow. Special focus will be given to the effect of the wall boundaries with respect to the size of the *DEs* and their distribution along the wall-normal direction of the channel. To obtain data for analysis, Direct Numerical Simulations (*DNS*) have been conducted at different Reynolds numbers as presented in chapter 2 following a brief introduction in §1. Turbulent channel flow statistics are discussed in §3 which are later addressed to interpret results from *DE* analysis. In chapter 4, three-dimensional turbulent structures, called vortices, are presented which are obtained with classical methods.

Classical turbulent length scales in Poiseuille flow are analyzed in §5 before the *DE* method is applied in chapter 6. Mean length of *DEs* and its variation with the distance from the wall will be addressed extensively. The influence of the Reynolds number and the choice of the scalar variable is discussed. Marginal, joint and conditional probability densities (*pdf*) of the Euclidean distance and scalar difference between extremal points are investigated. Employing Lie symmetry analysis, invariant solutions of the *pdf* are obtained. Further, a log-normal model for the *pdf* is derived. In

addition to the classical Poiseuille flow, three different channel flows are investigated by means of the *DE* method, namely channel flows with wall-normal and streamwise rotations and wall transpiration.

Finally, streamline segments are examined in chapter 7 with respect to the length and the velocity difference between their ending points. As in the case of *DEs*, marginal and conditional *pdfs*, as well as the influence of the wall-distance and Reynolds number are discussed.

## German

Turbulenz ist ein allgegenwärtiges Phänomen, das sich fast überall dort abspielt, wo Flüssigkeiten und Gase in Bewegung versetzt werden, und stellt doch einen der letzten Bereiche der klassischen Physik dar, dessen vollständige Erschließung bis heute aussteht. Aufgrund ihrer Komplexität erlauben turbulente Strömungen keinen deterministischen Lösungsansatz. Folglich stehen meist nur statistische Herangehensweisen zur Verfügung.

Bei der Beschreibung der Turbulenz kommt den darin enthaltenen Wirbelstrukturen, den sogenannten Eddies, eine Schlüsselrolle zu. Im Rahmen dieser Dissertation kommt eine neuartige Methode zum Einsatz, die das skalare Turbulenzfeld vollständig und, was noch wichtiger ist, eindeutig in kleinere räumliche Strukturen aufteilt. Die Methode heißt Dissipations-Elemente-Methode und nutzt Gradiententrajektorien, die unweigerlich zu einem Minimal- und Maximalpunkt führen. Sämtliche zu einem bestimmten Extrempunkte-Paar gehörigen Trajektorien bilden ein sogenanntes Dissipations-Element (*DE*). Die Methode wurde erstmals von Wang & Peters (2006) eingeführt und von den Autoren vor allem in Zusammenhang mit homogener Scherströmung eingesetzt.

Im Gegensatz dazu wird in dieser Arbeit eine wandgebundene turbulente Kanalströmung Gegenstand der Untersuchung sein. Besonderes Augenmerk gilt dabei dem Einfluss fester Wände auf die Länge und räumliche Verteilung von Dissipations-Elementen. Die für die *DE*-Analyse erforderlichen Daten werden mit Hilfe von DNS (Direkte Numerische Simulationen) gewonnen, die im Anschluss an eine kurze Einführung (§1) vorgestellt werden (Kapitel 2). In Kapitel 3 werden die turbulente Kanalströmung und ihre Statistiken behandelt, die im späteren Verlauf bei der Interpretation von Ergebnissen aus der *DE*-Analyse herangezogen werden. Anschließend werden in §4 räumliche turbulente Strukturen vorgestellt.



In §5 werden Längenskalen der Turbulenz behandelt, bevor die angekündigte DE-Methode in Kapitel 6 erläutert wird. Die mittlere Länge der Elemente und ihre Verteilung in wand-normaler Richtung werden ausgiebig diskutiert. Dabei werden sowohl unterschiedliche Reynolds-Zahlen als auch Skalarvariablen berücksichtigt.

Mit Hilfe von Lie-Symmetrie-Methode werden invariante Lösungen der Wahrscheinlichkeitsdichte der DE-Längenskala hergeleitet. Wahrscheinlichkeitsdichtefunktionen (pdf) der Länge und Skalar differenzen zwischen den Extrempunkten werden ausgewertet, und ein log-normales Modell für die marginale pdf vorgestellt. Drei weitere Konfigurationen der Kanalströmung werden ergänzend zur klassischen Poiseuille-Strömung untersucht, nämlich Kanalströmungen mit Wandtranspiration und mit Rotation in Strömungs- und wand-normaler Richtung.

Abschließend werden Stromliniensegmente hinsichtlich ihrer Länge und Geschwindigkeitsdifferenz an den Endpunkten analysiert. Ähnlich wie bei *DEs* werden marginale und konditionierte pdfs analysiert und der Einfluss des Wandabstandes als auch der Reynolds-Zahl ausgewertet.

# Nomenclature

$+$	superscript denoting wall, or inner scaling
$\ell$	length of a dissipation element / streamline segment
$\ell_m$	mean element length
$\epsilon$	rate of kinetic energy dissipation
$\eta$	Kolmogorov length scale
$\lambda$	Taylor length scale
$\nu$	kinematic viscosity
$\omega_x, \omega_y, \omega_z$	vorticity components
$\Phi$	scalar variable
$\tilde{P}$	invariant <i>pdf</i>
$CL$	centerline
$D$	molecular diffusivity
$DE$	dissipation element
$DNS$	Direct Numerical Simulation
$h$	channel half height
$k$	turbulent kinetic energy
$L$	integral length scale
$MPC$	multi-point correlation
$N$	number of grid points

$P$	<i>pdf</i> of the element length
<i>pdf</i>	probability density function
$Pr$	Prandtl number
$Q$	second invariant of the velocity gradient
$Re$	Reynolds number
$Re_\lambda$	Reynolds number based on Taylor length scale
$Re_\tau$	Reynolds number based on friction velocity
$S_{ij}$	symmetric rate-of-strain tensor
$u_\eta$	Kolmogorov velocity
$u_\tau$	friction velocity
$u_{rms}$	root-mean-square of a fluctuating velocity
$W_{ij}$	skew-symmetric rate-of-rotation tensor
$y^+$	wall-normal coordinate, made dimensionless with $\nu/u_\tau$

# 1 Introduction

## 1.1 Features of Turbulence

Turbulence is one of the most challenging and, at the same time, fascinating phenomena provided by physics. It plays a fundamental role in most flows occurring in nature and technical applications. Air flow in the atmosphere of the Earth, river and ocean currents as well as the flows in the wakes of aircrafts, cars and ships are turbulent. Turbulence is undesirable, e.g., when it results in an increment of aerodynamic drag of a vehicle, but useful for mixing the air and the fuel to ensure a more efficient burning in a combustion chamber.

Although the balance equations describing turbulent motion have been independently introduced by Claude Louis Marie Henri *Navier* (1785-1836) and George Gabriel *Stokes* (1819-1903) more than 150 years ago, it still remains one of the biggest unsolved problems of the physics. While a deterministic approach to the Navier-Stokes equations is possible for laminar flows, turbulent flows with random fluctuations permit only the use of statistical methods. Turbulence requires sufficiently high Reynolds numbers where non-linear convective forces overcome viscous forces. In addition, all turbulent flows share several features. They are always irregular, time dependent, rotational, three-dimensional, highly diffusive, dissipative and non-local. With increasing Reynolds number, turbulence becomes more chaotic. Nevertheless, in this seemingly disorganized turbulent state there exist organized spatial structures called coherent structures, e.g., hairpin vortices in the boundary layer flow.

## 1.2 Theory

To study the evolution of fluid variables, such as velocity, energy, temperature and chemical concentrations the fluid can be modeled as finite fluid particles with freedom to translate, rotate and deform. With the *Lagrangian* and *Eulerian* description there exist two formulations to describe the fluid

motion. Lagrangian description is typically used in flows where fluid particles need to be traced, e.g., flows with solid particles and bubbles. On the contrary, Eulerian description does not follow the fluid particles, but considers the flow through a fixed spatial domain. The Eulerian description is used most frequently and is also adopted in the present work.

Fluids obey the laws of conservation of energy, mass and momentum according to the general laws of continuum mechanics. Conservation of mass, energy and momentum are the laws of continuum mechanics which describe fluid motion.

The conservation equations for continuity (1.1) and momentum (1.2) specify the Navier-Stokes equations,

$$\nabla \cdot \mathbf{U} = 0, \quad (1.1)$$

$$\frac{D\mathbf{U}}{Dt} = \frac{\partial \mathbf{U}}{\partial t} + (\mathbf{U} \cdot \nabla) \mathbf{U} = -\frac{1}{\rho} \nabla p + \nu \nabla^2 \mathbf{U} + \mathbf{f}, \quad (1.2)$$

where  $x$ ,  $t$ ,  $\mathbf{U}$  and  $p$  are the position vector, time, the velocity vector and pressure. The kinematic viscosity  $\nu$  is the ratio of the dynamic viscosity  $\mu$  to the density  $\rho$  describing the resistance of a sheared fluid against deformation. Assuming constant density, the set of these equations represents the fluid motion of an incompressible Newtonian fluid.

The expression  $D\mathbf{U}/Dt$  in Eq. 1.2, called the *material derivative*, is the time rate of change following a fluid element and consists of a *temporal* and a *convective* term. The non-linear, convective term denotes the transport of the quantity due to fluid motion in general, and the acceleration of the fluid particle if the velocity vector is regarded. Unlike the convective transport which is due to the macroscopic fluid velocity, the *diffusion* transport is caused by the random motion of fluid molecules at microscopic level. It is represented by the term  $\nu \nabla^2 \mathbf{U}$  involving the viscosity  $\nu$  that is responsible for the resistance of the fluid to the flow. Viscosity, thus, produces friction between the layers of the fluid due to the relative motion of the particles. In *Newtonian* fluids, where the viscous stress and the deformation rate are linearly related, viscosity is a function of temperature only and independent of shear rate.

The term  $\mathbf{f}$  in Eq. 1.2 refers to forces that act upon fluid particles, namely *body forces*, *surface forces* and *surface tension*. Gravity, for instance, is a typical body force without direct contact to the fluid volume. As such, it differs from surface forces exerted to the surface of the fluid domain like pressure or friction.

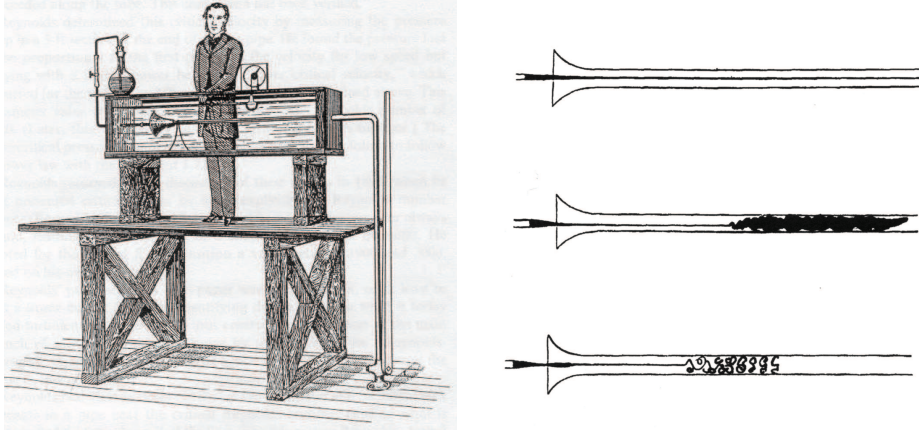


Figure 1.1: Reynolds' experiment on the transition from laminar to turbulent flow in pipes.

Handling the Navier-Stokes equations, or in other words, the problem of turbulence is a very big challenge. The equations are nonlinear because of the advection term and nonlocal due to the pressure contribution. Exact solutions are possible only with the aid of simplifications which are often problematic from the point of view of physics.

Osborne Reynolds (1883) was the first to systematically study the transition process of fluid flow in a pipe. In the wake of these experiments, he introduced the dimensionless Reynolds number ( $Re$ ) as the ratio of inertial forces to viscous forces

$$Re = \frac{UL}{\nu}, \quad (1.3)$$

using a characteristic velocity  $U$ , a typical length scale  $L$  and the kinematic viscosity  $\nu$ . These quantities are also used to obtain the dimensionless form of the Navier-Stokes equations.

$$\frac{\partial \mathbf{U}}{\partial t} + (\mathbf{U} \cdot \nabla) \mathbf{U} = -\nabla p + \frac{1}{Re} \nabla^2 \mathbf{U} + \mathbf{f}. \quad (1.4)$$

The inverse of  $Re$  is introduced into the dimensionless Navier-Stokes equations (1.4) as prefactor of the viscous term. Thus, increasing  $Re$  damps the influence of the dissipation term boosting turbulence intensity.  $Re$  of a flow must exceed an individual critical number to cause transition from laminar to turbulent state, e.g.  $Re_{crit} \approx 2300$  in a pipe flow with the diameter as  $L$ .

Turbulent quantities are characterized by chaotic fluctuations which are superimposed on mean values. These instantaneous quantities can be decomposed into a time-averaged and a fluctuating part which is called *Reynolds decomposition*,

$$\mathbf{U}(\mathbf{x}, t) = \overline{\mathbf{U}}(\mathbf{x}) + \mathbf{u}(\mathbf{x}, t) , \quad (1.5)$$

with  $\overline{\mathbf{u}}(\mathbf{x}, t) \equiv 0$ , indicating that the average of velocity fluctuations must vanish (see Figure 1.2). The same rule applies to the pressure variable  $p$ . In index notation, velocity and space vectors can be expressed as  $U_i$  and  $x_i$ , respectively. Together with other Reynolds operators the above relation can be used to arrive at the *Reynolds-Averaged Navier-Stokes (RANS)* equations in final form as follows:

$$\rho \frac{\partial \overline{U}_i}{\partial t} + \rho \overline{U}_j \frac{\partial \overline{U}_i}{\partial x_j} = \rho \overline{f}_i + \frac{\partial}{\partial x_j} \left[ -\overline{p} \delta_{ij} + \mu \left( \frac{\partial \overline{U}_i}{\partial x_j} + \frac{\partial \overline{U}_j}{\partial x_i} \right) - \rho \overline{u_i u_j} \right] , \quad (1.6)$$

$$\frac{\partial \overline{U}_k}{\partial x_k} = 0 . \quad (1.7)$$

As a result of this procedure, the additional term  $\rho \overline{u_i u_j}$ , the so-called *Reynolds stress (RS) tensor*, arises from averaging the nonlinear advection term in the momentum equations.  $\overline{u_i u_j}$  is a second order symmetric tensor such that  $\overline{u_i u_j} = \overline{u_j u_i}$  with  $i, j = 1, 2, 3$ . The diagonal components  $\overline{u_i^2}$  denote the *normal stresses* of the RS tensor whereas the remaining off-diagonal components  $\overline{u_i u_j}$  ( $i \neq j$ ) are known as the *shear stresses*. The turbulent kinetic energy  $k$  is proportional to the sum the of normal stresses as

$$k = \frac{1}{2} \overline{u_i u_i} . \quad (1.8)$$

*RS* tensor can be understood as the influence of velocity fluctuations on the mean flow. However, this term is unknown, so further equations must be provided to close the problem. One attempt in this regard is to generate an equation for the velocity fluctuations  $u_i$  by subtracting the *RANS* equations from the Navier-Stokes equations. Unfortunately, in doing so, one realizes that now third order moments of fluctuations emerge. Theoretically, such a hierarchy might be continued further to obtain moments of order  $N$ . However, using this method, the moments of order  $N+1$  will

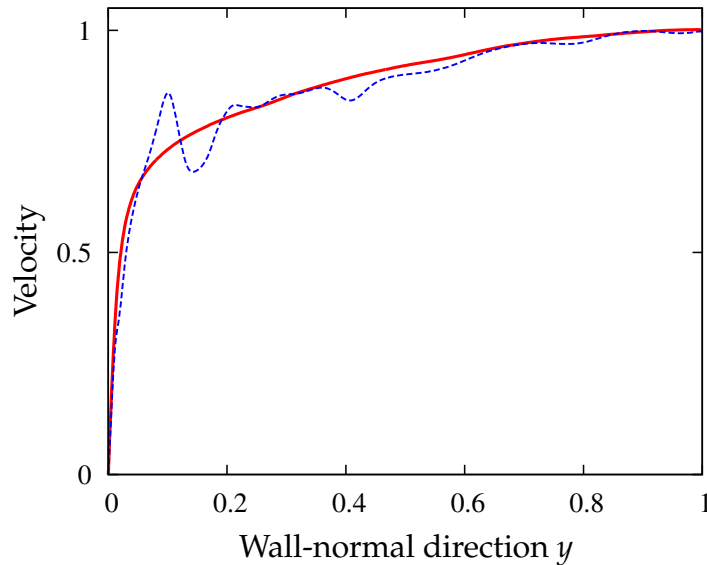


Figure 1.2: Instantaneous (dashed line) and mean (solid line) velocity profiles in turbulent channel flow.

always remain unknown. This is known as the *closure problem of turbulence*.

A more practical option to overcome this difficulty is introducing empirical assumptions in order to model the unknown moments. Today, owing to permanent development in the turbulence modeling community, there are a vast variety of models available. Some of these enjoy great popularity, especially in industrial fields. Notwithstanding, one must recall that none of these models can be directly attributed to the Navier-Stokes equations, but rather they are phenomenological assumptions.

The concept of Reynolds equations has been successfully applied to e.g. the similarity hypothesis by *von Kármán*, the mixing length approach by *Prandtl* and the *Boussinesq* approximation of the eddy viscosity, to name only a few.

### 1.2.1 Richardson's Energy Cascade

Richardson (1922) established a cascade theory according to which turbulent flows are composed of spatial structures of different sizes. This



cascade contains all length scales between the integral ( $L$ ) and the Kolmogorov ( $\eta$ ) length scales where

$$\eta = \left( \frac{\nu^3}{\epsilon} \right)^{1/4} . \quad (1.9)$$

Here,  $\epsilon$  is the dissipation rate of energy defined as

$$\epsilon = \frac{1}{2} \nu \left( \frac{\partial u_i}{\partial x_j} + \frac{\partial u_j}{\partial x_i} \right)^2 . \quad (1.10)$$

These structures are unstable and break into eddies of smaller size. Their kinetic energy, which is extracted from the mean flow, is distributed to these smaller eddies - not necessarily in equal parts. The latter are also unstable and break up as well.  $Re$  is assumed to be high enough to neglect the influence of the dissipation term. This process of energy transfer continues successively towards smaller elements until the dissipative Kolmogorov scale  $\eta$  is reached. Here, the kinetic energy is dissipated into heat due to the effect of molecular viscosity. There exists a balance of energy flux between the large and smallest scales. Under the equilibrium conditions in the inertial subrange, the rate of energy transfers between the energy containing and the dissipation range is equal to the *dissipation rate*  $\epsilon$ .

*Richardson's* approach has been confirmed by many experiments and is an inherent part of the turbulence theory.

## 1.2.2 Kolmogorov's Theory

Based on *Richardson's* concept of an energy cascade, Kolmogorov (1941)<sup>1</sup> formulated new hypotheses to derive statistical conclusions about fully-developed, homogeneous isotropic turbulence (hereinafter referred to as *K41*). In spite of the restricted validity his so-called *similarity hypotheses* are an outstanding contribution to the understanding of the turbulence theory.

Turbulent motion is anisotropic at large scales. For sufficiently high  $Re$ , *K41* postulates that the anisotropic character of these motions is reduced

---

<sup>1</sup>Andrey Nikolaevich Kolmogorov, (25 April 1903 - 20 October 1987), Soviet mathematician

gradually during the process of the energy transfer, hence reaching a statistically isotropic state after a sufficient number of cascade steps. At this isotropic level, turbulent motions lose their preferred spatial direction. This is known as the ***local isotropy hypothesis***.

### ***First similarity hypothesis***

*K41* implies that, besides the directional information, basically all geometrical information are lost which means that they are independent of the boundary conditions and the mean flow field. In other words, in every turbulent flow at high *Re* statistical properties associated with the small scales of the velocity field will feature a universal form that is uniquely determined by  $\nu$  and  $\epsilon$ . With dimensional analysis, one can obtain Kolmogorov length (equation 1.9), velocity and time scales using  $\nu$  and  $\epsilon$ .

$$u_\eta = (\epsilon\nu)^{1/4} \quad (1.11)$$

$$\tau_\eta = \left(\frac{\nu}{\epsilon}\right)^{1/2} \quad (1.12)$$

Once rescaled with the Kolmogorov scales, statistical properties of small scales in any turbulent flow will be identical. The Kolmogorov Reynolds number reads  $Re_\eta = (u_\eta\eta)/\nu = 1$ .

### ***Second similarity hypothesis***

Energy is injected into a turbulent flow at large scales  $L$ . In fully-developed flows, the energy cascade contains a broad spectrum of scales which are smaller than  $L$  but considerably larger than  $\eta$ . Thus, *Re* of these intermediate scales  $\ell$  is large and independent of the viscosity. Accordingly, Kolmogorov's second similarity hypothesis states that statistics of turbulent motions of scale  $\ell$  (where  $L \gg \ell \gg \eta$ ) are universal and depend on  $\epsilon$  only - but not on  $\nu$ . This intermediate range is called the *inertial subrange*.

One of the most significant findings from Kolmogorov theory is the energy spectrum within the inertial subrange,

$$E(\kappa) = C_2 \epsilon^{2/3} \kappa^{-5/3} , \quad (1.13)$$

with  $\kappa$  being the wavenumber. This relation has been verified through many experiments. According to *K41*,  $C_2$  denotes a universal constant

to be defined via experiments. *Structure functions* are another outcome stemming from dimensional considerations which are defined for a spatial distance  $r$ ,

$$S_q(r) = \langle \Delta u(r)^q \rangle = \int_{-\infty}^{\infty} P(\Delta u) \Delta u^q d(\Delta u) , \quad (1.14)$$

where  $\Delta u$  is the velocity increment between two points and  $P(\Delta u)$  is their probability distribution function. Following Kolmogorov's postulate together with dimensional analysis, one yields for high  $Re$

$$S_q(r) = C_q (\epsilon r)^{q/3} . \quad (1.15)$$

For second order structure function ( $q=2$ ) we arrive at an equivalent form of equation 1.13. Additionally, the structure function of order three may be inferred as

$$S_3(r) = -\frac{4}{5}\epsilon r \quad (1.16)$$

where  $\epsilon r$  has the same dimension as  $S_3$ , ensuring that  $C_3$  must be an obviously universal constant as can be obtained from the *von Kármán-Howarth* equation (Frisch (1995)).

### ***Refined Similarity Hypothesis***

Even though, equation 1.15 shows a good agreement for exponents up to  $q = 3$ , higher order structure functions expose distinct deviations for higher  $q$  suggesting some inconsistency of *Kolmogorov's* theory with real turbulence. In fact, in this case, the actual scaling exponents are smaller than  $p/3$  of *K41*, which is an indication of a variable *pdf*  $P(\Delta u)$  assigned to the inertial subrange. In this view, the supposed universality of the constants  $C_q$  must also to be questioned. Except for  $C_3$  from the equation 1.16, there is no evidence for a universal character of  $C_q$ .

The reason for the shortcoming of *K41* is that these hypotheses ignore the effect of spatial intermittency of the dissipation rate. *K41* assumes a constant energy transfer rate  $\epsilon$ , such that the energy transfer to smaller eddies should be in equal parts. However, this is clearly not the case. Furthermore, the energy and its dissipation rate vary in time and space by orders of magnitude which are even more pronounced at higher  $Re$ . Figure 1.4

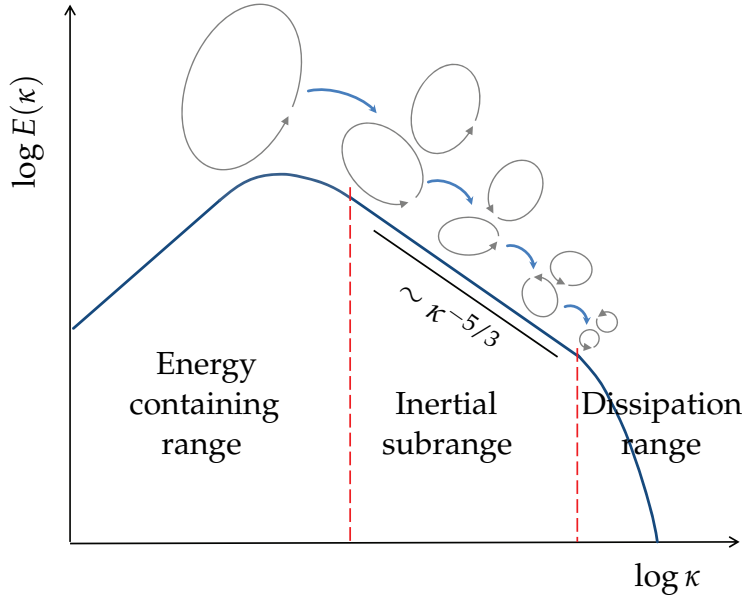


Figure 1.3: Energy cascade.

shows instantaneous, local distributions of  $\epsilon$ ,  $k$  and  $u$  along a line in the DNS case 2 (see table 2.1). In contrast to the fluctuation of the stream-wise velocity  $u$ , the plots of the quantities  $\epsilon$  and  $k$  have regions of very high intensity in close proximity of low intensity areas, revealing their intermittent character. This may be a reason for the anomaly of the scaling exponents in equation 1.15.

Accordingly, the intermittency effects in turbulence need to be accounted for, which led *Kolmogorov* to propose his so-called *Refined Similarity Hypothesis (RSH)* in the work *Kolmogorov (1962)*. He postulates a log-normal model of fluctuations of the local dissipation rate in a fluid volume ( $\sim r$ )  $\epsilon_r$  as shown below.

$$P(\epsilon_r) = \frac{1}{\epsilon_r \sigma_r \sqrt{2\pi}} \exp \left( -\frac{\left( \ln \left( \frac{\epsilon_r}{\bar{\epsilon}} \right) + \frac{\sigma_r^2}{2} \right)^2}{2\sigma_r^2} \right) \quad (1.17)$$

$\sigma_r$  is the standard deviation of the mean dissipation rate dependent on the scale  $r$  with

$$\sigma_r \sim -\mu \ln(r) . \quad (1.18)$$

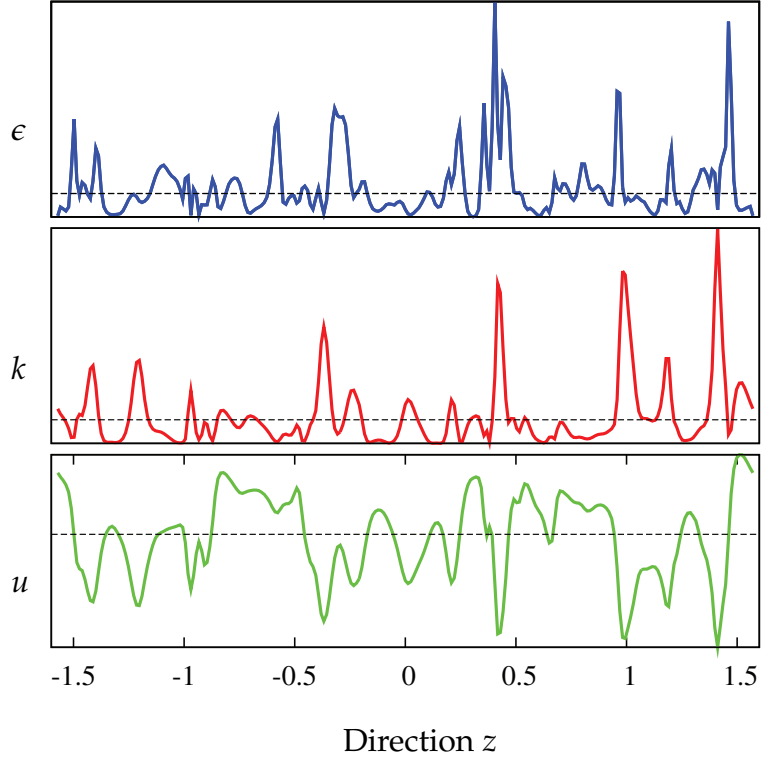


Figure 1.4: Instantaneous profiles along a spanwise line with the corresponding mean values (dashed lines).

where  $\mu$  is an empirical constant, called the intermittency factor. With this refinement, i.e. using equations 1.17 and 1.18, a correction term  $\Delta_q$  is introduced to the scaling exponent  $q/3$  as

$$\Delta_q = -\frac{\mu}{18}q(q-3), \quad (1.19)$$

hence,

$$\zeta_q = \frac{q}{3} - \frac{\mu}{18}q(q-3). \quad (1.20)$$

Compared to *K41*, the non-linear *RSH* scaling brings about significant improvements. However, note that the *RSH* scaling (1.20) cannot be strictly valid because it will take negative values for large  $q$  which is seen as non-physical. In figure 1.5 both Kolmogorov linear and refined scaling predictions are compared with experimental data from Benzi, Ciliberto, Tripiccone, Baudet, Massaioli & Succi (1993) up to structure function of order eight with rather good agreement with the refined scaling law.

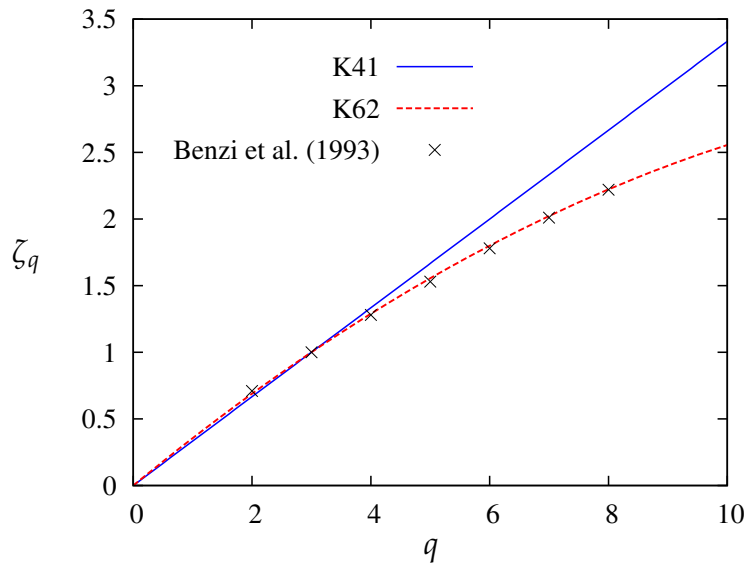


Figure 1.5: Scaling exponents  $\zeta_q$  as predicted by *Kolmogorov* in comparison with experimental data (crosses) from *Benzi et al.* (1993).

Although *Kolmogorov's* great contribution to the turbulence theory is undisputed, there are some legitimate objections. His hypotheses remain basically heuristic because a direct derivation from first principles is still missing.

### 1.3 Motivation

An important aspect of turbulence is the rich variety of the turbulent motions contained therein. Hence, it is essential to identify these structures, also referred to as *eddies*, and the interplay between them. Accordingly, great efforts have been made to investigate the geometrical structures of turbulence in order to acquire statistical information. Most popular approaches use different quantities of turbulence to isolate spatial structures, the so-called *vortices*. The main deficiency accompanied by such a procedure is the lack of a clear, self-contained definition of the shape of these vortices. Hence, the definition depends on the choice of certain random parameters and remains arbitrarily. In chapter 4, some approaches to identify vortical structures will be presented.

The alternative to this would be a method according which the turbulent flow field is decomposed into small subunits using non-arbitrary conditions which result directly from the physics of the flow. One very interesting approach in this respect was the work by Gibson (1968) who investigated the generation of critical points in turbulent scalar fields. Inspired by his idea, Wang & Peters (2006) proposed the method of *Dissipation Elements (DE)* where critical points in turbulent scalar fields are used to define spatial structures called dissipation elements. Gradient trajectories starting from any point in the turbulent field in the directions of ascending and descending scalar gradient will always reach a pair of extremal points, i.e. maximal and minimal points. For details on the tracing algorithm see Wang & Peters (2008). A dissipation element is defined by all trajectories belonging to the same pair of critical points. In a smooth turbulent field, this approach ensures a space-filling and unique decomposition of the scalar field without elements overlapping each other. *DE* method can be applied to any turbulent scalar quantity such as the components of the velocity and vorticity, turbulent kinetic energy and its dissipation rate.

In §6, this method is adopted to investigate the geometrical structures in wall-bounded turbulent channel flows. Main focus will be on the classical turbulent Poiseuille flow. Moreover, three different types of channel flow are investigated additionally, namely channel flows with rotation in streamwise and wall-normal directions and channel flow with wall transpiration. For this, various *Direct Numerical Simulations (DNS)* have been performed to obtain data to be analyzed with the *DE* method which are presented in §2. In chapter 3, statistics of wall-bounded turbulent flow are discussed which are referenced as needed to interpret the results from *DE* analysis. Parts of the chapters 5 and 6 have been published in Aldudak & Oberlack (2012).

The scalar difference  $\Delta\phi$  and the Euclidean linear length  $\ell$  between the extremal points are used to construct statistics such as the marginal, conditional and joint probability density functions *pdf*. The distribution of *DE* length scales and the scaling behavior of the scalar differences will be the subject of discussion. The influence of the Reynolds number, the choice of the scalar variable and not least the distance from the wall boundary will be examined in detail. A log-normal *pdf* model is derived for the *DE* length taking into account the mentioned parameters of influence. *DE* analysis is extended by the Lie group analysis which has been proved to be an effective tool to derive new scaling laws. Employing group theoretical methods and known symmetries of Navier-Stokes equations, it will be shown that, sufficiently far from the wall, the *pdf* of *DE* length exhibits

an invariant functional form, in other words, self-similar behavior with respect to the wall distance.

With the streamline segment analysis in §7, a different approach is used to study the length scales in turbulent channel flow. Here, streamlines are divided into segments bounded by zero-gradient points of the velocity magnitude with respect to the curvilinear streamline coordinate  $s$ . Again, *pdfs* and scalar differences are investigated, analogous to *DE* method.



---

## 2 Direct Numerical Simulations

The highly complex nature of turbulence is described by the Navier-Stokes equations (1.1, 1.2). However, in the absence of proper analytical tools for solving this set of equations, numerical methods remain the only option to describe a turbulent flow. The use of such numerical methods is aggravated by the complexity of the flow geometry and the increase of the Reynolds number resulting in a wider spectrum of spatial and temporal scales in turbulence. Fluid flows relevant to industrial applications can only be calculated by means of e.g. *Reynolds-averaged Navier-Stokes (RANS)* and, increasingly, *Large Eddy Simulation (LES)* methods, which, to different degrees, make use of empirical turbulence models to reduce computational cost. While in *RANS* method all turbulent scales are modeled, in *LES* only small, isotropic scales have to be modeled whereas the remaining larger scales are resolved providing more accuracy, yet at higher computational cost. Contrarily, *Direct Numerical Simulation (DNS)* abandons turbulence modeling and solves the Navier-Stokes equations directly. Thus, it is superior to other approaches in terms of accuracy. In this case, however, all spatial and temporal scales of the turbulence, ranging from the smallest Kolmogorov scales to the large integral scales, must be resolved. Accordingly, the associated computational effort for DNS is very high which makes it still far from being practical for most engineering problems. Its application is limited to canonical flows in simple geometries, such as channel and pipe flows, at relatively low Reynolds numbers. Notwithstanding, DNS is very prevalent in fundamental research of turbulence allowing access to information that are sometimes difficult or even impossible to obtain from real experiments. DNS is also subject of the present work and will be highlighted below.

The first DNS of a plane channel flow has been performed by Kim, Moin & Moser (1987), although it was already used earlier for 3D homogeneous and isotropic turbulence (see Orszag & Patterson (1972), Rogallo (1981)). Since then, a number of modified channel flow configurations could be studied such as wall-bounded flows with rough solid boundaries, rotation, transpiration and heat transfer, to name but a few. The largest DNS

so far were performed by Kaneda & Ishihara (2006) for homogeneous flow and by Hoyas & Jiménez (2006) for channel flow.

The growing availability of computational resources combined with invention of new efficient numerical methods will likely give rise to a broader use of DNS. Since DNS is the underlying method which was used to obtain data about inhomogeneous turbulence for further analysis, a brief discussion is presented in the following.

Basically, the spatial and temporal scales are strongly influenced by the geometry and the Reynolds number of the turbulent flow. As a consequence, DNS is required to meet certain resolution conditions, depending on the physics of the flow, in order to resolve these scales accurately. The spatial dimensions of the flow domain must be chosen large enough to account for the energy-containing, large eddies which contribute most to the turbulent kinetic energy. Those scales (integral length scale  $L$ ) are usually in the order of flow geometry.

At the same time, the size of the numerical grid  $\Delta x$  has to be small enough to resolve the Kolmogorov scales  $\eta = (\nu^3/\epsilon)^{1/4}$ . Kolmogorov scales, the smallest scales of turbulence, are assumed to be universal and isotropic. Thus, they depend solely on the dissipation rate  $\epsilon$  and the kinematic viscosity  $\nu$ .

Depending on which kind of statistics are of interest, a coarser grid can be sufficient. Given the fact that  $\eta$  underestimates the small scales to be resolved, which are slightly larger, e.g. Yeung & Pope (1989) considers  $\Delta x/\eta = 3$  as adequate for low-order velocity statistics. Nevertheless, the resolution condition  $\Delta x \leq \eta$  remains crucial if a high-resolution DNS is aimed for.

In an analogous manner, time scales in turbulence influence the temporal resolution, i.e. the advancing of the solution in time. The time step cannot be chosen arbitrarily, since the numerical accuracy and the stability of the solution may be affected. A fluid particle is allowed to move only a fraction of the grid distance to avoid errors being introduced to small scales. Pope (2000) states that the time step must satisfy the *Courant number*

$$\frac{\sqrt{k} \Delta t}{\Delta x} = \frac{1}{20}. \quad (2.1)$$

Choi & Moin (1994) concludes that the computational time step must be less than the Kolmogorov time scale to maintain turbulence. Too large time steps are reported to result in laminarization of the flow. From this

it becomes evident that increasing the spatial resolution involves smaller time steps which, in turn, means an increase of required computation time.

Bearing these restrictions in mind, the relevant aspect of the computational effort of a DNS can be estimated for the case of homogeneous isotropic turbulence. For wall-bounded turbulent flows the need for computation resources is even more stringent considering the necessarily small grid spacing towards the wall. The number of degrees of freedom depends on the Reynolds number and is proportional to the ratio between integral and Kolmogorov scales,  $L/\eta \sim Re^{3/4}$ .  $Re$  is the Reynolds number based on the integral length scale. Hence, the number of grid points for three-dimensional computation scales with  $Re^{9/4}$ . Taking into account the CFL constraint the total computational effort is in the order of  $Re^3$ .

The Navier-Stokes equations (1.1, 1.2) are valid for any incompressible flow. Therefore, *boundary and initial conditions* of the flow have to be specified additionally for the system to be definite. Physical boundaries are specified by natural conditions, i.e. solid walls with no-slip condition, while artificial boundaries, such as the *periodic boundaries*, must be approximated appropriately. Periodic boundary conditions (PBC) are realized by equalizing two different boundaries to simulate only a fraction of a large system in order to reduce computational costs. In DNS of turbulent flows they are common practice because in this way the number of the degrees of freedom can be diminished drastically. Also, if desired, inflow and outflow boundaries can be avoided by this means as is the case in the present work. Other BCs include the *Dirichlet* and *Neumann* boundary conditions. The former specifies the actual value of the variable on the surface whereas the latter gives its normal derivative. In plane turbulent channel flow no-slip BC applies to the walls at which the fluid clings to and moves with the walls. If the wall is at rest and impermeable the fluid velocity vanishes at this boundary. Regarding the pressure at the wall, the Neumann BC applies.

In general, turbulence is unsteady and highly dissipative. Nevertheless, one can assume that the simulation reaches a quasi-stationary state if the simulation time is sufficiently long. A carefully chosen initial field for DNS improves the simulation process considerably. One way to do this is to use an instantaneous fully-developed DNS field that has been obtained from other simulations. Thus, in the new initial field Reynold number, numerical degrees of freedom and the channel size can be changed. This method was used in this work with two different spectral codes (for details see Lundbladh, Berlin, Skote, Hildings, Choi, Kim & Henningson (1999),

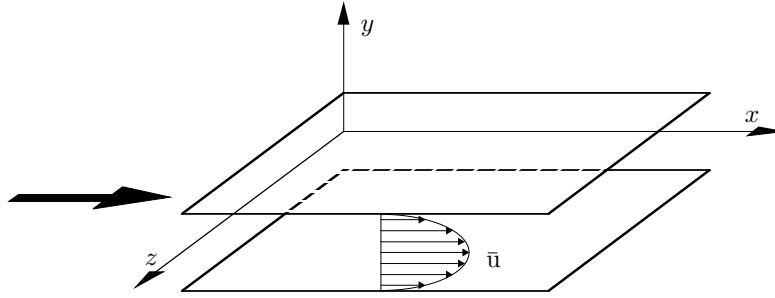


Figure 2.1: Sketch of the channel flow geometry.

Skote (2001) and Hoyas & Jiménez (2006)) to calculate several cases of turbulent plane Poiseuille flow. For this purpose, data in Fourier space from the old field is mapped to the wavenumbers of the new one. Given that the new field contains more Fourier modes, remaining wavenumbers are simply filled with zeroes. After an initial recovering phase due to the transition, which is excluded from the statistics, the solution approaches the new fully-developed state.

## 2.1 Numerical Methods and Algorithms

We investigate a pressure driven incompressible turbulent channel flow (see figure 2.1) employing the Navier-Stokes equations in the dimensionless form

$$\frac{\partial \mathbf{U}}{\partial t} + (\mathbf{U} \cdot \nabla) \mathbf{U} = -\nabla p + \frac{1}{Re} \nabla^2 \mathbf{U}, \quad (2.2)$$

$$\nabla \cdot \mathbf{U} = 0, \quad (2.3)$$

where  $x$ ,  $t$ ,  $\mathbf{U}$  and  $p$  are respectively the position vector, time, the velocity vector and pressure. All quantities have been non-dimensionalized by the channel half width  $h$  and the friction velocity  $u_\tau = \sqrt{\tau/\rho}$  where  $\tau$  is the mean wall friction,  $\rho$  is density and  $Re_\tau = u_\tau h/\nu$  is the friction based Reynolds number. With this the no-slip and impermeable wall boundary conditions at both channel walls read  $\mathbf{U}(x, y = \pm h, z) = 0$ . In the homogeneous streamwise ( $x$ ) and spanwise ( $z$ ) directions periodic boundary conditions are applied and the pressure gradient in  $x$ -direction that drives the flow is fixed to  $-1$ . The velocities in the streamwise, wall-normal and spanwise directions are respectively denoted by  $\mathbf{U} = (U, V, W)$ .

The first numerical code employed here uses well-established highly accurate spectral methods to solve the three-dimensional time-dependent incompressible Navier-Stokes equations and was developed at KTH, Stockholm (for details see Lundbladh et al. (1999) and Skote (2001)). The code adopts a spectral method with Fourier decomposition in the streamwise and spanwise directions and discretization with Chebyshev polynomials in the wall normal direction. Apart from the wall-normal integration the numerical method is similar to the one used by Kim et al. (1987). Time integration is performed using a third-order Runge-Kutta scheme for the advective and forcing terms and second-order Crank-Nicolson for the viscous terms. The transformation between physical and spectral space is done by Fast Fourier Transform (FFT).

A second code has been used to perform calculations with higher numerical resolution and Reynolds number (for details see Hoyas & Jiménez (2006)). This code employing high-order compact finite differences in the wall-normal direction provides more flexibility in the distribution of the collocation points in this direction. Further, since it is MPI-parallelized, more processors can be included in the computation.

The code integrates evolution equations for the wall-normal component of vorticity  $\omega_y$  and for the Laplacian of the wall-normal velocity  $\varphi = \nabla^2 v$ . With the relations for vorticity  $\boldsymbol{\omega}$  and the helicity  $\mathbf{H}$

$$\boldsymbol{\omega} = \nabla \times \mathbf{U} = (\omega_x, \omega_y, \omega_z) , \quad (2.4)$$

$$\mathbf{H} = (\mathbf{U} \times \boldsymbol{\omega}) - \frac{1}{2} \nabla (\mathbf{U} \cdot \mathbf{U}) = (H_1, H_2, H_3) , \quad (2.5)$$

the velocity-vorticity formulation of the Navier-Stokes equations can be obtained from 1.2 and 1.1 consisting of a fourth-order equation for  $v$ , and a second-order equation for  $\omega_y$  as follows:

$$\frac{\partial \varphi}{\partial t} = h_v + \frac{1}{Re_\tau} \nabla^2 \varphi , \quad (2.6)$$

$$\frac{\partial \omega_y}{\partial t} = h_g + \frac{1}{Re_\tau} \nabla^2 \omega_y \quad (2.7)$$

with

$$h_v = \frac{\partial}{\partial y} \left( \frac{\partial H_1}{\partial x} + \frac{\partial H_3}{\partial z} \right) + \left( \frac{\partial^2}{\partial x^2} + \frac{\partial^2}{\partial z^2} \right) H_2 , \quad (2.8)$$

$$h_g = \frac{\partial H_1}{\partial z} - \frac{\partial H_3}{\partial x}. \quad (2.9)$$

The code adopts a spectral method with Fourier expansions in the stream-wise  $x$  and spanwise  $z$  directions, as in the first code, but seven-point compact finite differences in the wall-normal  $y$  direction.

In order to test the performance of the code, we conducted some test cases regarding wall-time and memory requirements of the code with 128 cores as shown in figure 2.2 on *FUCHS Cluster at CSC, Frankfurt a. M.* showing a good scaling behavior.

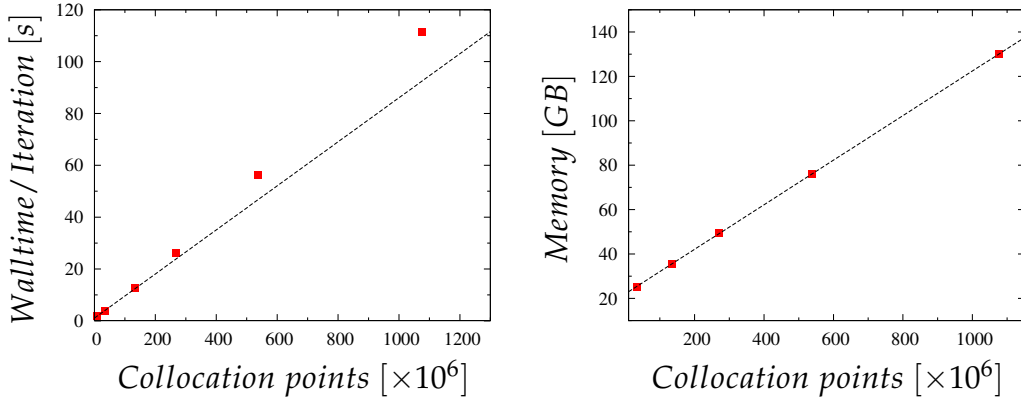


Figure 2.2: (a) Walltime per iteration and (b) used virtual memory as a function of numerical collocation points for processor number  $N_{proc} = 128$ .

-	$Re_\tau$	$L_x$	$L_z$	$N_x \times N_y \times N_z$	$\Delta x^+$	$\Delta z^+$	$\Delta y_c^+$	$\Delta y_{min}^+$
Case 1	180	$2\pi$	$\pi$	$512 \times 257 \times 256$	2.2	2.2	2.2	0.01
Case 2	360	$2\pi$	$\pi$	$512 \times 257 \times 256$	4.4	4.4	4.4	0.02
Case 3	720	$2\pi$	$\pi$	$1024 \times 513 \times 512$	4.4	4.4	3.9	0.31
Case 4	1440	$2\pi$	$\pi$	$2048 \times 513 \times 1024$	4.4	4.4	7.8	0.62

Table 2.1: Simulation parameters.  $L_x$  and  $L_z$  are the streamwise and spanwise dimensions of the computational box normalized by the channel half-height  $h$ .  $\Delta y_c^+$  and  $\Delta y_{min}^+$  are the dimensionless wall-normal resolutions in the center of the channel and at the wall, respectively.

## 2.2 Simulations

We conducted direct numerical simulations of the turbulent channel flow at four different Reynolds numbers to analyze the geometrical statistics of the dissipation elements (see Table 2.1). In periodic horizontal directions  $x$  and  $z$ , the numerical grid is distributed uniformly whilst the mesh is refined in the vicinity of the wall in order to account for high turbulence intensity created in this region. The minimum and maximum grid spacing in the wall normal direction for each  $Re$  case are shown. Furthermore, in Table 2.2, the numbers of grid points in the viscous sublayer near the wall are given.

$Re_\tau$	180	360	720	1440
Points	20	14	9	7

Table 2.2: Number of points in the viscous sublayer for different Reynolds numbers, i.e. in the range  $y^+ < 5$ .

## 3 Turbulent Channel Flow Statistics

Kolmogorov's spectral cascade theory is a milestone in the attempt to understand the theory of turbulence. But, one must not forget that the three-dimensional *homogeneous isotropic* turbulence remains an idealized assumption of an essentially very complex phenomenon. For a turbulent flow to be *homogeneous*, spatial gradients of averaged quantities must vanish, i.e. quantities must be invariant under translation. *Isotropic* turbulence additionally requires that the flow is invariant under rotation and that there is no mean flow as it would impose anisotropy. Strictly speaking, of course, none of these assumptions are valid for real flows.

For further understanding of turbulence, wall-bounded turbulent channel flow may serve as a more realistic case (see figure 2.1). Its relatively simple, yet realistic geometry allows for a theoretical investigation of near-wall turbulence.

Wall-bounded turbulent flows exhibit certain characteristic regions in the wall-normal direction, based e.g. on the functional form of the mean profile, where different turbulence phenomena are dominant to different degrees. Hence, all statistical quantities of these flows are inhomogeneous in the wall-normal direction.

For the present case of a pressure driven turbulent channel flow, a canonical member of this type of flow, four layers exist: a viscosity-dominated sublayer, a buffer layer where production of turbulent kinetic energy and the turbulence intensity itself reach their maximum, a logarithmic layer where production and dissipation are of the same order of magnitude and a core region, often denoted as defect layer Pope (2000).

Though a clear cut limit between layers is somewhat arbitrary, we now adopt the following classification:

- viscous sublayer:  $y^+ \leq 5$
- buffer region:  $5 < y^+ < 30$
- log region:  $y^+ \geq 30, y/h < 0.3$



- core region:  $0.3 \leq y/h < 1$

where  $y^+ = yu_\tau/\nu$  is the dimensionless distance from the wall.

### 3.1 Velocity Profiles

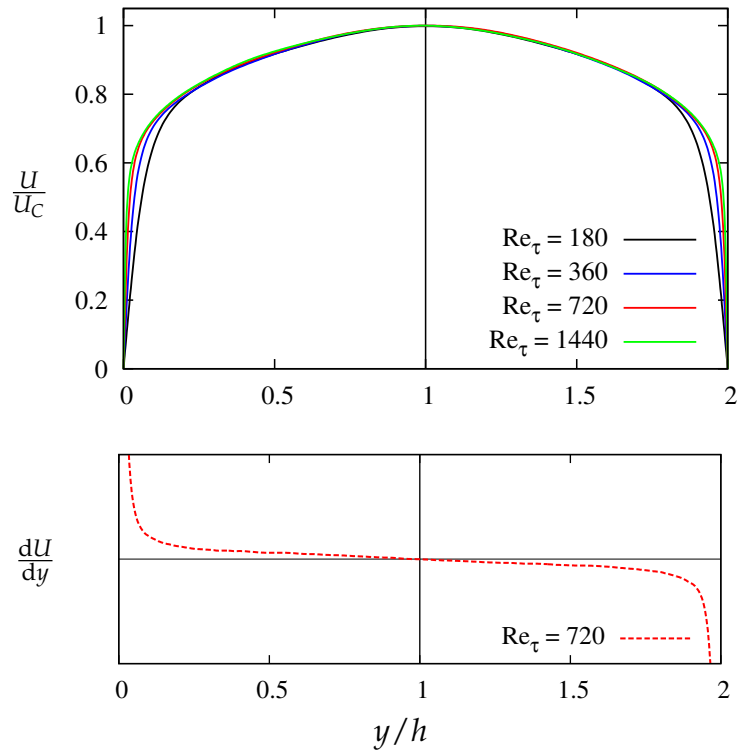


Figure 3.1: Mean velocity profile and its wall-normal gradient.

The mean velocity distribution is shown in figure 3.1 for different  $Re$  along the wall-normal direction  $y/h$ . All curves appear to be satisfactorily symmetrical as expected. Starting from the wall boundaries, where velocity vanishes, there is a limited near-wall region with very large gradients  $dU/dy$ , i.e. *mean shear*. Mean shear is closely related to the anisotropy of wall-bounded flows. With increasing  $Re$  these derivatives become even larger. Moving away from the wall, they continue to decrease further to become zero at the centerline of the channel, after which the same process with reversed sign comes into effect, as can be seen from the lower picture. Here,  $U_C$  denotes the centerline velocity and is used to obtain an alterna-

tive Reynolds number  $Re_C$ . By analogy,  $Re_b$  is the bulk Reynolds number based on the bulk velocity  $U_b$  where

$$U_b = \frac{1}{2h} \int_{-h}^h U(y) dy . \quad (3.1)$$

As in the case of the friction Reynolds number  $Re_\tau$ , the last two  $Re$  are related to the channel half width  $h$  and the kinematic viscosity  $\nu$ . According to Dean (1978), the correlation between the mean centerline velocity and the bulk mean velocity reads as follows:

$$\frac{U_C}{U_b} = 1.28 Re_b^{-0.0116} . \quad (3.2)$$

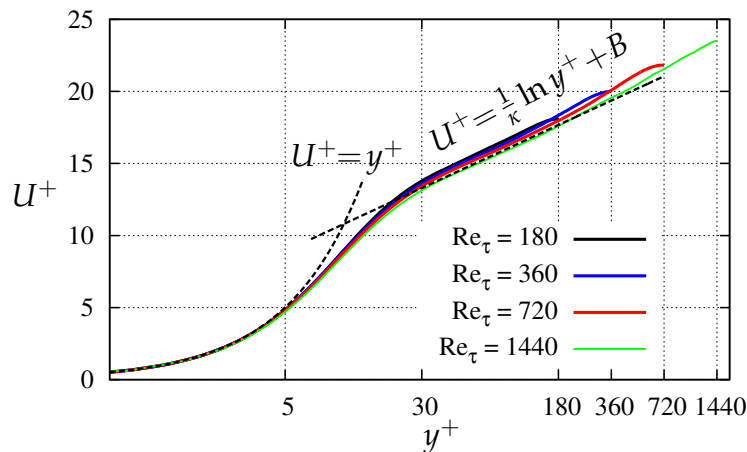


Figure 3.2: Universal velocity profile versus distance from the wall, expressed in wall units.

In figure 3.2 the mean velocity profiles are given in wall units, i.e. non-dimensionalized by the friction velocity  $u_\tau$ . It is striking how all velocity profiles collapse near the wall, even though the  $Re$  are far apart. This self-similar behavior can be derived analytically through dimensional analysis (see e.g. Bradshaw & Huang (1995)). Under the assumption of plane, smooth wall boundaries the mean velocity can be expressed in terms of the wall shear stress  $\tau_w$ , the wall-normal distance  $y$ , fluid density  $\rho$  and viscosity  $\mu$ . The wall-normal region in which this relation holds is called the *inner layer*, the rest being the *outer layer*.

$$U^+ = \frac{U}{u_\tau} = f\left(\frac{u_\tau y}{\nu}\right) = f(y^+) . \quad (3.3)$$

In the very near-wall region, viscosity effects are dominant. Here, equation 3.3 yields a linear pattern.

By substituting  $\partial U/\partial y$  for  $U$ , we obtain

$$\frac{\partial U}{\partial y} = \frac{u_\tau}{y} g(y^+) . \quad (3.4)$$

Taking into account that the influence of the viscosity in far-wall regions is negligible and, thereby,  $g(y^+)$  is transformed into a constant, namely the inverse of the *Kármán* constant ( $1/\kappa$ ).

$$\frac{\partial U}{\partial y} = \frac{u_\tau}{\kappa y} . \quad (3.5)$$

Finally, after integrating equation 3.5 one arrives at

$$\frac{\partial U}{\partial y} = \frac{1}{\kappa} \ln \frac{u_\tau y}{\nu} + C \quad \text{or,} \quad (3.6)$$

$$U^+ = \frac{1}{\kappa} \ln y^+ + B , \quad (3.7)$$

with  $\kappa \approx 0.41$  and  $B \approx 5.1$ . Besides the curves for different  $Re_\tau$ , figure 3.2 displays the linear scaling law in the viscous sublayer (3.3) and the logarithmic law (3.6), also known as the *log-law*. The log-law is a popular tool in describing the inner region of plane wall-bounded flows, such as the channel, pipe and boundary layer flows. However, some authors raised concerns regarding the existence of the logarithmic law, or the function  $g(y^+)$  being independent of  $Re$ . Barenblatt (1993), for instance, favors a power law stating that the assumption of a velocity gradient independent of  $Re$  in equation 3.4 may not be suitable.

Moreover, there are also works (e.g. Zagarola, Perry & Smits (1997)) suggesting that both the logarithmic law and the power law are justified in this region, albeit separated from each other. Based on experiments of

smooth turbulent pipe flow measured in the *Princeton University Super-Pipe*, the authors predict a power law following the buffer layer and a logarithmic law in the subsequent overlap region above. Contrary to Barenblatt (1993), they conclude that a logarithmic overlap region does exist at sufficiently high  $Re$ , indicating a complete similarity in this region.

This finding is supported by Oberlack (2001) who derived both scaling laws directly from Reynolds-averaged Navier-Stokes equations using the Lie symmetry group approach.

Nonetheless, the logarithmic law is generally accepted by the turbulence community and is also adopted in the present work. In accordance with Kim et al. (1987), who notes that the logarithmic region exists even at the lowest Reynolds number of  $Re_\tau = 180$ , in figure 3.2 our numerical experiments show a good agreement with the logarithmic law. Their agreement with the log-law is particularly pronounced in the case of higher  $Re$ .

According to the velocity defect law of von Kármán (1930), the difference between the velocity at the centerline  $U_C$  and the local mean velocity  $U$ , normalized by the friction velocity  $u_\tau$ , is a function of the distance from the wall such that

$$\frac{U_C - U}{u_\tau} = G(y^+) . \quad (3.8)$$

Equating the velocity profiles in the *velocity defect law* and the *law of the wall* (equation 3.3) to each other yields

$$\frac{U_C - U}{u_\tau} = -\frac{1}{\kappa} \ln \left( \frac{y}{h} \right) + B_1 . \quad (3.9)$$

This can be seen as an alternative approach to derive the logarithmic law. Unlike in the log-law, the integration constant  $B_1$  is flow-dependent.

The *Kármán* constant can be obtained from equation 3.7 as

$$\kappa = \left( y^+ \frac{dU^+}{dy^+} \right)^{-1} . \quad (3.10)$$

It is expected that  $\kappa$  will exhibit a constant course in the validity region of the log-law. To review this statement, in figure 3.3 (a) we plot this quantity as a function of non-dimensional wall-distance  $y^+$  at different  $Re$ . As can

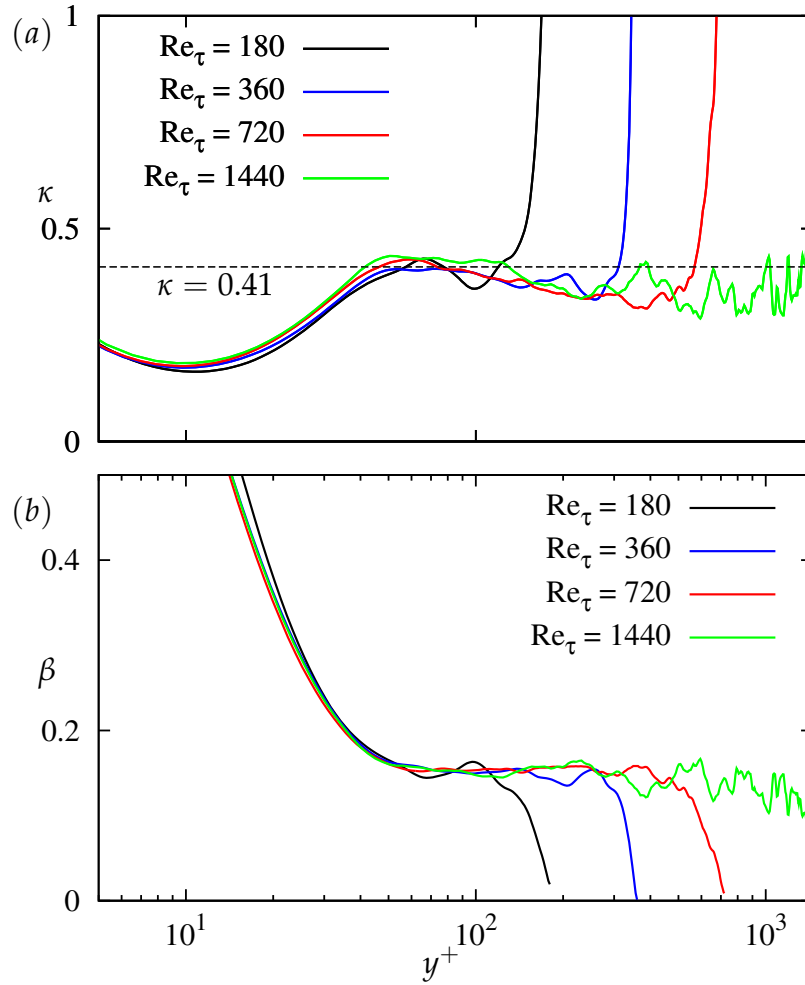


Figure 3.3: Log-law Kármán constant  $\kappa$  (a) and power law constant  $\beta$  (b).

be seen, all curves approximate the value of 0.41 in the region assigned to the logarithmic layer, though to different degrees.

The counterpart is the examination in respect to possible power law evidence. For this, 3.3 (b) shows the quantity  $\beta$  where

$$\beta = \frac{y^+}{U^+} \frac{dU^+}{dy^+}. \quad (3.11)$$

For the power law, i.e.  $U^+ = F(y^+)^n$ , to be a better approach,  $\beta$  needs to feature a constant stage of  $n$  in that region. The plot, however, reveals no

objective evidence to suggest that a power law should be preferred over log-law.

In conclusion, it can be stated that it is well justified to adopt the logarithmic law.

## 3.2 Turbulence Intensities

Figure 3.4 shows the *root mean square* ( $u_{rms}/u_\tau$ ,  $v_{rms}/u_\tau$ ,  $w_{rms}/u_\tau$ ) of velocity fluctuations or, in other words, the turbulent intensity profiles versus dimensionless wall-normal distance  $y^+$ . A strong dependency on *Reynolds number* is observed for all three components increasing with  $Re$ . It is interesting to note that all streamwise fluctuations  $u_{rms}^+$  reach a maximum within the near-wall buffer layer ( $5 < y^+ < 30$ ) before a sudden decrease. Despite major gaps between the various  $Re$ , the profiles of  $u_{rms}^+$  collapse nicely in this layer indicating a scaling with inner variables. Mochizuki & Nieuwstadt (1996) find that the peak value of the streamwise *Reynolds stress* is an essentially  $Re$ -independent constant  $u_{max}^2/u_\tau^2 = 7.34$ . This is in good agreement with our results ( $u_{max}^+ \approx 2.7$ ), although minor deviations can be detected with respect to  $Re$ . The location of the maximum in terms of  $y^+$ , however, may be weakly dependent on  $Re$ , albeit always in the buffer layer.

This is rather different from the behavior of  $u_{rms}^+$  if the wall distance  $y$  is not expressed in wall units, but rather with channel half height  $h$  (see figure 3.5). Besides the viscous sublayer, there is a strong  $Re$  impact on the profiles up to the channel core region ( $y/h = 0.3$ ). The location of the peak is influenced by the Reynolds number. For higher  $Re$ , it is shifted towards the wall boundaries alongside with the buffer layer.

Moving away from the wall, namely in the core region of the channel, the curves of all velocity components approach each other for different  $Re$  as illustrated in figure 3.5. Note that in the case of  $u_{rms}^+$  the collapse is particularly well, especially for the two higher  $Re$  indicating a universal character. It can be assumed that this collapse is a *high Re limit* (see Moser, Kim & Mansour (1999)) where *rms* profiles scale linearly with the wall-normal distance  $y/h$  in the outer region  $0.2 < y/h < 0.85$ , except for some deviations in the low  $Re$  case.

The  $Re$  effect is more apparent for the wall-normal and spanwise velocity components. In contrast to  $u_{rms}^+$ , there is no indication for the existence of

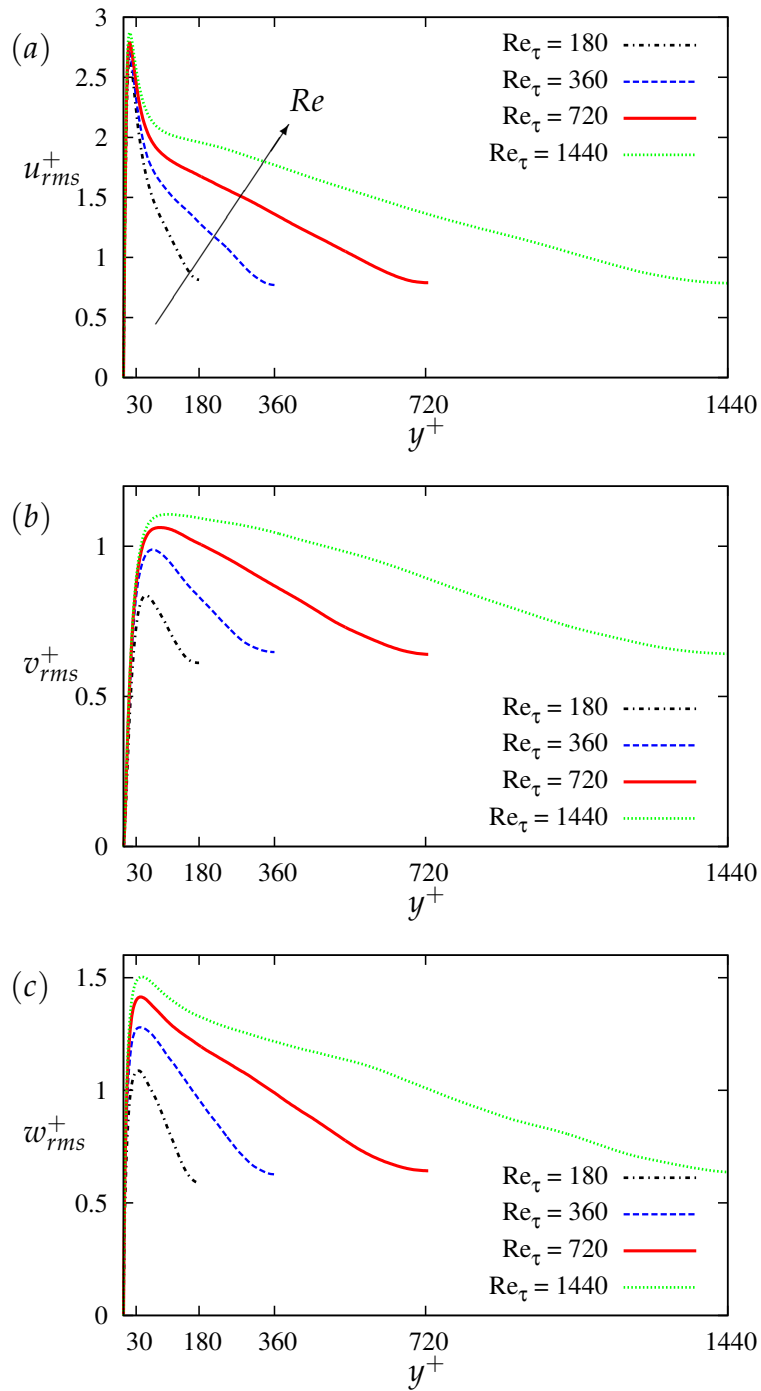


Figure 3.4: Turbulent intensity profiles normalized with wall variables ( $u_\tau, v/u_\tau$ ).

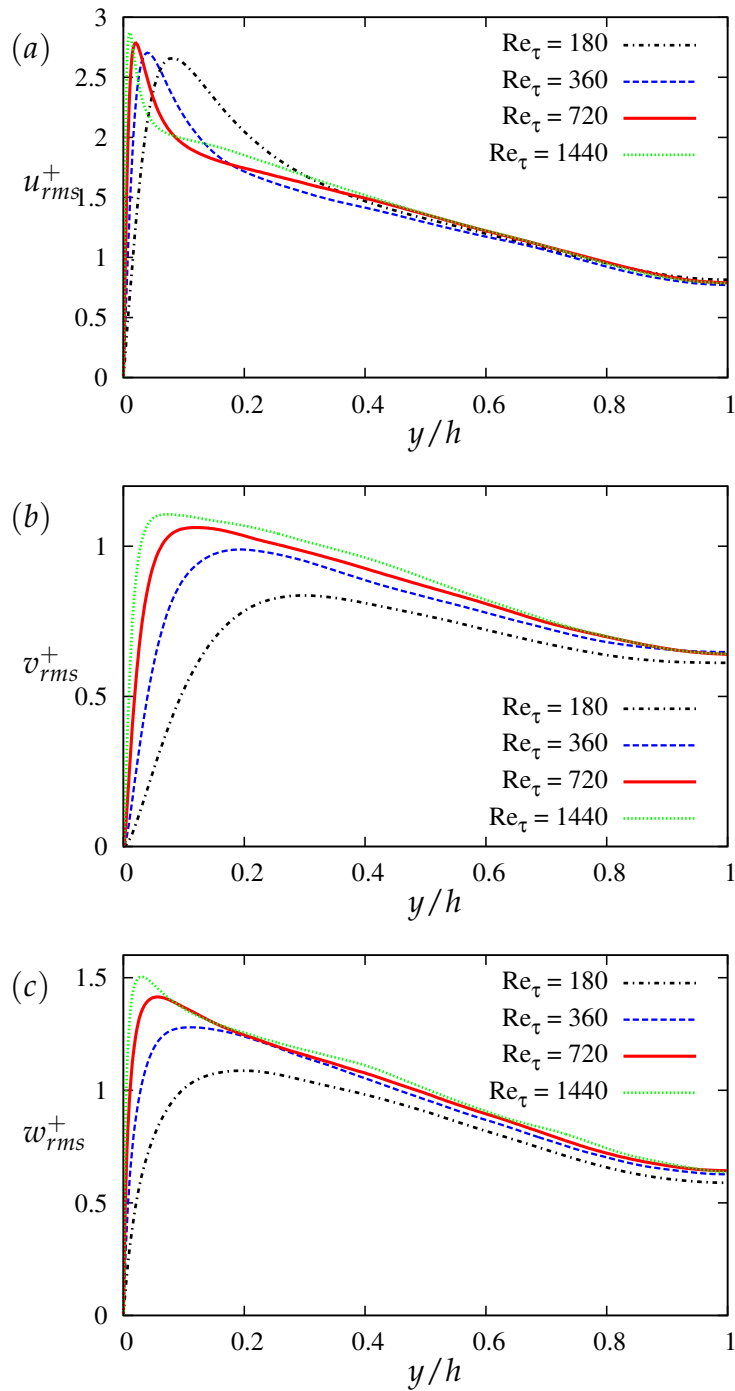


Figure 3.5: Turbulent intensity profiles versus wall-normal distance.



a quasi constant peak value for different  $Re$ . Figures 3.4 and 3.5 illustrate that both inner and outer scaling are unable to attain self-similar profiles in the *overlap region*, including the logarithmic layer. Instead, it is justified to adopt the *viscous length scale*  $\nu/u_\tau$  for the inner region and the *channel half height*  $h$  for the outer flow of the channel.

Furthermore, the normal component of the velocity decreases much faster than the horizontal velocity components. Hence, the flow motion very close to the wall boundaries takes place preferably in horizontal directions  $x, z$  parallel to the wall.

### 3.3 Energy Dissipation Rate

Owing to the anisotropic, inhomogeneous character of wall-bounded turbulence, the normalized profile of the energy dissipation rate (equation 1.10)  $\epsilon^+ = \epsilon\nu/u_\tau^4$  in figure 3.6 displays a strong impact of the distance from the wall. In contrast to homogeneous flows, in channel flow the contribution of the three velocity components is not identical as is evident from figures 3.4, 3.5. In fact, the influence of the streamwise component is dominant. The maximum amount of energy loss occurs close to the wall, i.e. in the viscous sublayer up to  $y^+ < 5$ , where viscous effects are most influential. The peak value of  $\epsilon^+$  is found to be in the range 0.165 to 0.251 and tending to an asymptotic value with increasing Reynolds number as reported in Shih & Lumley (1993). This is in good agreement with present results. Away from the wall the dissipation rate decreases fast before rising somewhat around to the buffer layer which is evident from the small bump. This is best observed in the low  $Re$  case, but weakens for higher  $Re$ .

Remarkable differences are apparent regarding the overall shape of the profiles. With increasing  $Re$  the dissipation apparently decreases in the outer region of the flow while increasing in near-wall regions, namely in viscous and buffer layers. In the channel core the different dissipation profiles become very small approaching each other towards the centerline.

Equation 1.10 for the energy dissipation rate involves a total of nine gradients of the velocity fluctuations in all three dimensions. In the presence of inhomogeneous flows the contribution of each gradient is different along the channel height. To illustrate this, figure 3.7 depicts normalized root-mean-square values of the velocity derivatives with respect to the wall

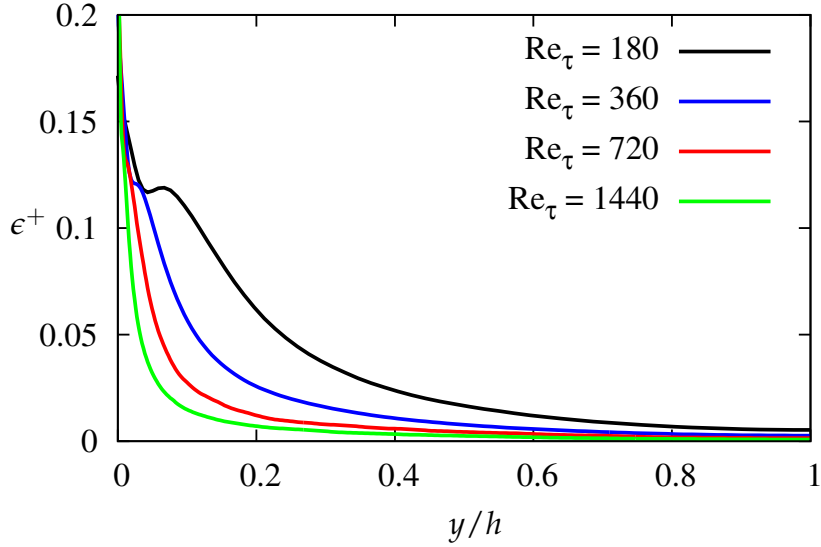


Figure 3.6: Normalized energy dissipation rate across the wall-normal direction of the channel.

distance for the highest  $Re_\tau = 1440$  case. Results at  $Re_\tau = 720$  show similar behavior. Black, red and blue curves represent the gradients of the streamwise velocity  $u$ , wall-normal velocity  $v$  and spanwise velocity  $w$ , respectively.

As expected, there are enormous differences between the components spanning orders of magnitude. The plots give also insight to the interesting question as to which gradients are dominant within the budget of  $\epsilon$ . The gradient of the spanwise velocity  $w$  with respect to wall distance  $y$  appears to be the leading part exceeding all other gradients by far. This is followed by the wall-normal derivative of the streamwise velocity component  $u$ . The contributions of both, in turn, exceed that of the wall-normal gradient of  $v$  such that,

$$\frac{\partial w}{\partial y} > \frac{\partial u}{\partial y} > \frac{\partial v}{\partial y}. \quad (3.12)$$

$\partial_y v$  is rather of the order of derivatives with respect to the streamwise direction  $x$ . Latter three derivatives ( $\partial_x u$ ,  $\partial_x v$ ,  $\partial_x w$ ) are seen to be more or less comparable with each other. Velocity gradients with respect to the spanwise direction  $z$  seem to be least influential as suggested by dotted curves.

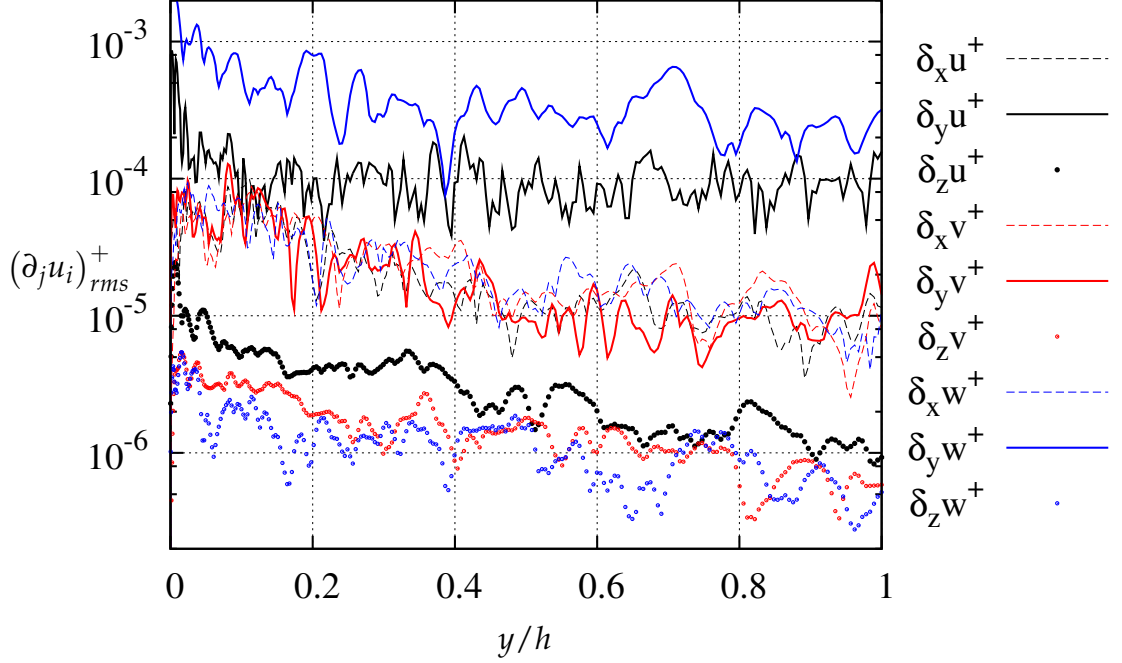


Figure 3.7: Normalized rms velocity gradients along wall-normal direction.

Roughly speaking, one can argue that wall-normal derivatives are highest, followed by the streamwise and spanwise gradients ( $\partial_y u_i > \partial_x u_i > \partial_z u_i$ ).

A more complete hierarchy reads as follows,

$$\frac{\partial w}{\partial y} > \frac{\partial u}{\partial y} > \frac{\partial v}{\partial y'} \frac{\partial u_i}{\partial x} > \frac{\partial u}{\partial z} > \frac{\partial v}{\partial z'} \frac{\partial w}{\partial z}. \quad (3.13)$$

Another important observation is the behavior in relation to the distance from the wall. Similar to the profile of  $\epsilon$ , all gradients attain maximal values at the wall and decrease while moving away from the wall.

Apart from the energy dissipation rate, there are also other turbulent quantities that are defined by all or some of these derivatives. Such quantities include, for instance, the strain rate, vorticity, enstrophy and the second invariant of the velocity gradient tensor, some of which will be discussed in chapter 4.

## 4 Instantaneous Fields

Instantaneous turbulent fields allow the study of interesting details closely related to the geometrical structure of turbulent patterns. There are many efforts to extract information about the behavior and the nature of these spatial structures. Are they simply chaotic, or do they follow an ordered structure? What is the role of the wall-induced anisotropy in their distribution? Equally large are the numbers of approaches to identify turbulent structures from a given instantaneous field.

*Vortex identification* plays a key role in characterizing organized structures. However, first one needs to provide a consistent definition of a spatial pattern, called *vortex*. Despite its chaotic nature, turbulence is well known to contain coherent small-scale structures making themselves apparent through non-Gaussian intermittent behavior.

### 4.1 Vorticity

For the identification of small-scale turbulent structures, *vorticity*  $\omega$  is a useful quantity which is defined as the curl of the velocity vector.

$$\begin{aligned}\omega &= \nabla \times \mathbf{U} \\ &= \begin{pmatrix} \frac{\partial w}{\partial y} - \frac{\partial v}{\partial z} \\ \frac{\partial u}{\partial z} - \frac{\partial w}{\partial x} \\ \frac{\partial v}{\partial x} - \frac{\partial u}{\partial y} \end{pmatrix}\end{aligned}\quad (4.1)$$

The vector  $\omega$  can be understood as the rotation of a fluid element around its own axis. In analogy to the Navier-Stokes equations (1.2), vorticity is often used to describe the fluid motion instead of the primitive variables such as pressure and velocity through the *vorticity transport equation*.

$$\frac{D\omega}{Dt} = \omega \cdot \nabla \mathbf{U} + \nu \nabla^2 \omega \quad (4.2)$$

Vorticity appears as vortex tubes in local regions with high intensity composed of vortex lines which are tangent to the local vorticity. The circulation around such a tube, which is a measure for its strength, remains constant due to the divergence-free nature of vorticity.

## 4.2 Second Invariant of the Velocity Gradient

Another important quantity in aiding the study of turbulence dynamics is the velocity gradient tensor  $A_{ij} \equiv \partial u_i / \partial x_j$  which determines the stretching and rotation rates of material lines, surfaces and volumes. It is relevant to important phenomena such as the vortex stretching, scalar mixing, surface propagation and small-scale evolution in fluid flows.

The tensor can be decomposed into a symmetric *rate-of-strain tensor* and an skew-symmetric *rate-of-rotation tensor*, respectively, as

$$A_{ij} = S_{ij} + W_{ij}, \quad (4.3)$$

where

$$S_{ij} = \frac{1}{2} \left( \frac{\partial u_i}{\partial x_j} + \frac{\partial u_j}{\partial x_i} \right) \quad (4.4)$$

$$W_{ij} = \frac{1}{2} \left( \frac{\partial u_i}{\partial x_j} - \frac{\partial u_j}{\partial x_i} \right). \quad (4.5)$$

For  $S_{ij}$  and  $W_{ij}$ , the invariants  $Q_S, Q_W, R_S$  can be derived (see Chong, Soria, Perry, Chacin, Cantwell & Na (1998)) which are non-zero with  $R_S = -1/3(S_{ij}S_{jk}S_{ki})$ .

The second invariant  $Q = Q_S + Q_W$  is the most important since it is closely linked to strain and vorticity with

$$Q_S = -\frac{1}{2} S_{ij} S_{ji} \quad (4.6)$$

$$Q_W = \frac{1}{2} W_{ij} W_{ji}. \quad (4.7)$$

Note that  $Q_S$  is always negative whereas  $Q_W$  is positive. With this in mind, the second invariant for incompressible flow yields,

$$\begin{aligned}
Q &= \frac{1}{2} (W_{ij}W_{ji} - S_{ij}S_{ji}) \\
&= -\frac{1}{2} \frac{\partial u_i}{\partial x_j} \frac{\partial u_j}{\partial x_i}.
\end{aligned} \tag{4.8}$$

Taking a closer look, one can notice that the components of  $Q$  are related to the enstrophy  $\omega^2$  and the dissipation rate of the kinetic energy such that

$$\omega^2 = 4 Q_W, \tag{4.9}$$

$$\epsilon = -4 \nu Q_S. \tag{4.10}$$

Hence, the second invariant  $Q$  is directly linked to both these well-known turbulence quantities as follows

$$Q = \frac{1}{4} \left( \omega^2 - \frac{\epsilon}{\nu} \right). \tag{4.11}$$

$Q$  can be positive or negative depending on the local balance between the vorticity and dissipation as illustrated in equation 4.11. As a consequence, local areas of high vorticity will result in high positive values of  $Q$ . Contrarily, large negative values of  $Q$  will be located in regions of high dissipation intensity. Different levels of  $Q$  represent different types of flow patterns. This is therefore a quantity well-suited to identify turbulent structures.

Accordingly, we plot the second invariant of the velocity gradient tensor  $Q$  together with other turbulent quantities in order to observe the interplay between them. Furthermore, the influence of the Reynolds number  $Re$  and the wall boundary is examined.

In figure 4.1  $Q$  alone is plotted in the channel showing two large positive and negative levels at three different  $Re$ . The quantities are normalized with inner layer scaling variables. It is interesting to note that regions with large positive values of  $Q$  exhibit tube-like structures whereas large negative values appear to be stretched sheets. Both, negative and positive high intensity regions are located in the immediate vicinity of each other indicating large gradients.

Moreover, intense vortex tubes and vortex sheets are clustered with each other in some areas attesting to coherence. This is well known for high  $Re$ . However, there is evidence for such tendency even in the lower  $Re$  case (top figure). Here, mostly quasi-streamwise vortices are present whose wall-normal core location is in the range  $y^+ \approx 20 - 40$  as also reported in Tomkins & Adrian (2003). These vortices are slightly tilted from the wall.

In general, vortex structures are under strong influence of  $Re$ . While, for instance, there exist fewer but much longer vortex tubes in the low  $Re$  case for increasing  $Re$  a larger quantity of structures are created that are considerably smaller. Furthermore, as  $Re$  increases, the type of the structures also change. This means that in addition to the streamwise structures, arch-type vortices are introduced.

So-called *hairpin vortices* which were proposed first by Theodorsen (1952), consisting of two quasi-streamwise legs and a spanwise head part (also known as horseshoe vortices) can also be seen. These vortex structures are organized in *hairpin packets* aligned in the streamwise direction. Evolving along the streamwise direction, they spawn new hairpin vortices. Hereby, these structures are being stretched streamwise by the mean shear whereas their heads are lifted away from the wall due to self-induction. They are believed to be closely related to the quasi-streamwise vortices such that the latter represent the legs of the hairpin vortices. Hairpin vortices are not restricted to regions very close to the wall, but can, in fact, grow and be lifted up to logarithmic layer and above. Although often illustrated symmetrically in idealized sketches, they are usually asymmetric and even one-sided.

In general, vortices near the wall are smaller compared to those in the outer layer of the flow. Tomkins & Adrian (2003) reports that mean values of spanwise length scales increase linearly with distance from the wall. This is similar to our findings in the context of Dissipation Element length scales as will be discussed later.

In figure 4.2, high- and low-speed streaks (blue and green) of the streamwise velocity and quasi-streamwise vortices (brown) are displayed. The isosurface of  $Q^+ = 0.015$  is brown as in previous figure 4.1. It is observed that quasi-streamwise vortices are in close proximity to the low-speed streaks. The latter are more elongated than the high-speed streaks. Low-speed streaks are generated by the induction of the hairpin vortex legs. High- and low-speed streaks appear to be different regarding their size, i.e. high-speed streaks are markedly shorter. Similar to  $Q$ , an increase

in  $Re$  results in increased irregularity of the shape of the velocity streaks on the one hand, and causes shorter streaks on the other.

According to equation 4.11, vorticity plays an important role in the budget of  $Q$ . To further investigate this assertion, both quantities are shown in normalized form with high amplitudes (see figure 4.3). One observes that tube-like vortices of  $Q$  with large positive amplitudes emerge mainly near vorticity-dominated regions close to the wall. Consequently, regions of strong strain will lead to large negative values of  $Q$  in the form of stretched sheets.

One disadvantage of using vorticity is that tube-like vorticity structures can only be obtained by displaying vortex lines. The radius of such vortex tubes is typically of the order of Kolmogorov length scale. The relationship between  $Q$ , i.e. quasi-streamwise vortices, and vortex lines is exposed in figure 4.4 exemplarily for three vortices. Interestingly enough, it can be deduced that vortex lines are clearly aligned with the direction of the respective  $Q$  vortex in its core. Apparently, this only applies to the core, where the magnitude of  $Q$  is high. One can see how the vortex lines enter the tubes and move inside the core before exiting again in lower intensity regions. They are well-organized within the vortex core but diverge gradually while moving away. Hence, at low vorticity regions vortex lines are highly random as is apparent from the figure.

In literature there is a large number of different vortex classifications. However, there is still no consensus as to which vortex structures are the most significant with respect to turbulence dynamics. However, what they all have in common is the arbitrary character. Since the extent of these structures arbitrarily depends on the chosen iso-surface level, a unique decomposition of the turbulent field into such vortices is not possible.

In fact, there are other approaches to overcome this difficulty such as the Dissipation Element method which is the main subject of the present work and will be presented later.



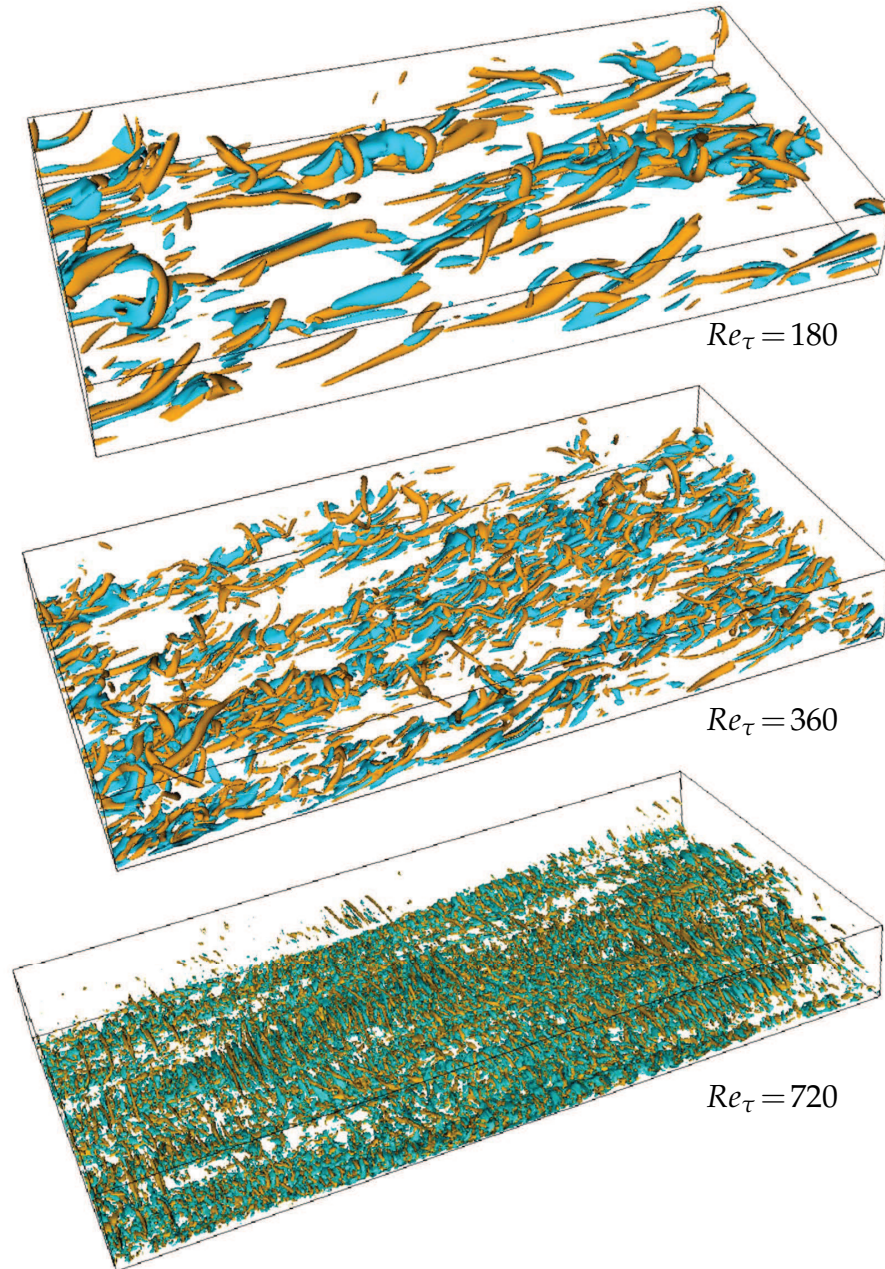


Figure 4.1: Normalized second invariant of the velocity gradient  $Q$  for different  $Re$  ( $Q^+ = -0.015$ , light blue;  $Q^+ = 0.015$ , brown).  $Q^+ = \pm 0.07$  is chosen for  $Re_\tau = 720$ . The flow goes from left to right.

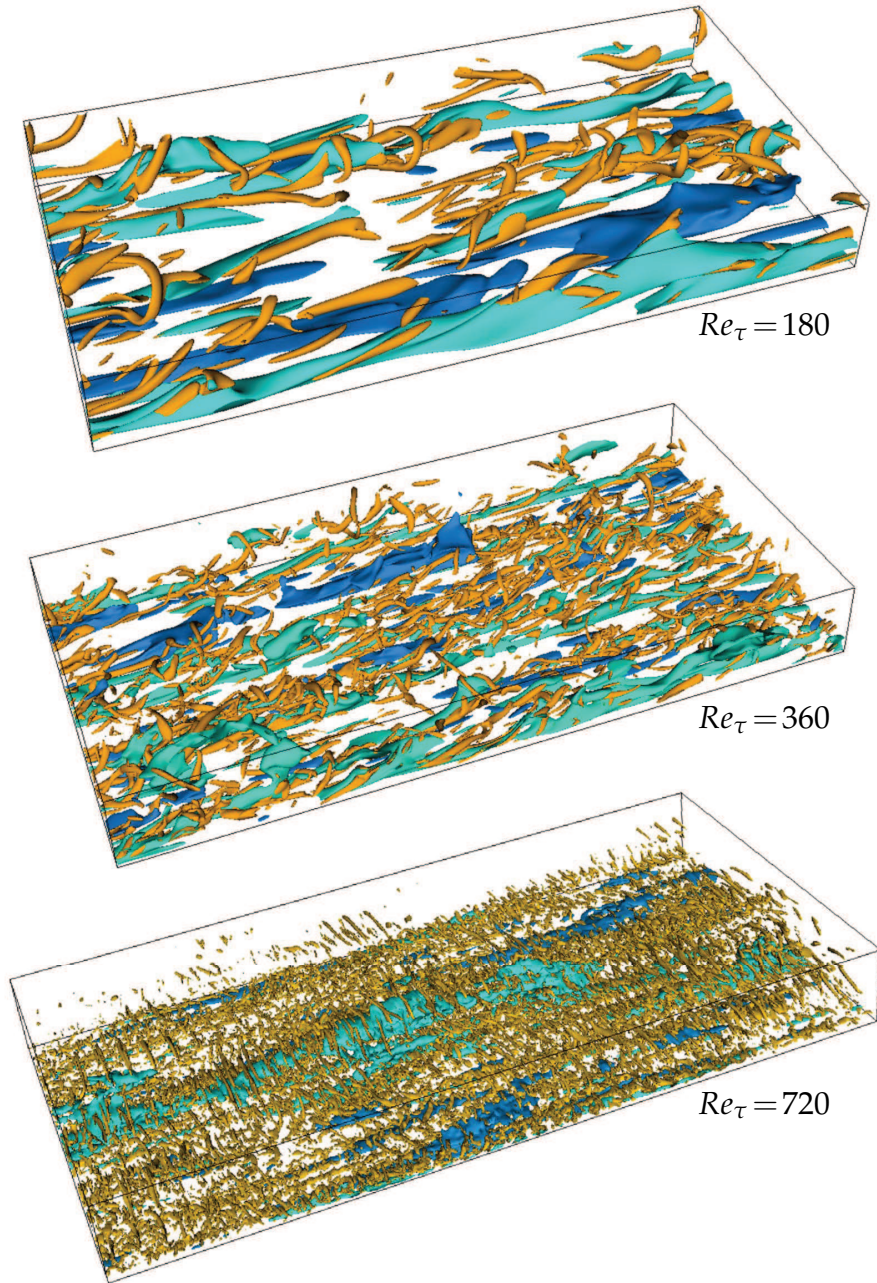


Figure 4.2: The second invariant  $Q$  and streamwise low- and high-speed streaks for different  $Re$  ( $Q^+ = 0.015$ , brown;  $u^+ = -3.7$ , green;  $u^+ = 3.7$ , blue).  $Q^+ = 0.07$  is chosen for  $Re_\tau = 720$ .

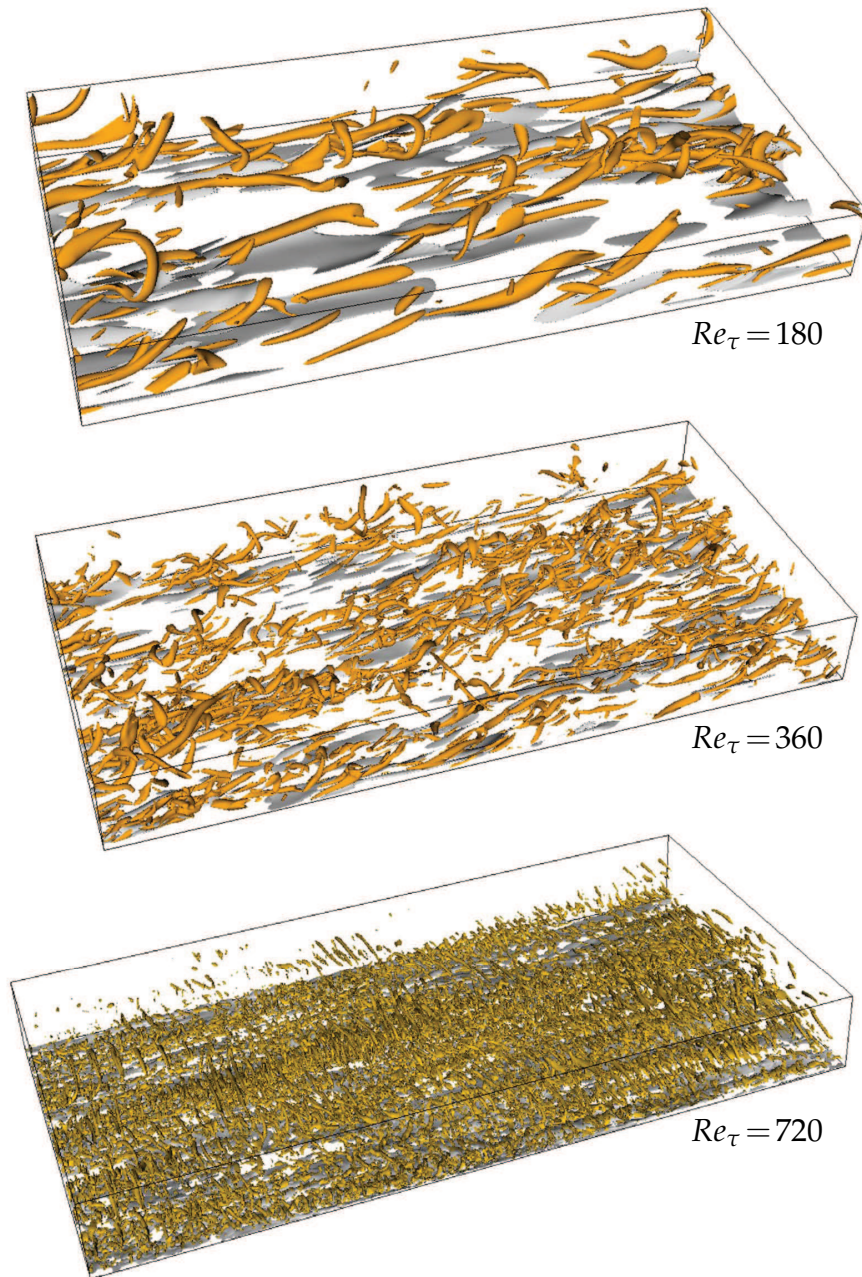


Figure 4.3: Normalized second invariant  $Q$  and vorticity magnitude for different  $Re$  ( $Q^+ = 0.015$ , brown;  $\omega^+ = 0.6$ , gray).  $Q^+ = 0.07$  is chosen for  $Re_\tau = 720$

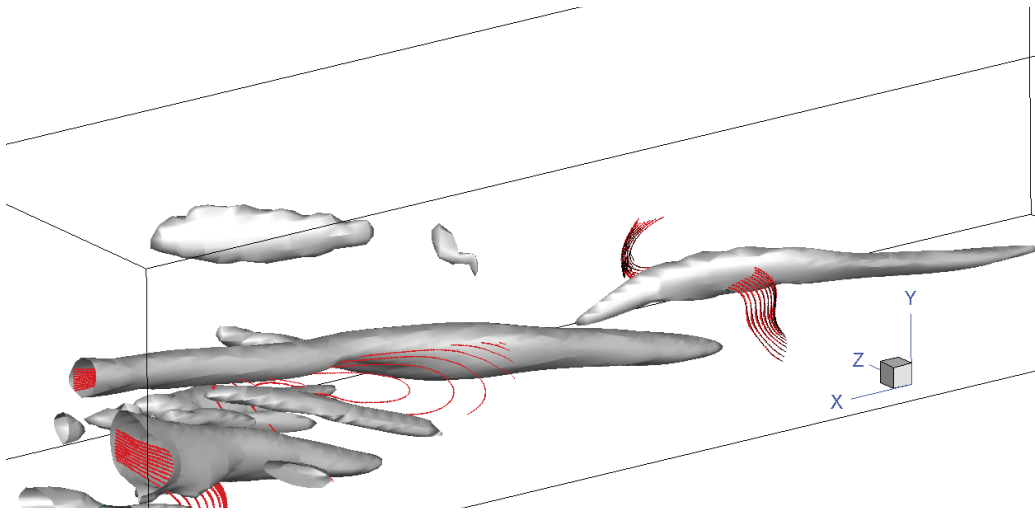


Figure 4.4: Interaction between  $Q$  and vortex lines.

## 5 Length Scales in Turbulent Channel Flow

As discussed before, turbulence produces structures with a wide-ranging spectrum of length. According to the classical theory of turbulence, this spectrum is limited by the integral length scale  $L$  from above and the dissipative Kolmogorov length  $\eta$  from below, respectively.

In the region far from the largest and the smallest scales local motions are largely independent of boundary influences and viscosity. Among these scales, the integral length scale is an estimate of the largest turbulent scales which corresponds to the size of the largest eddies and is of the order of the channel height in our case. Integral length scales are usually anisotropic, in other words, they are different with respect to the sense of direction as for any inhomogeneous flow. Since the characteristic velocity of these eddies is of the same order of magnitude as the mean fluid velocity, their Reynolds number is large and the direct effect of the viscosity can be neglected in a statistical sense. As stated earlier, energy is injected into the flow at very large scales. According to the energy cascade model large eddies will break up due to their instability while transferring the energy extracted from the mean flow to smaller eddies until the stage of dissipative scales is reached where energy dissipates into heat due to viscous effects. This is true for any fluid flow at sufficiently high Reynolds number.

Obukhov (1949) and Corrsin (1951) independently extended the second Kolmogorov hypothesis to the process of turbulent scalar mixing, assuming that many aspects of turbulence are universally similar, although the scalar hypotheses are complicated by the effects of *Prandtl number*,

$$Pr = \frac{\nu}{D}, \quad (5.1)$$

where  $D$  is the molecular diffusivity of the scalar. This provides a new length scale  $L_c$  which is analogous to the definition for  $\eta$ . The case where Prandtl number  $Pr \leq 1$  yields the Obukhov-Corrsin inertial-diffusive scale as

$$L_c = \left( \frac{D^3}{\epsilon} \right)^{1/4}. \quad (5.2)$$

The case with  $Pr = 1$ , and accordingly  $\nu = D$ , leads to the fact that the Obukhov-Corrsin length scale is equal to the Kolmogorov scale.

For large  $Pr$  numbers with weakly diffusive scalars one obtains the Batchelor scale

$$L_B = \left( \frac{D}{\gamma} \right)^{1/2} = \frac{\eta}{\sqrt{Pr}}, \quad (5.3)$$

where  $\gamma = (\epsilon/\nu)^{1/2}$  is the small-scale strain rate. For a given flow, the Batchelor scale decreases with increasing  $Pr$ .

Beside these, considering pure hydrodynamic turbulence there is also the intermediate Taylor length scale  $\lambda$ , with  $\eta \ll \lambda \ll L$ . This scale is preferred in the study of homogeneous turbulence and is defined as

$$\epsilon = 15\nu \frac{u'^2}{\lambda^2}, \quad (5.4)$$

where  $u'$  is the rms value of velocity fluctuation. Additionally, this is also a good qualitative measure for anisotropic turbulence since the contribution of the anisotropic part is very small. This expression yields

$$\lambda = \left( 10\nu \frac{k}{\epsilon} \right)^{1/2}, \quad (5.5)$$

where  $k = (3/2)u'^2$  is the turbulent kinetic energy associated with large scale eddies. The physical meaning of the Taylor scale is still a subject of discussions. Although it has no distinct physical interpretation, it can be considered as the distance that a large eddy advects a small Kolmogorov eddy during its turn-over time  $t_\eta = (\nu/\epsilon)^{1/2}$ . It is assumed that the inertial range with energy balance is extended from  $L$  to  $\lambda$  where viscosity effects start to gain influence towards  $\eta$ .

Regarding turbulent length scales, the main focus of the present work is the question of how they are affected by wall-bounded shear flows. While

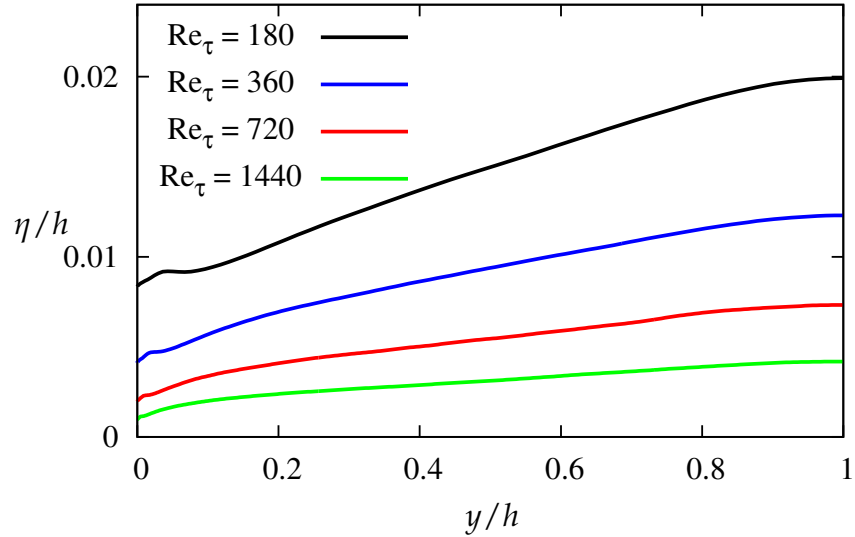


Figure 5.1: Kolmogorov length scale  $\eta$  as a function of wall-normal distance.

homogeneous turbulence yields solely an integral value for the entire turbulent field, wall-bounded flows, e.g. channel flow, possess inhomogeneous length scale profiles as functions of the wall distance  $y$  as a result of strong mean shear. This is due to the no-slip condition inducing a strong anisotropy and mean velocity gradients along the channel height to different degrees which is responsible for the anisotropic behavior of the statistics.

## 5.1 Kolmogorov Length Scale

To begin exploring the influence of the walls, we recall the definition of the Kolmogorov length scale

$$\eta = \left( \frac{\nu^3}{\epsilon} \right)^{1/4},$$

which includes the dissipation rate of the kinetic energy  $\epsilon$  (equation 1.10). Figure 3.6 testifies to the strong dependence of the dissipation rate on the wall-normal direction  $y$ . Thus,  $\eta$  will feature a wall-normal dependency as well. In fact, the profiles for  $\eta$  at different Reynolds numbers in picture 5.1 approve this expectation. All curves show a local maximum at

the position around the near-wall buffer region where the corresponding  $\epsilon$  profile exhibits a bump which disappears for high  $Re$ . Approaching the outer flow region,  $\eta$  scales linearly with the distance  $y$  between the point  $y/h \approx 0.2$  and the channel core region ( $y/h \approx 0.8$ ). In the core region, however, it tends asymptotically to a constant centerline value dependent on the Reynolds number  $Re$ . Hence, in relation to the wall-normal direction, three areas can be identified;

1. a near-wall region with no clear scaling property,
2. an intermediate region with linear scaling ( $0.2 \lesssim y/h \lesssim 0.8$ ),
3. a nearly constant core region.

Furthermore,  $\eta$  declines when  $Re$  is increased throughout the entire channel height. It can be asserted that both the wall-normal distance  $y$  and  $Re$ , exert a strong influence on Kolmogorov length scale,  $\eta(Re_\tau, y)$ .

Continuing further, we derive analytical relations for the latter two scaling regions with definable scaling properties. The linear scaling region can be approximated as follows,

$$\eta_{lin}(Re_\tau, y) / h \approx \frac{0.62}{(Re_\tau^{0.79} + 13)} + \frac{0.72}{(Re_\tau^{0.78} - 4.4)} \left(\frac{y}{h}\right). \quad (5.6)$$

As can be seen from picture 5.2, equation 5.6 is a good approximation for the linear region. In addition to our results, an even higher Reynolds number case with  $Re_\tau = 2003$  from Hoyas & Jiménez (2006) is shown to evaluate the quality of the approximation 5.6 indicating a very good match.

Similarly, an expression for the peak value of the Kolmogorov length at the centerline of the channel has been found as stated below (filled circles in figure 5.2). Fixing the position  $y$  at the centerline,  $\eta$  becomes a function of  $Re$  only, thus, resulting in the rather simple relation,

$$\eta_{CL}(Re_\tau, y=y_{CL}) / h \approx 1.0 Re_\tau^{-3/4}. \quad (5.7)$$

Note that the centerline position is the point with the least shear, i.e. being closest to the homogeneity in a turbulent Poiseuille flow. The knowledge of the size of Kolmogorov scale is of particular interest for the purpose of grid spacing estimation  $\Delta x / \eta$ . In wall-bounded flows, the distribution is usually not equidistant, i.e. denser near the wall, in order to account for the high wall-normal gradients mentioned before. Equations 5.6 and 5.7



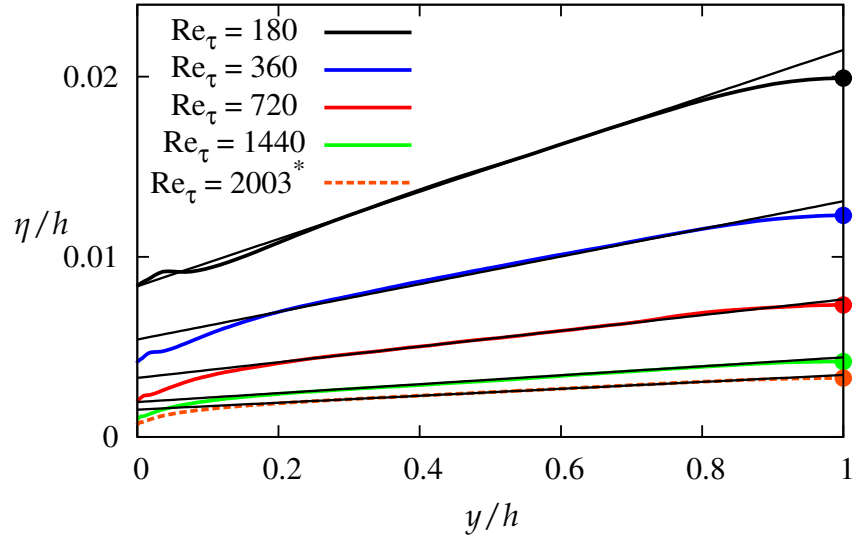


Figure 5.2: Kolmogorov length scale  $\eta$  compared with the approximations for the linear region and the centerline (filled circles). The data for  $Re_\tau = 2003$  was taken from Hoyas & Jiménez (2006).

could be used to estimate the number and distribution of the grid points especially with respect to the wall-normal direction allowing a more efficient grid resolution.

## 5.2 Taylor Length Scale

Taylor length  $\lambda$ , as defined in equation 5.5, is depicted in figure 5.3, again as a function of  $y$  for different Reynolds numbers. Wall influence is present in this case as well. A strong linear rise at the origin is followed by a slower increase up to the channel core where  $\lambda$  finally takes a constant value.

In homogeneous flows, Reynolds number based on the Taylor length scale,  $Re_\lambda$ , is the relevant parameter to characterize the flow as opposed to the friction Reynolds number  $Re_\tau$  in channel flow. This makes it difficult to compare these different flow regimes with respect to  $Re$ , since  $Re_\lambda$ , too, is a function of  $y$ . However, considering the single value of the Taylor length scale at the channel centerline associated with the mean flow, a corresponding  $Re_\lambda$  at the centerline can be obtained which allows a rough comparison of both flows. In this sense, the Taylor micro-scale  $\lambda(Re_\tau)$  at the centerline is calculated.

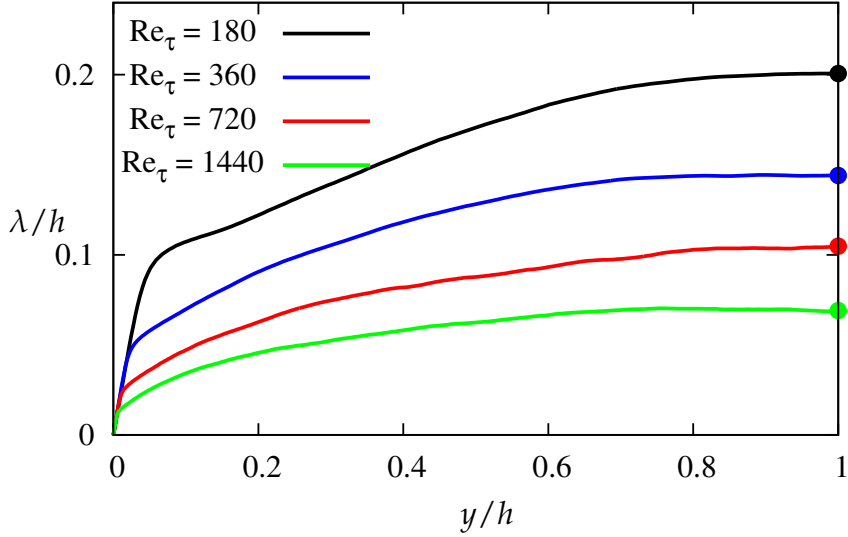


Figure 5.3: Taylor length scale  $\lambda$  along wall-normal direction. Filled circles are estimates of centerline values according to equation 5.8.

$$\lambda_{CL}(Re_\tau, y=y_{CL})/h \approx \frac{11}{4} Re_\tau^{-1/2}. \quad (5.8)$$

Together with the definition for the Taylor Reynolds number,

$$Re_\lambda = \frac{\lambda (2/3k)^{1/2}}{\nu}, \quad (5.9)$$

based on Taylor length  $\lambda$ , equation 5.8 yields a direct approximative relation between the two important Reynolds numbers as follows.

$$(Re_\lambda)_{CL} = \frac{11h}{4\nu} \left( \frac{2k}{3Re_\tau} \right)_{CL}^{1/2}. \quad (5.10)$$

Compared to the Kolmogorov length, Taylor length scale is an order of magnitude larger. The relationship between the two length scales at the centerline yields a scaling as function of Reynolds number as noted below,

$$\left( \frac{\lambda}{\eta} \right)_{CL} = \frac{11}{4} Re_\tau^{1/4}. \quad (5.11)$$

---

## 6 Dissipation Element Analysis

Addressing the problem of real-life turbulence from a purely mathematical point of view is not productive. Instead, physical properties of a turbulent flow may serve as an approach to characterize turbulence with its chaotic nature on the one hand, and the coherence on the other. One straightforward approach is the idea of reducing the complexity of the system by decomposing the turbulent flow field into smaller spatial units which are easier to investigate. The statistics obtained through such a decomposition would allow for an assessment of the question as to whether and how these structures are correlated.

The theory of hierarchy of turbulent scales (Richardson (1922), Kolmogorov (1941)), which assumes the turbulent flow to be composed of spatial structures of different size, is a similar idea. However, in this context this cascade bears a distinct disadvantage, namely the arbitrariness in the definition of a turbulent eddy. In fact, a natural definition of the geometrical shape of an eddy is what is needed in order for the decomposition to be non-arbitrary. With such a natural decomposition, the flow field could be partitioned into sub-units with unique geometry stemming from the physics or, in other words, determined by the turbulent field itself.

In the past there have been many approaches in this regard. For instance, based on the pressure  $p$  and the second invariant of the velocity gradient  $Q$  (equation 4.8) discussed in chapter 4, Wray & Hunt (1990) subdivided the turbulent flow field into four types of space-filling regions. Nevertheless, the decomposition of the field with this method remains artificial since the displaying isosurface levels are chosen arbitrarily which can also be seen from our results in figures 4.1 et seq.

A rather different but complementary way to classify and characterize turbulent structures is to examine critical points of the turbulent field. C. Gibson Gibson (1968) was the first to analyze in detail these properties and the behavior of points with zero-gradient and minimal gradient surfaces in a passive scalar  $\phi$  in a turbulent field. His motivation was to obtain physical and geometrical information about the smallest scales and their features in a turbulent scalar field. These are primarily determined by the

number and distribution of critical points where the scalar gradient vector vanishes, i.e

$$\nabla\phi \equiv 0. \quad (6.1)$$

Later, Gibson (see Gibson (1968)) also analyzed the mechanism by which extremal points are generated. Convective motion alone is unable to generate extremal points, since without diffusion isoscalar surfaces in a turbulent field will usually follow the fluid motion. Only a diffusion velocity of the same order of magnitude as the local convective velocity is able to restore the iso-scalar surfaces and to generate extremal points Wang & Peters (2006). From the conclusion that in scalar turbulent fields the local convective velocity is of the order of the Kolmogorov velocity, and equating it with the balancing diffusive velocity, Gibson (1968) concluded that extremal points are generated at scales of the Obukhov-Corrsin length.

Furthermore, Gibson (1968) supposed that the production of zero-gradient points by direct distortion in regions of uniform scalar gradient is due only to eddies larger than the Obukhov-Corrsin scale. For the case  $Pr \gg 1$ , the latter conclusion implies that any scale in the turbulent field is capable of generating new extremal points from regions of uniform scalar gradient since those length scales are the smallest. If  $Pr \ll 1$ , the Obukhov-Corrsin length scale is larger than the Kolmogorov length scale. Then, at the level of smallest scales, velocity perturbations are too weak to generate new zero-gradient points.

Gibson concluded that the dominant physical mechanism by which turbulence produces the small-scale features of scalar fields is the local stretching of small gradient regions. This mechanism should equally apply to strongly diffusive scalars, where the scalar diffusivity is much larger than the viscosity, as well as to weakly diffusive scalars, where the viscosity is much larger than the scalar diffusivity. Considering a 1D model problem, he pointed out that the number of maximum and minimum points must be equal whereas in 2D their sum equals the number of saddle points.

In 3D no theory is known but in the present DNS data we found that the number of maximal and minimal points are of the same order of magnitude for a turbulent channel flow as shown in a companion publication Aldudak & Oberlack (2009). However, a simple relation between critical points does not exist.

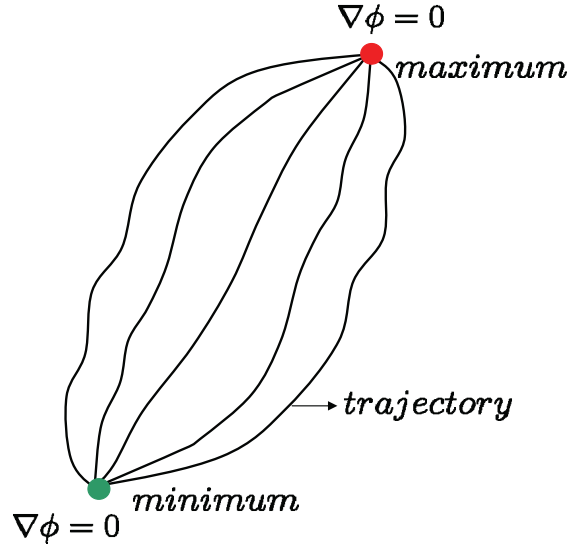


Figure 6.1: Schematic sketch of *DE*.

The present work is inspired by the work of Gibson (1968) and Wang & Peters (2006) who analyzed the small-scale statistics from passive scalar fields of homogeneous shear turbulence obtained from direct numerical simulation (DNS) by means of the dissipation element (*DE*) method. The notion refers to the tracking of gradient trajectories starting from every point in the directions of ascending and descending scalar gradients until local minimum and maximum points of the fluctuating scalar field are found (for details see Wang & Peters (2006)). The set of all points which lie on the gradient trajectories leading to the same pair of extremal points defines a dissipation element. Figure 6.1 shows a simplified illustration of a dissipation element for the 3D case. In figure 6.2, a dissipation element is illustrated using the streamwise velocity field.

Gradient trajectories, which travel along the normal direction  $\vec{n} = \nabla\phi/|\nabla\phi|$  of isoscalar surfaces in 3D, can be traced in any scalar field  $\phi(x, y, z)$  as long as the field is smooth. The trajectory is uniquely determined everywhere except at critical points, where the gradient  $\nabla\phi$  vanishes, marking the ending points of the *DE*. The Euclidean distance  $\ell$  between its extremal points and the absolute value of the scalar difference  $\Delta\phi$  at these two points are chosen to parameterize the geometry of a dissipation element.

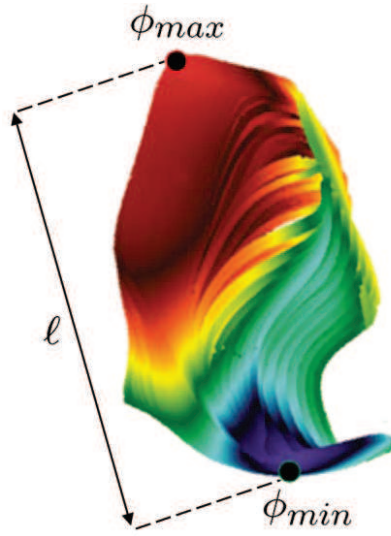


Figure 6.2: Example of *DE*.

*DE* are space-filling which means that any turbulent scalar field can be completely decomposed into such elements without any blank regions. This allows the reconstruction of certain statistical quantities of turbulence rather different from classical length scale concepts in turbulence theory, such as those based on Kolmogorov or integral length scales as discussed above.

Although these spatial structures are far from being regularly shaped, the choice of the above-mentioned parameters is reported to be appropriate by Wang & Peters (2006). We, therefore, adopt the same classification here. The authors postulate an integro-differential evolution equation for the marginal *pdf* assuming a Poisson process for the cutting of linear elements and a reconnection process due to molecular diffusion. The conditional mean of the scalar difference is shown to closely follow the inertial-range Kolmogorov scaling over a large range of length scales which is supported by our findings. Later, Wang & Peters (2008) found that while the conditional mean difference follows the inertial range Kolmogorov scaling for the passive scalar field, this is not the case for the components of the velocity.

In the latter work, the dissipation element methodology is extended to other fields in turbulence. The length scale distribution function for various turbulent fields is compared with the model equation. From their findings they concluded that the mean distance between extremal points,

which corresponds to the mean length of the dissipation elements, is of the order of the Taylor length  $\lambda$ . It is further reported that the distribution function is essentially independent of the Reynolds number. Our findings in Aldudak & Oberlack (2009) and Aldudak & Oberlack (2012) as well as the present work strongly support both these conclusions (figures 6.4, 6.16).

In the following, Dissipation Element analysis will be conducted to investigate the geometric structure of turbulent flow patterns and their statistics for various scalar fields and Reynolds numbers in the case of different channel flow configurations. The emphasis is on the plane turbulent channel flow study which will be augmented by Lie symmetry group methods to find invariant functional solutions. Additionally, turbulent channel flows with wall-normal rotation  $\Omega_y$  Mehdizadeh (2010), spanwise rotation  $\Omega_z$  Weller (2007) and wall transpiration Avsarkisov, Oberlack & Khujadze (2011) will be examined.

## 6.1 Plane Turbulent Channel Flow and Lie Group Analysis

Lie symmetry methods have been proved to be extremely important in deriving scaling laws in turbulence. This was shown by *Oberlack* in Oberlack (1999), Oberlack (2000), Oberlack (2001) by directly deriving turbulent scaling laws from principles only employing the infinite series of multi-point correlation (*MPC*) equations. In the frame work of Lie symmetry theory, these special solutions are called invariant solutions. In the latter publications, he showed that in canonical geometries, e.g. in channel flows, large-scale quantities, such as the logarithmic law of the wall, are exact solutions of the *MPC* equations.

Recently (see Oberlack & Rosteck (2010)), these ideas have been considerably extended due to the discovery that the *MPC* equations admit an even wider set of symmetries compared to the set of groups which are implied from the original set of equations, i.e. the Euler and Navier-Stokes equations. Specifically, a new scaling group and translational groups of the correlation tensors of all dependent variables have been discovered. These new statistical groups have important consequences for our understanding of turbulent scaling laws, which may be exemplarily revealed by two examples. First, it has been demonstrated that the logarithmic law fundamentally relies on one of the new translational groups. Further, with

these new symmetries at hand all higher *MPC*, which include classical one-point quantities such as the turbulent stresses, may be derived. Second, it was demonstrated that the recently discovered exponential decay law of isotropic turbulence generated by fractal grids (see Hurst & Vassilicos (2007), Seoud & Vassilicos (2007)) is only admissible with the new statistical scaling symmetry.

In particular, the latter result of an exponential decay cannot be derived from the two classical scaling groups implied by the fundamental equations of fluid motion, which has dictated our understanding of turbulence decay since the early 1930s, as implicated by the von-Kármán-Howarth equation.

Employing commutator theory and generating three more sets of symmetries, the latter findings of new statistical Lie symmetry groups for the *MPC* have been obtained which, together with the known symmetries of Euler and Navier-Stokes equations form a Lie algebra (Rosteck & Oberlack (2011)). These results will formally be applied to *DE*.

It is of particular interest to examine how the *DE* statistics change in wall dominated shear turbulence. To do this, firstly, the channel half height  $h$  is subdivided into wall-normal viscous, buffer, logarithmic and core regions as described in §3 and secondly,  $h$  is partitioned equidistantly (hereafter referred to as the *characteristic* and *equidistant* layers). Both division types are seen to be complementary. The first one is aimed to account for very thin near-wall layers at high Reynolds number  $Re$  while the equidistant division results in finer layers in the broad core region, thus enabling a more nuanced analysis. For instance, the buffer layer ( $5 < y^+ < 30$ ) amounts to only 1,7% of the channel half height  $h$  at the highest  $Re_\tau = 1440$  case, the viscous sublayer with 0.4% even less. On account of this, the viscous sublayer next to the wall is excluded from the analysis of the characteristic layers.

In order to comprehend the scaling properties of the *DE pdf*, we should first reconsider the scaling symmetries of the Navier-Stokes, or rather, the Euler equations. In the large Reynolds number limit, the Navier-Stokes equations (1.2) and (1.1) admit the two independent transformation groups of scaling

$$\begin{aligned}
 T_1 : t^* &= t , \\
 \mathbf{x}^* &= e^{a_1} \mathbf{x} , \\
 \mathbf{U}^* &= e^{a_1} \mathbf{U} , \\
 p^* &= e^{2a_1} p ,
 \end{aligned} \tag{6.2}$$



$$\begin{aligned}
T_2 : t^* &= e^{a_2 t} , \\
x^* &= x , \\
\mathbf{U}^* &= e^{-a_2} \mathbf{U} , \\
p^* &= e^{-2a_2} p ,
\end{aligned} \tag{6.3}$$

where  $a_1, a_2 \in \mathbb{R}$  are independent group-parameters. These transformations refer to symmetry groups, meaning that their substitution into the Navier-Stokes equations (1.2) and (1.1) (in the limit  $1/Re_\tau \rightarrow 0$ ) leads to identical equations written in the new variables denoted by the asterisk.

Apart from the latter two groups, the Euler and Navier-Stokes equations admit the group of translation, i.e. any shift of origin leaves these equations unchanged. The corresponding transformation reads

$$\begin{aligned}
T_3 : t^* &= t , \\
x^* &= x + \mathbf{a} , \\
\mathbf{U}^* &= \mathbf{U} , \\
p^* &= p ,
\end{aligned} \tag{6.4}$$

and, as is apparent, this is also a symmetry transformation of (1.1) and (1.2). A complete list of all symmetries of the Euler and Navier-Stokes equations is given in Oberlack (2000).

It is in particular the above two scaling groups, (6.2) and (6.3), and their combinations that form the basis for many turbulent scaling laws in the group theory, called invariant solutions (see e.g. Oberlack (1999), Oberlack (2000), Oberlack (2001), Oberlack & Rosteck (2010), Rosteck & Oberlack (2011)).

This is true both for small-scale turbulence and the Kolmogorov law (see Ünal (1994)), as well as for scaling laws of large scale quantities such as of wall-bounded shear flows. In particular, for a turbulent channel flow it has been shown in Oberlack (2000), Oberlack (2001) that, both for the log region and for the algebraic law in the core region, scaling of space according to  $T_1$  with the group parameter  $a_1$  is the key property. In respect to their scaling properties the two cases are distinguished by the scaling of time  $T_2$ .

This may best be observed by reconsidering the invariant surface condition for the mean velocity for wall-bounded plane shear flows which has the form

$$\frac{dy}{a_1 y + a_3} = \frac{d\bar{u}}{(a_1 - a_2)\bar{u} + a_4} \tag{6.5}$$

(see Oberlack (2001)). Apparently, for the log-law we have  $a_2 = a_1$  while for the algebraic law we have  $a_2 = na_1$  for a fixed given value of  $n$ . Regardless of which mean flow scaling law is active in the respective flow regime, we always have a scaling of space in the wall-normal direction according to (6.2)

$$y^* = e^{a_1} y \quad (6.6)$$

which is in fact true for all length scales. Therefore, this is also valid for the length scale of the *DE*

$$\ell^* = e^{a_1} \ell \quad (6.7)$$

where  $\ell$  is the Euclidean length of the *DE*.

From (6.4) we also obtain the translational group for  $y$

$$y^* = y + a_3, \quad (6.8)$$

which will be employed subsequently.

For the analysis of the *DE* statistics Wang & Peters (2006) introduced the *pdf* or, respectively, the conditional *pdf* as the main quantity. In the homogeneous flow, which was investigated therein, the *pdf* is only a function of the *DE* length, Reynolds number and perhaps a time scale ratio between turbulent and shear time scales.

As derived in Aldudak & Oberlack (2012), for the present flow case, any statistical quantity depends on the wall normal distance  $y$  and the Reynolds number  $Re_\tau$  as parameters, and hence the formal *pdf* for the length scale distribution is of the form

$$P(\ell; y, Re_\tau) \quad (6.9)$$

where the Euclidean length  $\ell$  is now referring to the sample space variable.

The usual *pdf* normalization condition

$$\int_0^\infty P \, d\ell = 1 \quad (6.10)$$

together with the length scale scaling (6.7) implies a scaling of the *pdf* of the form

$$P^* = e^{-a_1} P. \quad (6.11)$$

Further, defining the mean or expectation value for the *DE*

$$\ell_m = \int_0^\infty \ell P \, d\ell \quad (6.12)$$

we instantly obtain the scaling

$$\ell_m^* = e^{a_1} \ell_m. \quad (6.13)$$

With the two key assertions of Lie symmetry theory one arrives at following (see Aldudak & Oberlack (2012));

1. Any concatenation of two or more symmetry groups of a given problem or differential equation is again a symmetry group. However, it is now a multi-parameter symmetry group. For example from (6.2) and (6.3) we obtain the multi-parameter group:

$$\begin{aligned} T_{1,2} : \quad t^* &= e^{a_2} t, \\ \mathbf{x}^* &= e^{a_1} \mathbf{x}, \\ \mathbf{U}^* &= e^{a_1 - a_2} \mathbf{U}, \\ p^* &= e^{2(a_1 - a_2)} p, \end{aligned} \quad (6.14)$$

which, implemented in (1.1) and (1.2), constitutes a symmetry group.

2. Any invariant under a given group, i.e. a quantity which does not change form under a given symmetry group, may allow a reduction of parameter space. E.g. the quantity  $\tilde{\mathbf{U}} = \mathbf{U}t$  is an invariant with respect to the symmetry (6.3) since its implementation in the latter leads to  $\tilde{\mathbf{U}} = \mathbf{U}t = \mathbf{U}^*t^* = \tilde{\mathbf{U}}^*$ . These properties of groups are in fact also true for any combination of symmetry groups. These may be invoked as new independent variables, which then lead to invariant solution under the above scaling group, often denoted similarity-solution.

With these assertions in mind, we may now construct the invariant solution of the *DE pdf* by using (6.7), (6.11) and (6.13) to obtain the invariants  $\tilde{\ell} = \frac{\ell}{\ell_m}$  and  $\tilde{P} = \ell_m P$ . Solving for  $P$  yields the invariant solution

$$P = \frac{\tilde{P} \left( \frac{\ell}{\ell_m} \right)}{\ell_m}. \quad (6.15)$$

Here, however, the  $y$  dependence is still hidden and we should now consider the combined scaling and translational group of  $y$ , i.e. (6.6) and (6.8), in conjunction with the selfsame scaling for  $\ell_m$ , namely equation (6.13). With this we obtain the invariant form of  $\ell_m$

$$\ell_m \sim y + c \quad (6.16)$$

where the constant  $c$  emerged due to the combined group parameters  $a_1$  and  $a_3$ . With this at hand, we derive the alternative form of the *pdf* scaling law (6.15) given by

$$P = \frac{\tilde{P}\left(\frac{\ell}{y+c}\right)}{y+c}. \quad (6.17)$$

A complete derivation of the present theory based on the key quantities of Lie theory such as infinitesimal transformations, invariant surface condition, etc. is given in appendix A.

### 6.1.1 Validation of the Dissipation Element Scaling Laws

Before investigating the new scaling laws above in detail, we first (a) examine the DNS data in table 2.1 with respect to isotropy or anisotropy of the *DE pdf* and, in a second step (b), the Reynolds number dependence of the *DE pdf*.

To understand both the issues (a) and (b), the figures in 6.3 and 6.4 illustrate the marginal probability densities  $\tilde{P}(\ell/\ell_m)$  of the Euclidean length of the *DE* of the entire channel. Here the scalar fields which are studied are the turbulent kinetic energy  $k$ , its dissipation rate  $\epsilon$ , and the fluctuations of the velocity components ( $u, v, w$ ) at four different Reynolds numbers ( $Re_\tau$ ). Here, the *pdf* have been properly normalized using (6.10), and all length scales are rescaled by the mean length  $\ell_m$  of the entire channel, according to (6.12).

The distribution of the *pdfs* is essentially log-normal as it will be outlined further below. The curves show a very steep algebraic rise with an increase of the element size for small *DE* for all cases, and an exponential decay for larger elements after reaching a maximum at around  $\ell \approx 0.6\ell_m$ . Hence, the *DE* length scale which is associated with the highest probability is, as to be expected, in the order of the mean length.

Related to the issue (a) of isotropy/anisotropy above, it is also interesting to note that the curves for all five scalars have remarkably coinciding shapes. From the linear plot in figure 6.3, particularly, matching curves are observed for  $k, u$  and  $\epsilon$ . However, for large length scales, taken from the semi-logarithmic plot, it appears that  $u$  and  $w$  profiles are closer together and apparently decay faster than the *pdf* for  $k, v$ , and  $\epsilon$ . The *pdf* of the wall-normal velocity component  $v$  shows a minor deviation from other distributions. Still, a remarkable insensitivity related to the choice

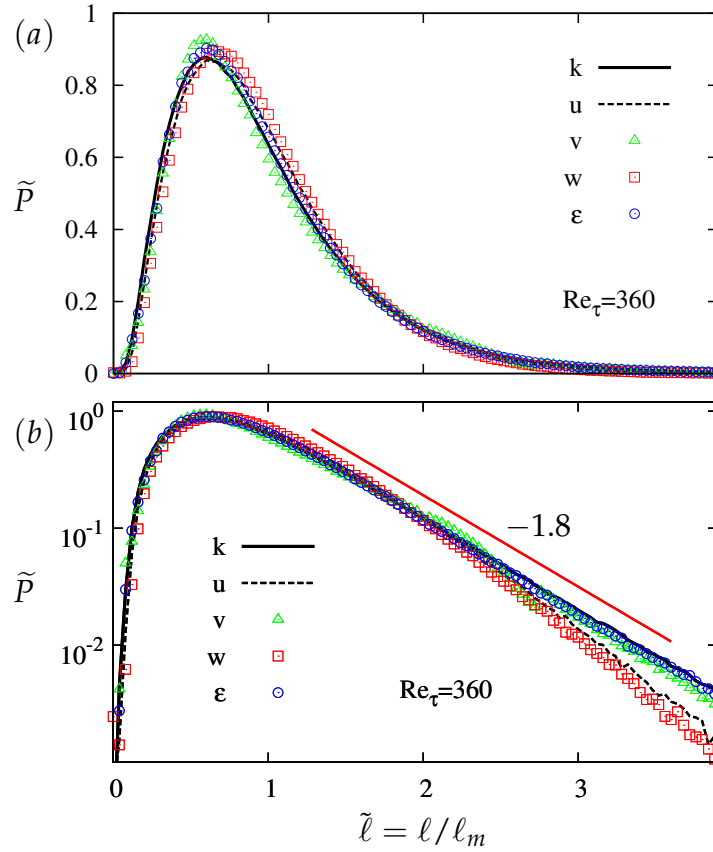


Figure 6.3: Comparison of the overall *pdf* of the entire channel for different scalar variables.

of the scalar variable is observed, implying a large degree of *DE* isotropy which is in fact true for small as well as for large scale of *DE*. This is, in fact, a very interesting outcome considering the different natures of the individual scalar variables such as the strong intermittent character of the dissipation rate  $\epsilon$ .

An even more remarkable insensitivity with respect to different Reynolds numbers may be taken from the figure 6.4. Curves from all *Re* almost perfectly coincide which is also unexpected, since the considered Reynolds number range is quite large. The lowest and highest *Re* are a factor of four apart, thus justifying a general statement.

Below, we intend to validate the scaling laws (6.15) and (6.16) or respectively (6.17) with the channel flow DNS data. To this end, we focus on the region of validity of the above scaling laws, i.e. the log-region and

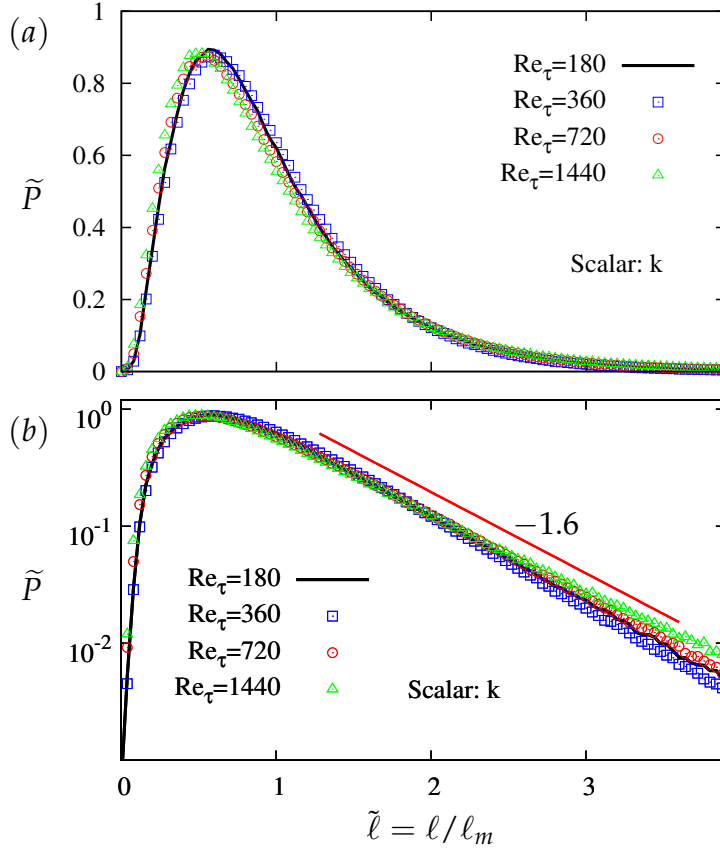


Figure 6.4: Comparison of the overall *pdf* of the entire channel for different  $Re_\tau$ .

the algebraic region in the core of the channel. Therein, we rescale the data for the logarithmic and core regions, and plot them according to the rescaled *pdf*  $\tilde{P} = \tilde{P}(\tilde{\ell})$  in (6.15). In order to properly accentuate this behavior, we split the channel into five equidistant wall-normal layers with an increment of 0.2 in the normalized wall distance  $y/h$ .

In figure 6.5, *pdf* profiles for five adjacent layers from the most wall adjacent layer ( $0.0 < y/h < 0.2$ ) to the channel center ( $0.8 < y/h < 1.0$ ) are displayed for highest *Re* case,  $Re_\tau = 1440$ .

While in the upper picture the *pdf*  $P$  is only normalized according to (6.10), in the picture below the length scale has also been normalized by the corresponding local mean length  $\ell_m$ . In other words, we plot the similarity variable  $\tilde{P}$  from equation (6.15).

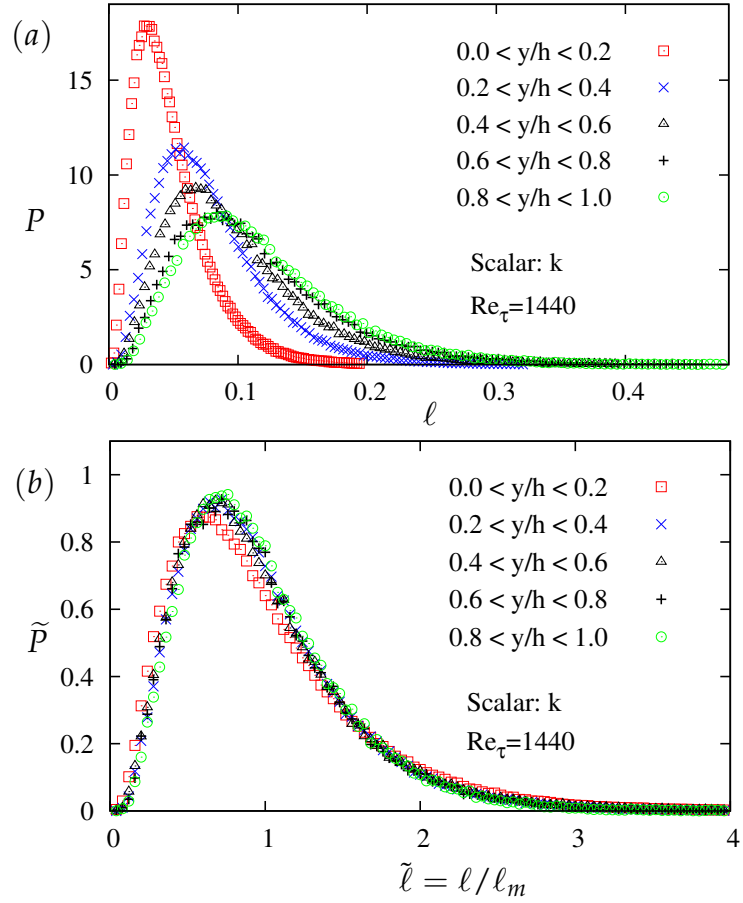


Figure 6.5: Pdf for equidistant wall-normal layers where in (a)  $\ell$  is not normalized while in (b)  $\ell$  is normalized with  $\ell_m$  at  $Re_\tau = 1440$ .

When the length scale  $\ell$  is not normalized, figure 6.5(a) indicates distinctive differences in the pdf curves with respect to the distance to the wall. Larger elements are seen to be located preferentially in the far-wall layers, as indicated by the pdf for the core region where the maximum peak and the far-tail of the pdf are shifted to larger elements. By the same token, small elements will be found mostly near the wall. This is consistent with the findings in figure 6.13 where the mean DE length  $\ell_m$  is plotted against the wall-normal distance. Its linear rise in layers away from the wall is an indication of their wider spectrum of length scales compared to regions closer to the wall, where the shape of the pdf becomes narrower. Furthermore, the higher peak values of the pdf towards the wall suggest that there are more DE approaching the wall. Note that the volume of

each equidistant layer is equal. Recalling the space-filling character of  $DE$ , thus, one can assume small, numerous elements close to the wall which increase in size but decrease in quantity.

The strong influence of the wall is very obvious considering the relative differences between neighboring layers. While the change from the first near-wall layer to the next one is enormous, it is retarded with increasing distance from the wall.

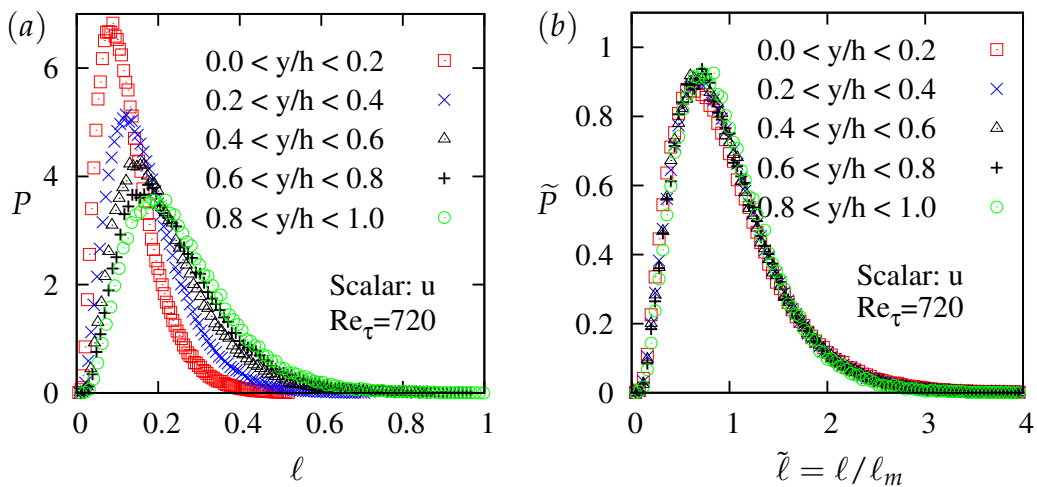


Figure 6.6: Same as in figure 6.5. But for scalar  $u$  and  $Re_\tau = 720$ .

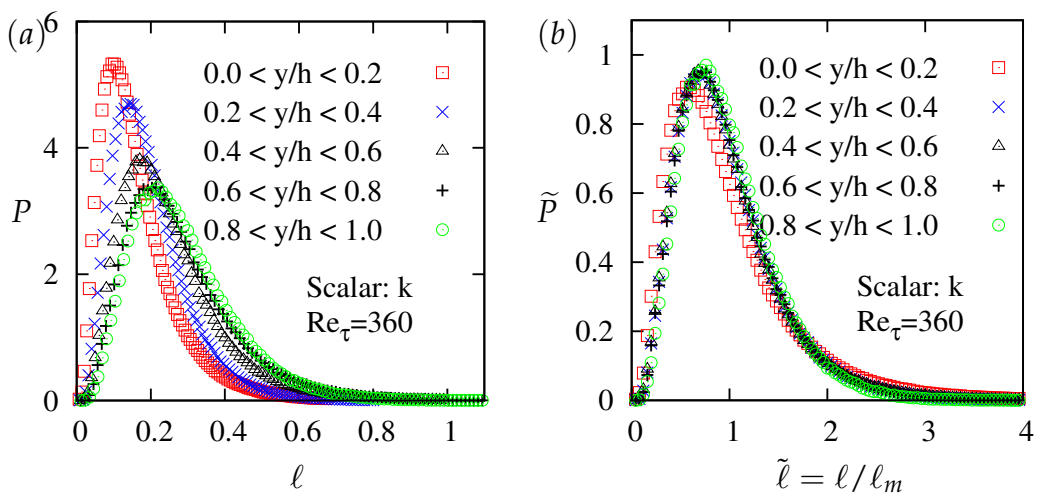


Figure 6.7: Same as in figure 6.5. But for  $Re_\tau = 360$ .



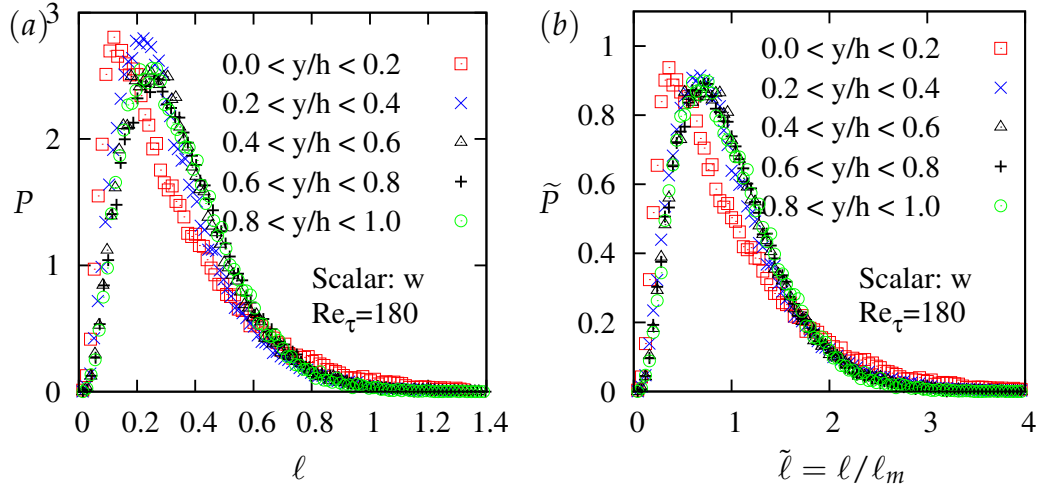


Figure 6.8: Same as in figure 6.5. But for scalar  $w$  and  $Re_\tau = 180$ .

Figures 6.6(a), 6.7(a) and 6.8(a) without normalization confirm this behavior for different Reynolds numbers. This is even true for the lowest  $Re$  case, although less markedly.

In pictures 6.5(a) and 6.7(a), the same scalar variable, namely the kinetic energy  $k$ , is shown for  $Re_\tau = 1440$  and  $Re_\tau = 360$ , respectively. A direct comparison of both figures gives the first evidence of the effect of the Reynolds number. First, more elements are produced in the higher  $Re$  case which can be deduced from the significantly larger peak values in all layers. Second, the elements become obviously smaller with increasing  $Re$  as indicated by the shorter far-tails in 6.5. The  $pdf$  profiles in 6.6(a) and 6.8(a) illustrate exemplary the same characteristics for other variables such as the velocity components  $u$  and  $w$  at different  $Re$ .

In contrast to this, figures (6.5, 6.6, 6.7 and 6.8)(b) show that if the  $DE$  length is normalized with the mean length  $l_m$  of the respective layer, the curves coincide very well, especially for the region  $0.2 \leq y/h < 1.0$ . This collapse is a strong indication for the invariant solution (6.15) or (6.17). The  $pdf$  for the layer most adjacent to the wall is noticeably different from the others due to the influence of the solid walls.

For further analysis of the  $pdfs$ , we investigate their behavior in distinguished characteristic channel flow layers mentioned above. Again, we use for the normalization of the length scale the corresponding local mean length  $l_m$  of the current layer according to (6.15).

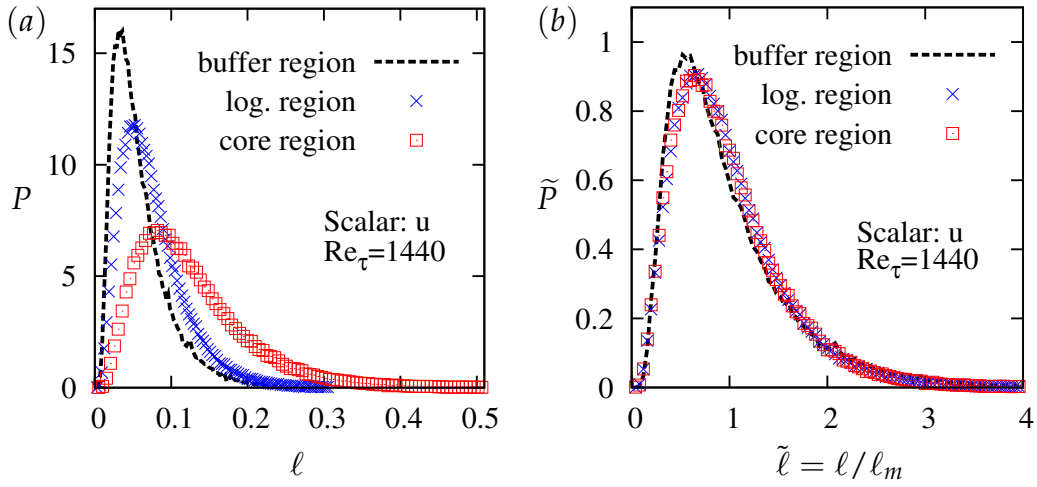


Figure 6.9: Pdf for characteristic wall-normal layers at  $Re_\tau = 1440$ . Again, in (a)  $l$  is not normalized while in (b)  $l$  is normalized with  $l_m$ .

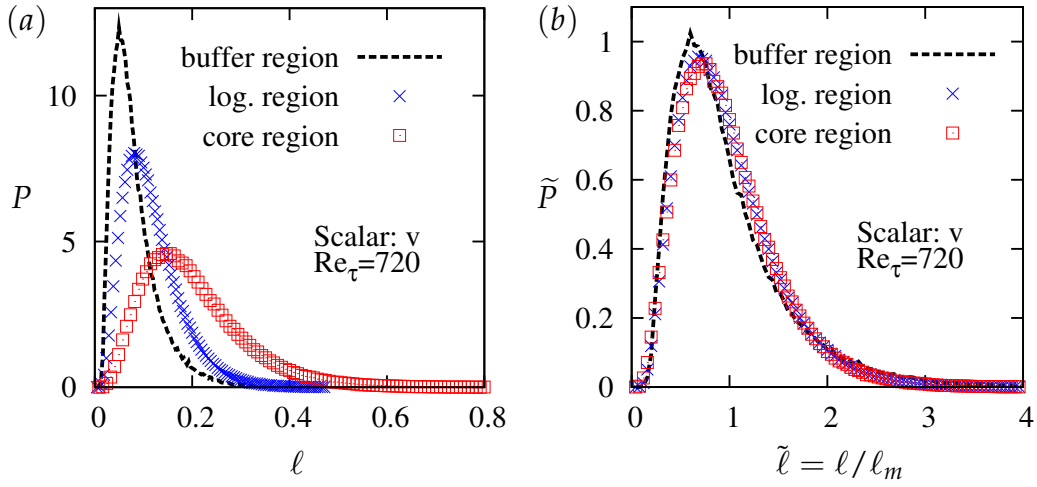


Figure 6.10: Same as in figure 6.9. But for scalar  $v$  and  $Re_\tau = 720$ .

The same self-similar behavior of *pdfs* after normalization, as observed in equidistant layers, can also be taken from pictures 6.9, 6.10, 6.11 and 6.12, which show a remarkable collapse of the *pdf* profiles for the logarithmic and the core regions of the channel. On the other hand, the near-wall buffer layer departs significantly as a result of wall-boundary effects which applies to all variables and  $Re$ . After normalization, the *pdf* is shifted towards small elements, meaning that this layer contains more

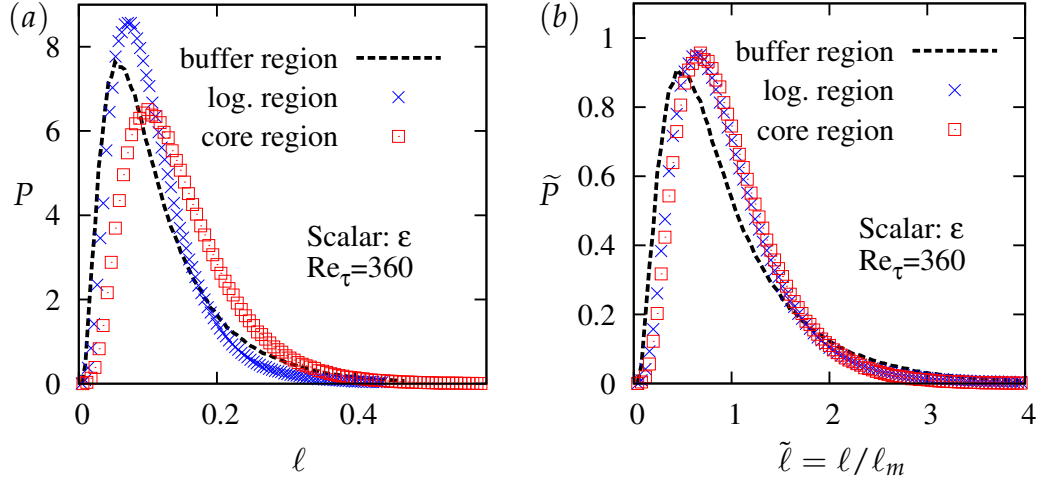


Figure 6.11: Same as in figure 6.9. But for scalar  $\epsilon$  and  $Re_\tau = 360$ .

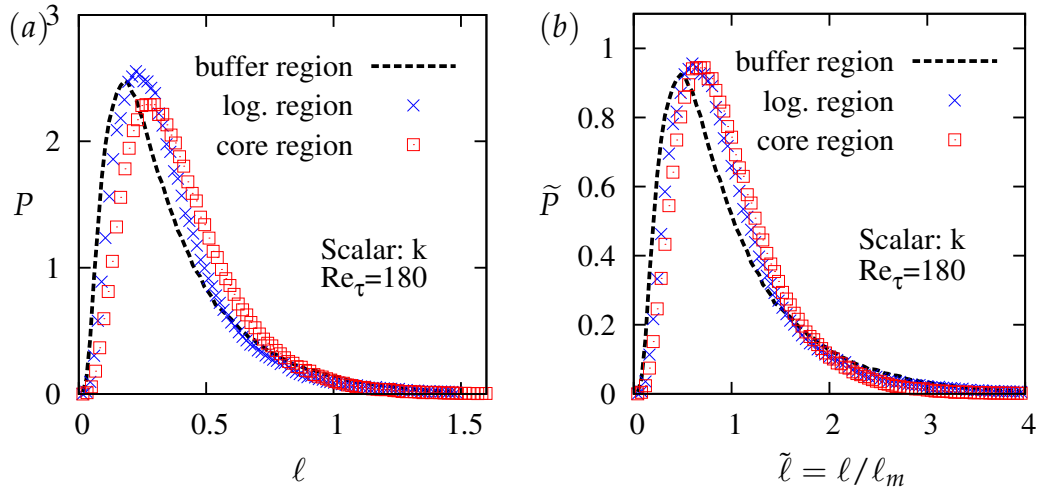


Figure 6.12: Same as in figure 6.9. But for scalar  $k$  and  $Re_\tau = 180$ .

elements that are smaller than its local mean length scale compared to the layers beyond  $y^+ = 30$ . In general, the buffer layer seems to contain more elements than the layers above. Interestingly, however, the dissipation rate  $\epsilon$  appears to be special in this respect, since it exhibits more elements in the intermediate logarithmic layer (see figure 6.11(a)). Nonetheless,  $\epsilon$  too is subject to the self-similarity.

Figures 6.13(a),(b) depict the mean  $DE$  length  $\ell_m$  versus the wall-normal  $y$  direction. First of all, it can be deduced that all curves obey a charac-

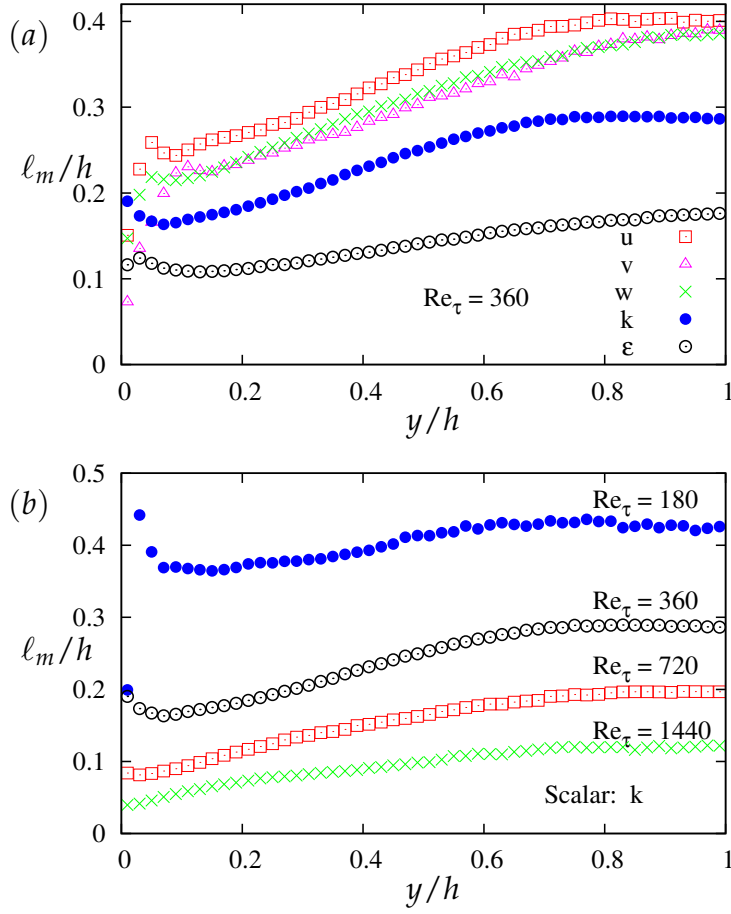


Figure 6.13: Mean length  $\ell_m$  of DEs varying with the wall-normal direction  $y$  for different (a) scalar variables and (b)  $Re$ . Note that  $h = 1$  is the channel half-height.

teristic profile, that is, a sudden increase of the element size near the wall, a subsequent linear rise and finally a nearly constant center region. The wall, or the high turbulent intensity especially in the buffer layer, has a strong impact on the course of the DE length in the wall vicinity. Here,  $\ell_m$  reaches a maximum after which it drops at around  $y^+ = 20$ .

Despite these mutualities, in (a), where  $\ell_m$  is plotted for several scalar variables at  $Re_\tau = 360$ , it can be seen that there exist enormous differences in the DE size of different variables. Hence, considering the fact that the length of a DE is the Euclidean length between its extremal points, one can conclude that the production of these extremal points, where  $\nabla\phi = 0$ ,

is strongly coupled to the choice of the scalar variable  $\phi$  which will be discussed later in detail.

The scalar field  $u$  appears to have the largest elements for a given Reynolds number, followed by the other two velocity components  $v$  and  $w$ , both being very similar except in the near-wall region. The scalar field of the dissipation rate has the smallest elements which conforms with its known intermittent nature leading to a higher production rate of extremal points. Since *DEs* are space-filling, one can simply argue that the smaller *DEs* are, the higher their number will be.

The profiles of the mean *DE* length  $\ell_m$  is reminiscent of the classical Kolmogorov ( $\eta$ ) and Taylor ( $\lambda$ ) length scales as functions of  $y$  as plotted in pictures 5.1 and 5.3 in chapter 5. Similar to  $\eta$  and  $\lambda$ , the size of the *DE* length scales decreases with increasing Reynolds number as can be seen from figure 6.13(b) where the scalar variable is the kinetic energy  $k$ . The key advantage of *DE* length scale compared to others is that their number can be precisely determined since they completely occupy the domain.

The intermediate region with linear relation between  $\ell_m$  and  $y$  has been represented by equation (6.16). The latter is part of the basis for the *pdf* scaling laws (6.15) or rather (6.17), and we also see that the linear scaling is only confirmed in a region excluding the very center region of the channel and, of course, the near-wall region.

Interestingly, the center section behavior implies a remarkable result, as it gives rise to an extended similarity behavior for  $\tilde{P}(\tilde{\ell})$ . The reason is that, since similarity is clearly observed for all regions between  $0.2 \leq y/h \leq 1.0$  in figures (6.5, 6.6, 6.7, 6.8)(b), even for the very center layer, this is not directly supported by the finding in figures 6.13(a),(b) in connection with the scaling laws (6.15) or (6.17). Since (6.15) or (6.17) are based on the linear scaling relating  $\ell_m$  and  $y$ , one would expect a clear deviation for the *pdf* in the very center layer. However, only a tiny variation from the *pdfs* taken outside the central region is detected.

As shown above,  $\ell_m$  is clearly a function of the wall-normal distance, the Reynolds number and the choice of the scalar such that

$$\ell_m = f(y, Re_\tau, \phi) \quad (6.18)$$

In the following, analytical expressions of the mean *DE* length are derived for the linear scaling range where *pdfs* exhibit similarity behavior.

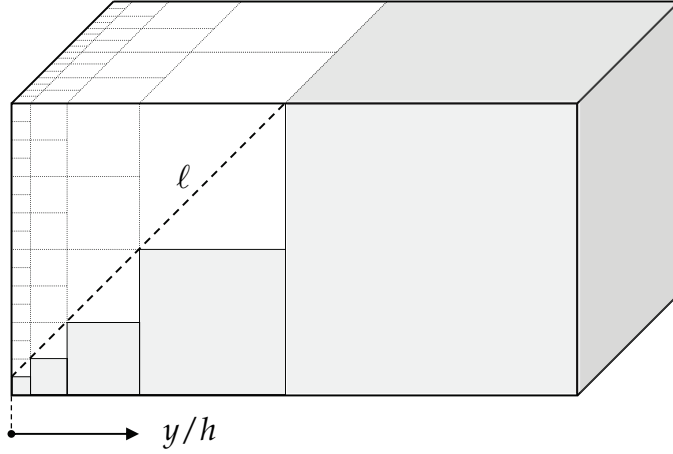


Figure 6.14: Sketch of the *DEs* in a turbulent channel flow approximated as cubes.

$$\ell_{m,k}/h = 6.58 Re_{\tau}^{-0.66} + 9.71 Re_{\tau}^{-0.63} y/h \quad (6.19)$$

$$\ell_{m,u}/h = 20.65 Re_{\tau}^{-0.78} + 10.41 Re_{\tau}^{-0.62} y/h \quad (6.20)$$

$$\ell_{m,v}/h = 12.86 Re_{\tau}^{-0.72} + 7.98 Re_{\tau}^{-0.60} y/h \quad (6.21)$$

$$\ell_{m,w}/h = 12.47 Re_{\tau}^{-0.71} + 11.98 Re_{\tau}^{-0.65} y/h \quad (6.22)$$

These equations containing all dependencies are needed later to formulate a log-normal model for *DE pdfs* .

The property of *DEs* that they have a clear geometric definition of a three-dimensional structure will subsequently be employed to estimate the number of *DEs*,  $N$ , as a function of the wall distance  $y$ . For this, we utilize the linear scaling between  $\ell$  and  $y$  and take the rather simplifying assumption that *DE* fill cubic sub-volumes as shown in figure 6.14. From this figure, we may take as a first step the relation between the  $n^{\text{th}}$  element and the distance to the wall which is a geometric series

$$2^n - 1 \sim y + c. \quad (6.23)$$

Now, in a second step, counting the number of elements at the position  $n$  we arrive at the number of *DEs*

$$N \sim 2^{2n}, \quad (6.24)$$

where the proportionality factor is measure of the channel size. Combining (6.23) and (6.24), we find the scaling relation

$$N(y) = \frac{b}{(y + a)^2}, \quad (6.25)$$

where  $a$  and  $b$  are constants which are functions of  $Re_\tau$  and  $\phi$ . This scaling law is nicely validated in figures 6.15(a) and (b).  $N$  is rescaled with channel dimensions, representing number of elements in a unit cube ( $1^3$ ), to allow for comparison of results from domains of different sizes. Weak deviations are only visible in the near wall region and in the very center of the channel, where the linear scaling is excluded regardless as is observed in figures 6.13(a),(b).

The plots for the number of  $DE$  confirm the conclusions drawn earlier with respect to the  $pdf$  and the mean length distribution  $\ell_m$  depending on the wall-normal distance. To this end, most elements are created always in the vicinity of the wall due to the higher turbulence intensity. Is the channel core approached, the number of elements drops significantly in connection with an increase of the size. Apart from the near-wall region where deviations occur due to the anisotropy induced by the wall boundary (see figures 3.4, 3.5 in chapter 3), all velocity components feature comparable numbers of elements at a given  $Re$  (figure 6.15(a)). From figure 6.15(b), one can argue that the generation of  $DEs$  clearly depends on the  $Re$ . As already deduced, with growing  $Re$ , i.e. degree of turbulence intensity, more elements are created which on the other hand become smaller.

Having established that the generation of  $DEs$  and extremal point, respectively, depends on the  $Re$ , the wall-normal direction  $y$  and the choice of the scalar field  $\phi$  together with the scaling relation 6.25, we can formulate the following approximation for  $N(y, Re_\tau, \phi)$  which is validated by the two solid lines in the pictures 6.15(a),(b),

$$N_\phi(y, Re_\tau) = \frac{b_\phi(Re_\tau)}{(y + a_\phi)^2}. \quad (6.26)$$

As pointed out, the length of a dissipation element is defined by the linear length between adjacent minimal and maximal points, respectively. Hence, saddle points are not taken into account, though these too are critical points with  $\nabla\phi = 0$ . Though simple relations between minimal, maximal, and saddle points exist for one and two dimensions, no simple

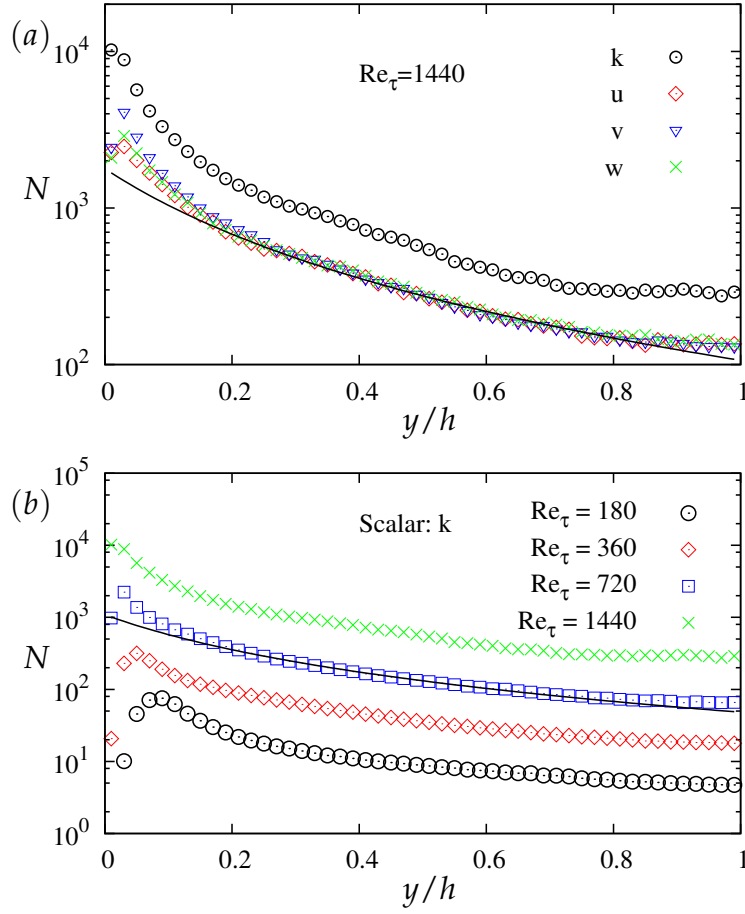


Figure 6.15: Number  $N$  of DE per unit cube ( $l^3$ ) as function of the wall-normal direction  $y$  (a) for different variables, (b) for different  $Re$ . Solid lines represent the fit curve according the approximation 6.26.

Scalar $\phi$	$k$	$u$	$v$	$w$
$b_\phi(Re_\tau)$	$1.2 \cdot 10^{-4} Re_\tau^{2.04}$	$2.5 \cdot 10^{-6} Re_\tau^{2.50}$	$1.7 \cdot 10^{-4} Re_\tau^{1.87}$	$1.6 \cdot 10^{-5} Re_\tau^{2.21}$
$a_\phi$	0.281	0.323	0.260	0.295

Table 6.1: Coefficients of the scaling relation 6.25 for  $N$ .

counting relations exist in three dimensions, not even for Morse fields (see Peters & Wang (2006)). Hence, only statistical measures may be invoked to count critical points for the present three-dimensional flow problem. In fact, the DNS data clearly indicate that the number of minimal and maxi-



mal points are identical. Additionally, they are indistinguishable from the number of *DE* as plotted in figure 6.15. Hence, any further analysis of the distribution of these points is omitted.

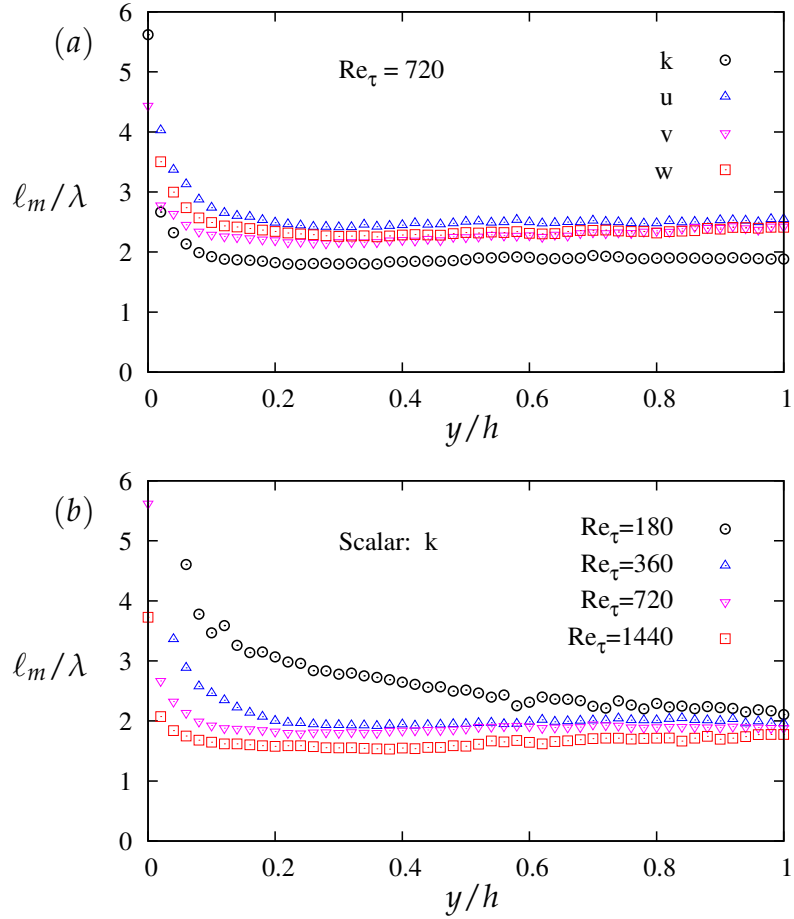


Figure 6.16: Ratio of the mean *DE* length  $\ell_m$  and Taylor length scale  $\lambda$  as a function of the channel height (a) for different variables, (b) for different  $Re$ .

In the context of *DE* analysis, a possible link between *DE* and classical length scales, in particular the Taylor length scale, is investigated subsequently for the turbulent channel flow.

A first estimate in this respect was given in Wang & Peters (2006) where it was concluded that the expectation value of the *DE* distribution is proportional to the Taylor length scale, i.e.

$$\ell_m \sim \lambda, \quad (6.27)$$

specifying a link to classical turbulent length scales. In order to validate this conclusion, we plot the ratio  $\ell_m/\lambda$  as a function of the wall-normal direction (figure 6.16). This nicely reveals that - especially in higher  $Re$  cases - for a large portion of the channel height the mean length  $\ell_m$  scales very well with the Taylor length scale  $\lambda$ , substantiating the above relation (6.27).

Sufficiently far from the wall, the plots show an essentially constant profile up to the channel center. Nevertheless, on approaching the wall this feature seems to vanish, such that the near-wall viscous and buffer layers are excluded. It is interesting to note that in the subplot (a) the profiles of all velocity components collapse at the centerline in spite of the deviations near the wall. It can therefore be concluded that, for a fixed  $Re$ ,  $DEs$  at the centerline are to a strong degree independent of the direction of the velocity. The lowest  $Re_\tau = 180$  case is in reasonable, but less, agreement with these findings, and low- $Re$  effects are clearly noticeable.

Figure 6.16(b) suggests that by increasing the Reynolds number the profiles of  $\ell_m/\lambda$  will approach each other further. Based on the two lower  $Re$  cases, Aldudak & Oberlack (2012) argue that the plots for the same scalar but different  $Re$  approximate each other towards the channel center. This is further augmented by the two higher  $Re$  cases. The ratio  $\ell_m/\lambda$  obviously tends to a centerline value which can be assumed to be nearly constant, i.e. weakly dependent of the  $Re$ . It is interesting that this tendency is observable even for the smallest  $Re$ . This coincides with the fact that the channel core region is the one most insensitive to the  $Re$  effects.

For the sake of completeness, the ratio between the  $DE$  and the Kolmogorov length scales is depicted in figure 6.17 showing several variables at  $Re_\tau = 720$ . Compared to the counterpart figure 6.16(a), the scaling behavior is less suitable.

## 6.1.2 Log-normal Pdf Model

As already noted above, the *pdfs* of  $DE$  length reveal a skewed distribution rather than a bell-shaped, symmetrical Gaussian distribution. In a characteristic manner, skewed distributions point out non-negative values and large variances. A typical skewed distribution is the log-normal distribution, which fits the probability density of various processes in nature. A random process is log-normally distributed, by definition, if its loga-

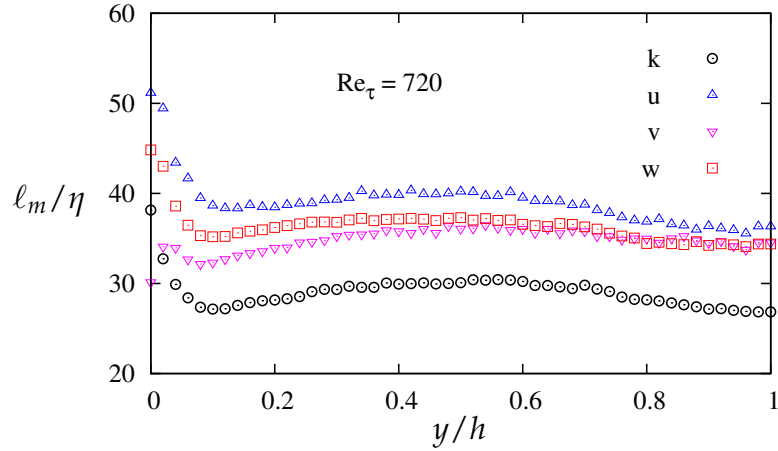


Figure 6.17: Ratio of the mean  $DE$  length  $\ell_m$  and Kolmogorov length scale  $\eta$  against the wall-normal distance for different variables.

rithm agrees with the Gaussian distribution. Hence, all values are positive and the curve of the  $pdf$  is shifted to the left.

The log-normal  $pdf$  of a random variable, here  $\ell$ , is described as

$$P(\ell) = \frac{1}{\ell\sigma\sqrt{2\pi}} \exp\left(-\frac{(\ln(\ell) - \mu)^2}{2\sigma^2}\right), \quad \ell > 0, \quad (6.28)$$

where the parameters  $\sigma$  and  $\mu$  are a measure of the expectation value and the variance, respectively, and fully specify the shape of the  $pdf$ .

Under these conditions, we now examine the relation between  $DE$  length and log-normal probability densities. As evident from figure 6.18,  $DE$   $pdf$ s closely fit the log-normal distribution. In figure 6.18 (a) overall  $pdf$ s of different scalar variables are displayed in a semi-logarithmic plot together with the log-normal fit for the scalar  $u$  as an example. First of all, the picture emphasizes that the  $DE$   $pdf$  closely follows a log-normal distribution. Minor deviations are only visible towards the origin, where the element size is small. Upon logarithmic scaling of the horizontal axis, a second important aspect makes itself apparent. All  $DE$   $pdf$ s follow the symmetrical, normal distribution of the log-normal  $pdf$ , limited deviations notwithstanding.

The example in figure 6.18 (b) shows  $pdf$ s of equidistant wall-normal layers for  $u$ , highlighting an almost perfect fit by means of log-normal  $pdf$ s. Adjusting the two shape parameters  $\sigma$  and  $\mu$ , the  $pdf$  can be fitted properly

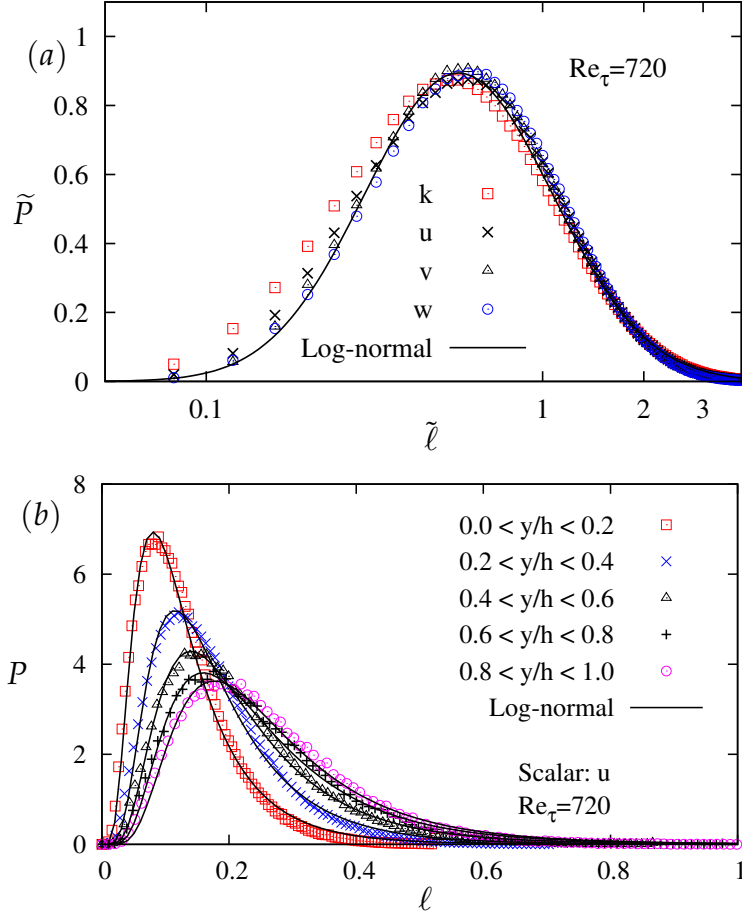


Figure 6.18: (a) Overall *pdf* of different scalar variables in semi-log plot; (b) *pdf* of equidistant wall-normal layers with related log-normal fit.

for the respective wall-normal layer. As a result, it is examined whether these shape parameters can be written as functions of  $y/h$ . This allows us to derive a simple log-normal model which is also a function of the distance from the wall and, thus accounts for the known wall-normal dependence of the *DE pdf*.

In Aldudak & Oberlack (2012) we found for the  $Re_\tau = 360$  case that the parameter  $\sigma$  can be regarded as independent of the choice of the scalar variable  $\phi$  whilst  $\mu$  scales logarithmically with the distance to the wall  $y$ . The latter was, moreover, a function of  $\phi$ . Presently, these findings are supplemented with an additional Reynolds number dependence.

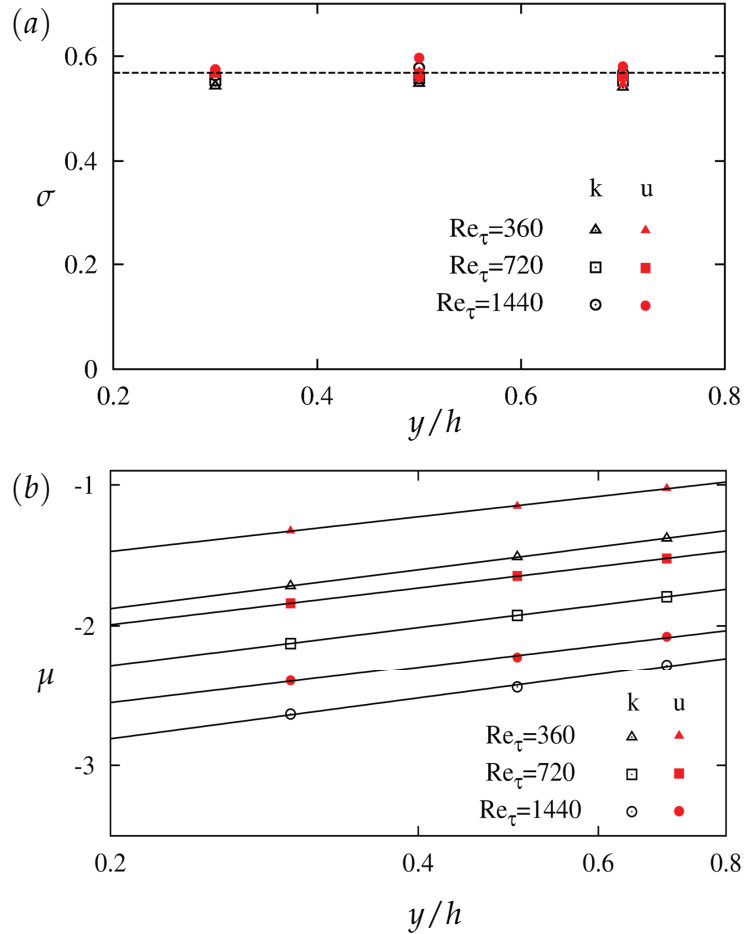


Figure 6.19: Shape parameters  $\sigma$  and  $\mu$  as functions of  $y/h$  for two scalar variables at different  $Re$ .

As shown in figures 6.3 and 6.4, overall *pdfs* representing the entire channel are insensitive to the choice of the scalar  $\phi$  and  $Re$  when the *pdf* is normalized according to the rescaled *pdf*  $\tilde{P} = \tilde{P}(\tilde{\ell})$  in (6.15). This also applies to the *pdfs* of individual wall-normal layers.

However, this is not true when *pdfs* are only normalized according to (6.10), i.e.  $P(\ell)$  is plotted. In that case, probability densities of different  $Re$  and variables differ due to the different number of generated elements in the respective layer (see figures 6.5, 6.6, 6.7, 6.8 (a)).

This behavior can be best understood by looking at the mean length profiles  $\ell_m$  and  $N$  in figures 6.13 and 6.15 for which we derived analytical relations. Both quantities depend on  $y$ ,  $Re$  and  $\phi$ . Hence, the unscaled *pdf*  $P(\ell)$ , which corresponds to the log-normal distribution, is expected to be a function of these variables, too.

To verify this assertion, in figure 6.19 we investigate the shape parameters  $\sigma$  and  $\mu$  which are plotted against the wall distance  $y/h$  for the scalar fields  $k$  and  $u$  at different  $Re$ . Note that these analytical relations again exclude the near-wall and the channel core region. Figure 6.19(a) shows that while  $\sigma$  remains basically constant for all  $Re$  and  $\phi$  throughout this range,  $\mu$  reveals a clear logarithmic dependency on  $y$ . Both results are in agreement with the findings in Aldudak & Oberlack (2012). Furthermore,  $\mu$  clearly depends on  $Re$  and  $\phi$ , i.e. decreasing for higher  $Re$ .

The parameters can be described as follows:

$$\begin{aligned} \sigma &\approx 0.563, \\ \mu_\phi(y, Re_\tau) &= \alpha_\phi(y, Re_\tau) \ln(\beta_\phi(y, Re_\tau) y/h). \end{aligned} \quad (6.29)$$

In addition to the wall-normal dependence of the coefficients of  $\mu$ , it is found that  $\alpha_\phi$  is widely insensitive to  $Re$  variation, but is influenced by the scalar field  $\phi$ .  $\beta_\phi$ , however, is coupled to both  $Re$  and  $\phi$  as given in table 6.2.

Scalar $\phi$	$k$	$u$
$\alpha_\phi$	0.402	0.369
$\beta_\phi(Re_\tau)$	$445 Re_\tau^{-1.56}$	$1973 Re_\tau^{-1.72}$

Table 6.2: Coefficients of the shape parameter  $\mu$  (6.29) for  $N$ .

Using the findings for  $\sigma$  and  $\mu$  in 6.29 with the log-normal distribution (6.28), we may finally formulate a log-normal *pdf* model for  $DE$  length which takes into account all dependencies such as the wall-normal distance  $y/h$ , the Reynolds number  $Re$  and the choice of the scalar variable in the case of  $k$  and  $u$ .

$$P(\ell, y, Re_\tau) = \frac{h}{\ell \sigma \sqrt{2\pi}} \exp\left(-\frac{1}{2\sigma^2} \ln\left(\frac{\ell}{(\beta y)^\alpha}\right)^2\right), \quad \ell > 0. \quad (6.30)$$

By inserting the respective coefficients from table 6.2, the unscaled *DE pdf* at any *Re* can now be approximated by the above equation.

With the substitute  $\ell = \tilde{\ell} \ell_m$  obtained from the invariant solution, equation 6.30 can be transformed into the self-similar, rescaled form  $\tilde{P}(\tilde{\ell})$ .

$$\tilde{P}(\tilde{\ell}, y, Re_\tau) = \frac{h}{\tilde{\ell} \ell_m \sigma \sqrt{2\pi}} \exp\left(-\frac{1}{2\sigma^2} \ln\left(\frac{\tilde{\ell} \ell_m}{(\beta y)^\alpha}\right)^2\right), \quad \tilde{\ell} > 0. \quad (6.31)$$

Note that the *Re* dependence of this log-normal *pdf* model is introduced by  $\ell_m$  (equations 6.19, 6.20) and  $\beta$  which are both functions of *y* and *Re*.

### 6.1.3 Conditional Mean of Scalar Differences

In this section, we examine the conditional mean of scalar differences between the values at the extremal points given the length of the corresponding dissipation element for the instantaneous turbulent kinetic energy *k*. Therefore, the first order conditional moment is investigated to measure its scaling along the wall-normal distance. The first moment based on gradient trajectories is non-zero since the value of the turbulent kinetic energy, by definition, increases monotonically along a trajectory from the minimum to the maximum point.

Considering this, the conditional mean of scalar difference, non-dimensionalized with  $u_\eta^2$  and  $u_\tau^2$ , i.e. the Kolmogorov and the friction velocity, respectively, is plotted for five equidistant wall-normal layers and three different Reynolds numbers. The Kolmogorov velocity scale is defined as

$$u_\eta = (\nu\epsilon)^{1/4}. \quad (6.32)$$

In figure 6.20 we focus on the center regions of the channel corresponding to  $0.2 \leq y/h \leq 1$ , where the least mean shear is present in the flow. For sufficiently large *DE*, the double logarithmic plots reveals a power law with a scaling exponent of 2/3 which is known from Kolmogorov's hypothesis (as discussed in §1.2.2). This applies to elements whose sizes are close to the mean *DE* length  $\ell_m$ , hence in the order of  $\lambda$ , and larger ( $\ell \geq \ell_m$ ). It is noteworthy that even the three intermediate layers between 0.2 and 0.8 follow the 2/3 scaling. These layers collapse perfectly as a consequence of the normalization while the central core region departs

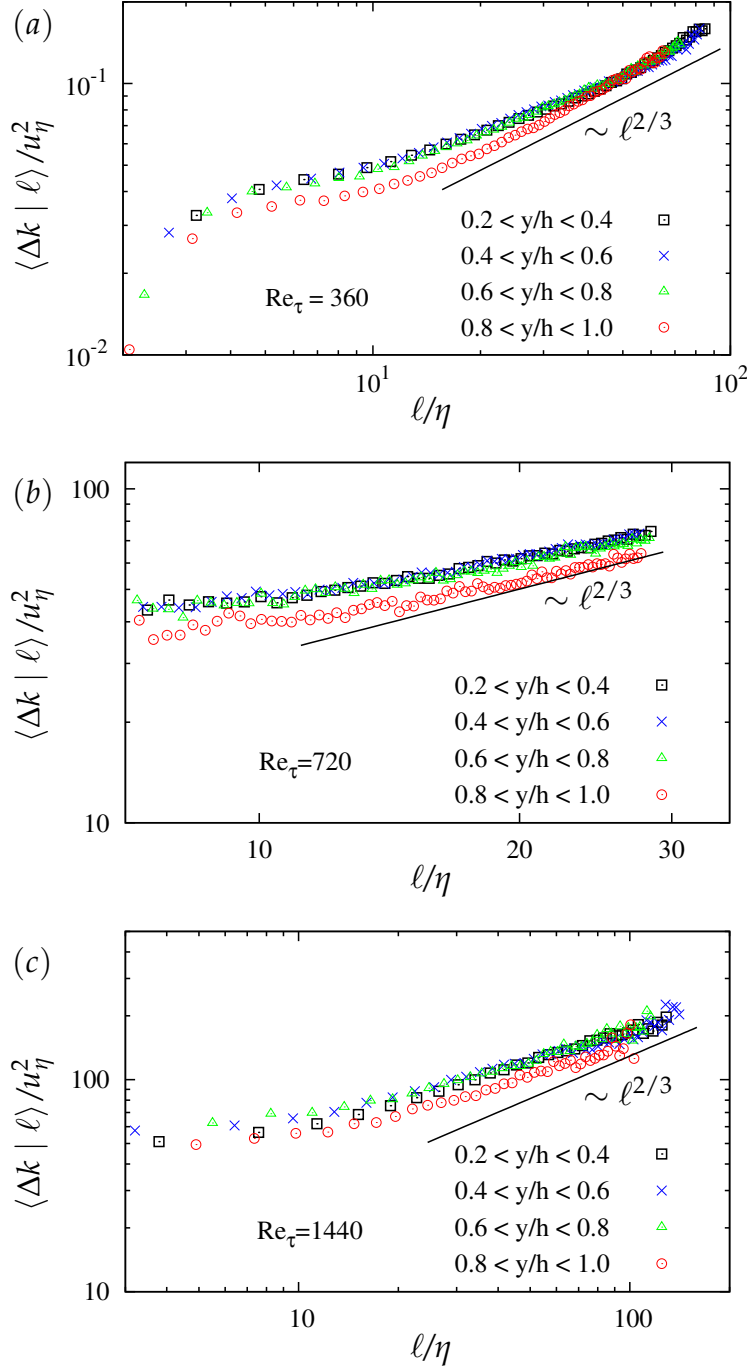


Figure 6.20: Conditional mean scalar differences for equidistant wall-normal channel layers versus  $DE$  length for different  $Re$ . Solid lines represent Kolmogorov's  $2/3$  scaling exponent.



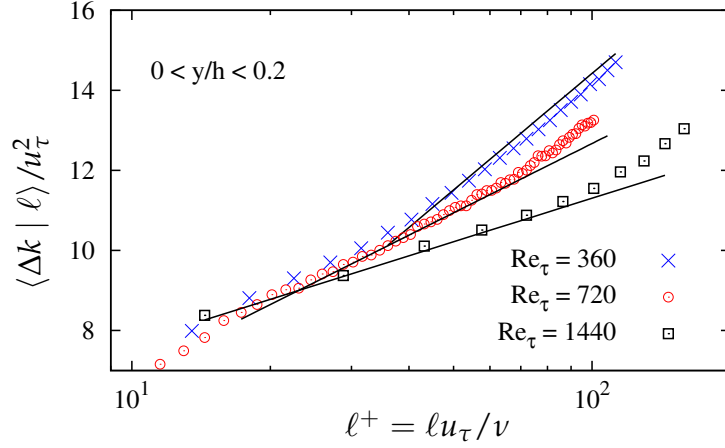


Figure 6.21: Conditional mean scalar differences for equidistant wall-normal channel layers as functions of  $DE$  length in wall-units for different  $Re$ . Solid lines are logarithmic fits.  $Re_\tau = 360$ :  $\sim \ln(0.3\ell)$ ;  $Re_\tau = 720$ :  $\sim \ln(1.6\ell)$ ;  $Re_\tau = 1440$ :  $\sim \ln(10.3\ell)$ .

somewhat from them. However, it must be noted that in the the highest  $Re$  case (figure 6.20(c)) scalar differences do not follow the scaling exponent exactly, but have a somewhat flatter slope.

Approaching the wall, this scaling is likely to break definitely under the influence of strong shear-induced anisotropy. This is confirmed by the semi-logarithmic plot 6.21. In the near-wall layer ( $0 \leq y/h \leq 0.2$ ) consisting of the buffer and logarithmic regions where turbulent kinetic energy scales as  $u_\tau^2$  we may invoke the same Lie symmetry arguments as for the mean velocity log-law (Oberlack (2001), Oberlack & Rosteck (2010)). For this, we may rewrite the invariant equation for the mean flow equation (6.5) in terms of the conditional mean scalar variance

$$\frac{d\ell}{a_1\ell} = \frac{d\langle \Delta k | \ell \rangle}{(a_1 - a_2)\langle \Delta k | \ell \rangle + a_5} \quad (6.33)$$

where  $a_1$  and  $a_2$  still refer to the scaling groups of space and time in equations (6.2) and (6.3), respectively, here combined to

$$t^* = e^{a_2 t}, \quad x^* = e^{a_1 x}, \quad \mathbf{U}^* = e^{a_1 - a_2} \mathbf{U}, \quad p^* = e^{2(a_1 - a_2)} p. \quad (6.34)$$

$a_5$ , in fact, corresponds to a statistical group similar to  $a_4$  in equation (6.5) (see Oberlack & Rosteck (2010)).

Employing the velocity scale  $u_\tau$  as the symmetry-breaking parameter for the velocity scale in (6.34), i.e.  $a_1 - a_2 = 0$ , we obtain from (6.33) the logarithmic scaling

$$\langle \Delta k | \ell \rangle = \frac{a_5}{a_1} \ln(\ell) + C . \quad (6.35)$$

Normalizing by wall coordinates yields

$$\langle \Delta k | \ell \rangle = u_\tau^2 \left( \gamma_1 \ln \left( \frac{\ell u_\tau}{\nu} \right) + \gamma_2 \right) . \quad (6.36)$$

This is rather equivalent to the classical power spectrum  $E(K) \sim u_\tau K^{-1}$  in the logarithmic region, where  $K$  is the wave number (see e.g. Perry, Henbest & Chong (1986)), which is nicely verified in figure 6.21. This logarithmic law is again valid for  $DE$  where  $\ell \geq \ell_m$ .

The joint probability density function (*jpdf*) for the parameters  $\Delta\phi$  and  $\ell$  can be written as  $P(\Delta\phi; \ell)$  which is the product of the marginal *pdf* and the conditional probability density (*cpdf*) of the scalar difference according to Bayes' theorem.

$$P(\Delta\phi; \ell) = P(\ell) P(\Delta\phi | \ell) . \quad (6.37)$$

The *jpdf* contains information that allows the reconstruction of statistics such as the conditioned probability distributions and marginal *pdfs*. Equation 6.37, i.e. *jpdf*, is plotted in figure 6.22 for the difference of the stream-wise velocity fluctuation  $u$  and the length between the ending points of the elements. Plots in (a)–(e) show the profiles in the five vertical layers. The known influence of the wall distance  $y$  on the  $DE$  length  $\ell$  is also present in the case of the scalar differences, as is to be expected based on the statistics examined in §3.

Accordingly, large values of  $\Delta\phi$  occur towards the wall due to higher turbulence intensity. The steep profile flattens gradually approaching the core consisting of larger elements with smaller scalar difference compared to lower layers. In addition, the profile for the entire channel is shown in picture (f) as a superposition of the five sections whose shape is more symmetrical.

The conditional probability function  $P(\Delta\phi | \ell)$  can be obtained as the ratio between joint and marginal *pdfs*, which can be interpreted as an analogous

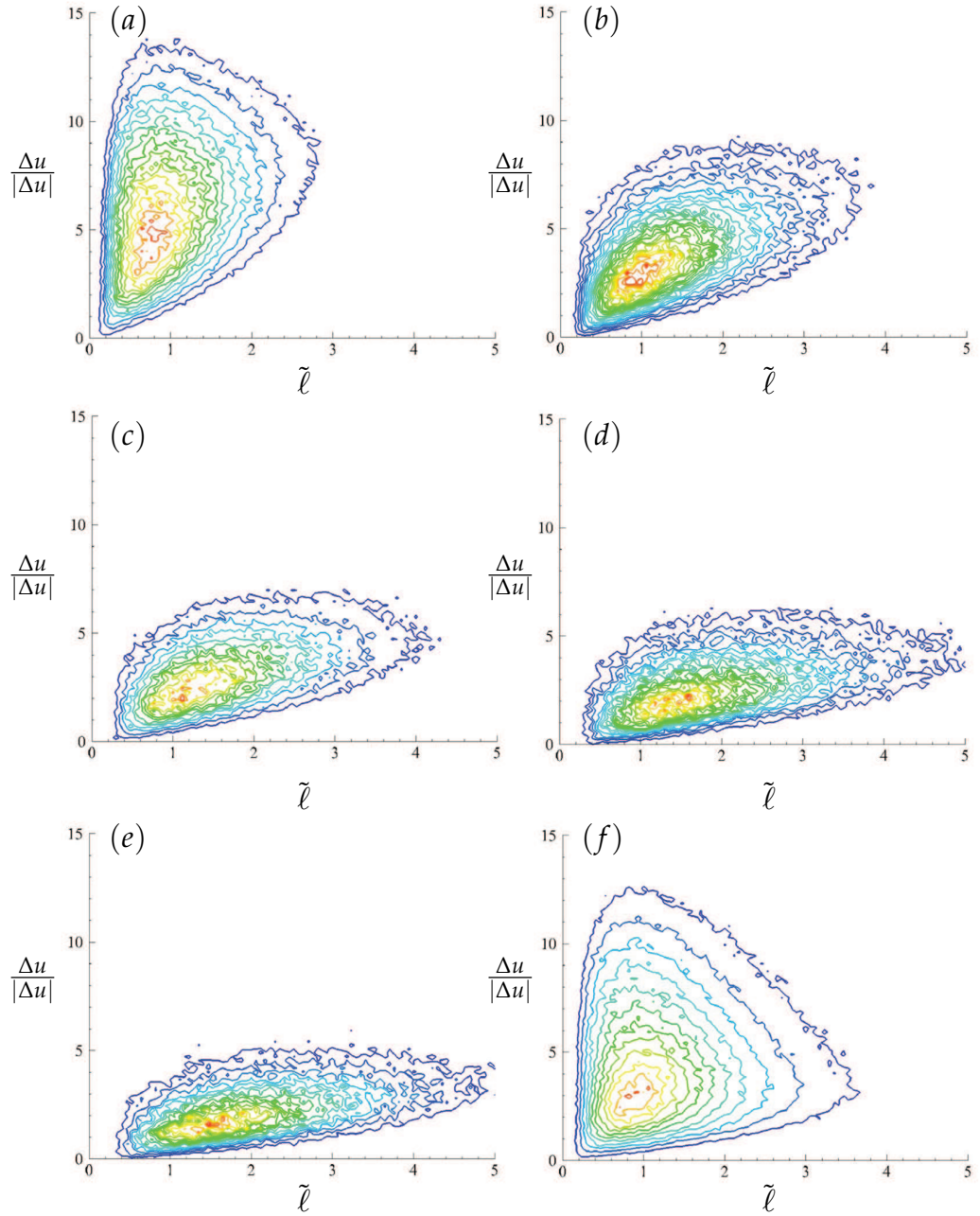


Figure 6.22: Joint *pdf* of the streamwise velocity difference and the *DE* length at  $Re_\tau = 720$ . Pictures (a) – (e) show five equidistant wall-normal layers beginning at the wall, (f) represents the whole channel.

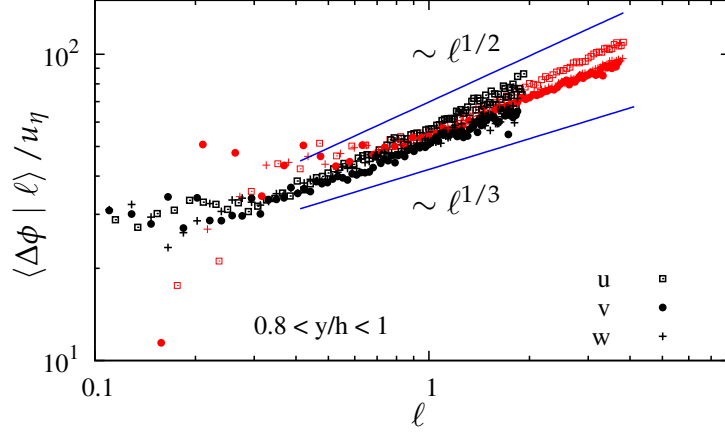


Figure 6.23: Conditional scalar differences of velocity components at the center of the channel for  $Re = 1440$  (black symbols) and  $Re = 720$  (red symbols).

moment to the structure function definition from equation 1.14 (discussed in §1.2.2). *Cpdf*, however, is conditioned on the length of the *DEs*, thus, accounts for the scalar difference on the ending points of the elements rather than arbitrary points. The distance corresponds to the linear length of the *DEs*. Moreover, unlike in classical structure functions, the scalar difference  $(\Delta\phi)_{\max-\min}$  is positive because the gradient trajectories between the ending points vary monotonously.

Although, Kolmogorov's  $n/3$ -scaling law for the inertial range is met for the kinetic energy field  $k$  (figure 6.20), scalar differences for the velocity components reveal no clear agreement in this regard. Instead of the expected scaling  $\langle \Delta\mathbf{U} | \ell \rangle \sim r^{1/3}$ , figure 6.23 shows a scaling exponent  $\approx 0.5$  for the streamwise velocity and  $\approx 0.4$  for the transversal velocities  $v, w$ . This deviation is linked to the lack of sufficient degree of isotropy for which Kolmogorov's approach is valid. In conclusion, it can be stated that for  $k$  being a scalar rather than a vector component may be the reason why scalar differences of  $k$  show better agreement than that of the velocity components.

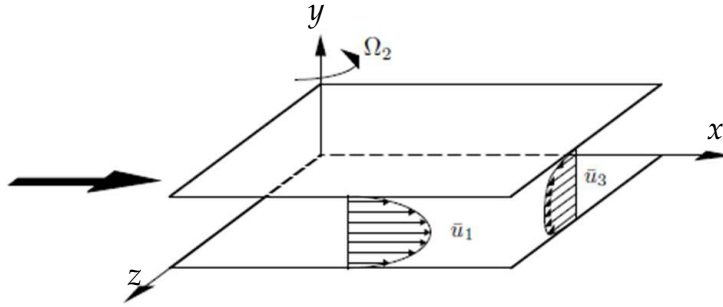


Figure 6.24: Sketch of the channel flow geometry with wall-normal rotation.

## 6.2 Turbulent Channel Flow with Wall-normal Rotation

In this chapter the dissipation element analysis will be applied to the plane turbulent channel flow with rotation around the wall-normal direction  $y$  as illustrated in 6.24. A detailed description of this flow type can be found in Mehdizadeh (2010) and, hence, is omitted here. Instead,  $DE$  statistics will be discussed.

Two calculations are performed at Reynolds number  $Re_\tau = 360$  with rotation rates  $Ro_y = 0.011$  and  $Ro_y = 0.072$ , with  $Ro_y$  being the rotation number with respect to the vertical direction  $y$ . The dimensionless rotation number  $Ro$  is defined as

$$Ro_j = \frac{2\Omega_j h}{u_\tau}, \quad \text{with } j = x, y, z, \quad (6.38)$$

where  $\Omega_j$ ,  $h$  and  $u_\tau$  are the dimensional rotation number, the channel half-height and the friction velocity, respectively. Three-dimensional DNS files from Mehdizadeh (2010) were advanced in time to obtain statistics.

It is shown in Mehdizadeh (2010) and Mehdizadeh & Oberlack (2010) that wall-normal rotation strongly affects the flow. Due to the Coriolis force, a non-zero mean spanwise velocity  $W$  along the channel height is induced. Increasing the rotation rate  $Ro_y$  leads to a drop of the mean streamwise velocity  $U$  and the wall-normal velocity  $v$ , but causes an initial increase of the spanwise velocity  $w$ , before it too decreases. Furthermore, it is stated that the turbulence intensity is reduced with an increasing rotation rate gradually forcing the flow into a completely laminar state. The authors report

that the fluid flow becomes fully laminar for rotation rates  $Ro_y \geq 0.546$ . Both cases investigated here are reportedly fully turbulent with symmetrical velocity profiles.

First, we examine the distribution of the mean *DE* length along the wall-normal direction. In figure 6.25, three flow fields at  $Re_\tau = 360$  with different degrees of rotation rate are compared for  $u$ ,  $v$  and  $w$ , hereafter referred to as case 1 – 3 according to the rotation rate. The non-rotating case analyzed in §6.1 is used as reference. It is striking that the lower rotation case possesses smaller elements for all scalar variables near the wall. Towards the core region its mean length approaches that of the non-rotational case (case 1) where they are more or less completely equal. Case 3 with the highest rotation degree has more common with the non-rotating case near the wall but deviates significantly above the buffer layer. Here, elements in case 3 are considerably larger.

This is consistent with the mentioned finding that the turbulence intensity is damped with increasing  $Ro$  since higher turbulence intensity results in more extremal points, i.e. dissipation elements, which in turn are smaller in size as already discussed.

An even greater influence of the rotation is observed in the case of the spanwise velocity field  $w$  (picture (c)). While for  $u$  and  $v$  the profiles associated with various  $Ro$  are similar in all cases, profile of case 3 for the velocity field  $w$  features a significant anomaly especially beyond the buffer layer. It can be deduced that, because of the weak turbulence intensity, moving away from the wall the number of generated elements declines very steeply. Hence, elements grow to almost 30% of the full channel height in the core of the channel.

In contrast to the behavior exhibited by the other two components, near the wall both rotation cases reveal similar element sizes for  $w$ . Again, in the outer flow region, the intermediate rotation case (2) is indistinguishable from the non-rotating case for all variables which is also evident from the number  $N$  of *DEs* in figure 6.26.

The anomalous behavior of the spanwise velocity field can also be observed regarding  $N$  as depicted in figure 6.26(b). Much less *DEs* are produced here for the high  $Ro$  case, especially near the wall. Contrarily, these differences in  $u$  field are weaker. Note that the number  $N$  is rescaled with the channel volume.

Interestingly, at  $Ro = 0.072$  both, number and mean length of the *DEs* in  $w$  field, seem to be less than that of the reference case in the near-wall

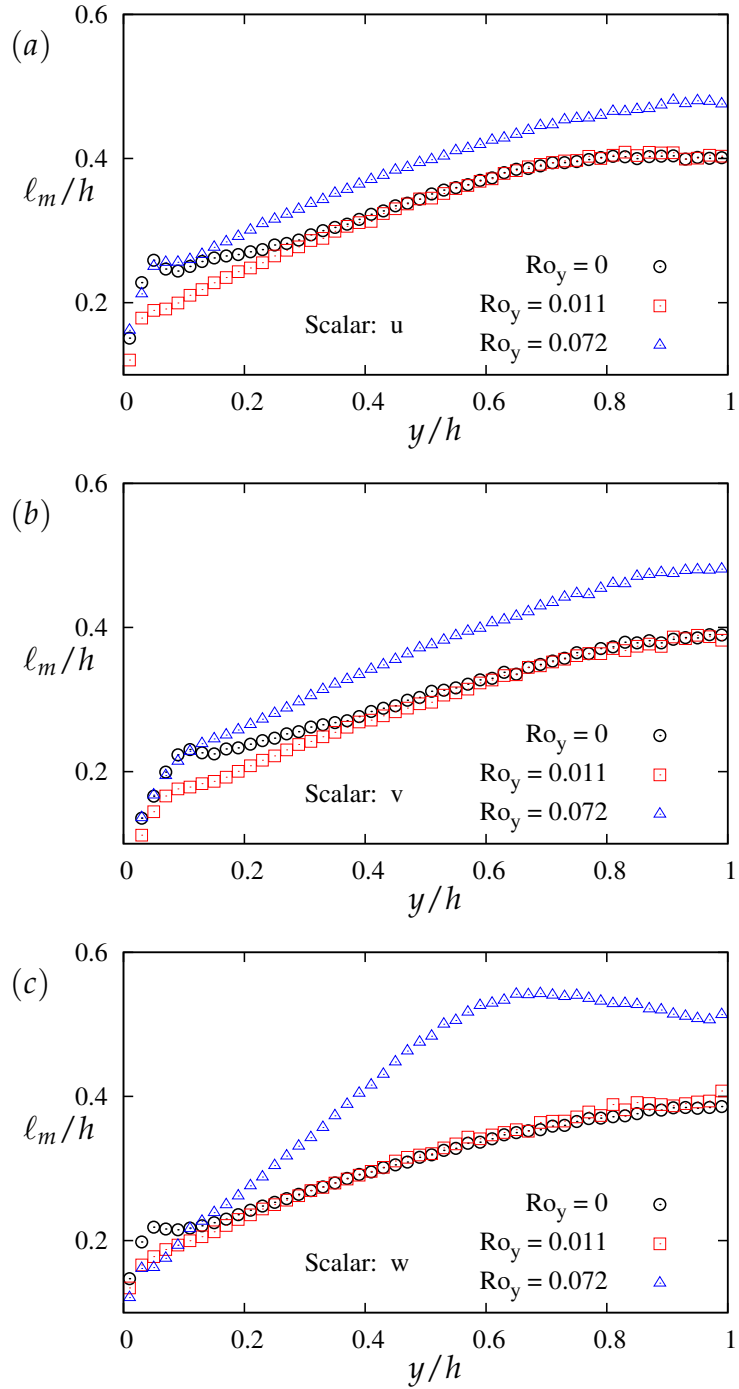


Figure 6.25: Mean *DE* length  $\ell_m$  at different rotation rates.

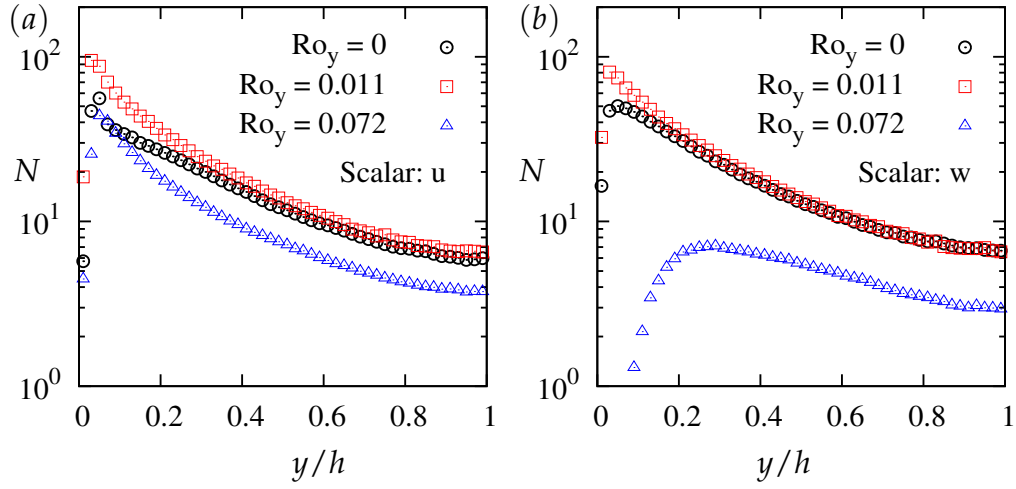


Figure 6.26: Number  $N$  of  $DE$  per unit cube ( $l^3$ ) along the wall-normal direction for  $u$  and  $w$ .

region,  $0 \leq y/h \leq 0.1$ , which actually contradicts previous observations, namely that they are inversely proportional. The reason for this may lie in the effect of laminarisation. Indeed, in Mehdizadeh & Oberlack (2010) the cases above this rotation rate are classified as quasi-laminar. Thus, it is possible that laminarisation effects make itself felt already in this rate of rotation.

Further, in figures 6.27, 6.28, 6.29,  $DE$   $pdfs$  are presented for five equidistant wall-normal layers between the wall and the centerline of the channel as before. For comparison, the non-rotating case is displayed with solid lines in each plot. The self-similar behavior, which was observed for the plane Poiseuille flow, apparently applies to the wall-normal rotation case for the rescaled  $pdf$   $\tilde{P}$ . Except for the first layer close to the wall,  $pdfs$  for case 1 and case 2 show similar shapes. This is rather missing in comparison with case 3 particularly for the spanwise velocity field. The profiles of case 3 in the center of the channel are more flat and very different from the reference case.

In conclusion, it can be stated that the generation and distribution of turbulent structures are strongly affected by the wall-normal rotation due to the induced non-zero spanwise velocity and probably laminarisation effects towards relatively high rotation numbers.



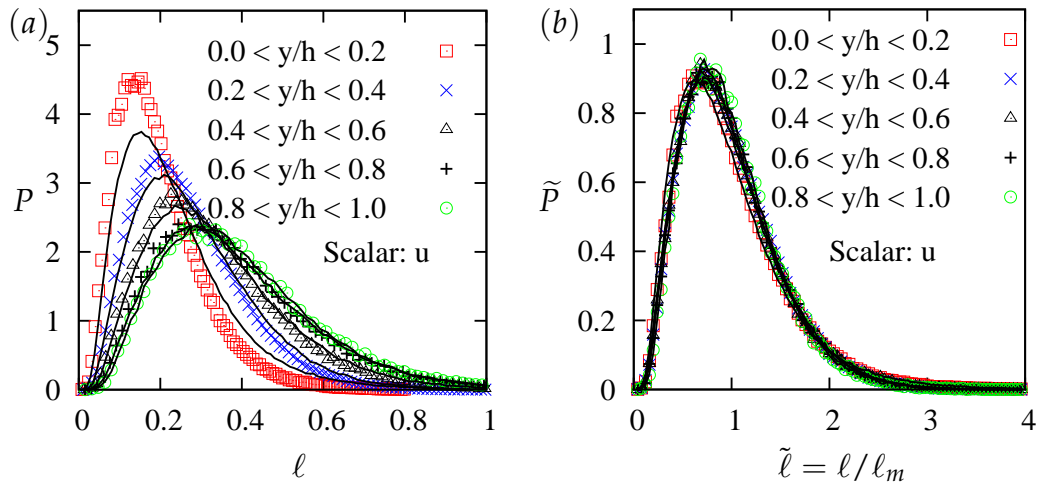


Figure 6.27: Pdf in equidistant layers for scalar  $u$  and  $Re_\tau = 360$ . Rotation rate is  $Ro_y = 0.011$ . Solid lines represent the case without rotation.

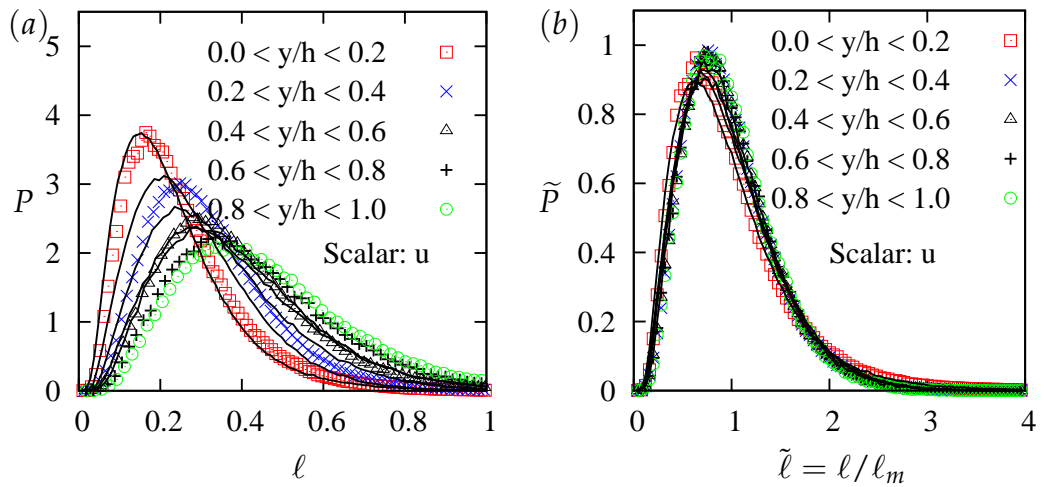


Figure 6.28: Same as in 6.27, but for the rotation rate  $Ro_y = 0.072$ .

### 6.3 Turbulent Channel Flow with Streamwise Rotation

Subsequently, turbulent channel flow rotating about the streamwise direction is investigated by means of dissipation element analysis. Similar to the wall-normal rotating case, a cross-flow in the spanwise  $z$  direction is

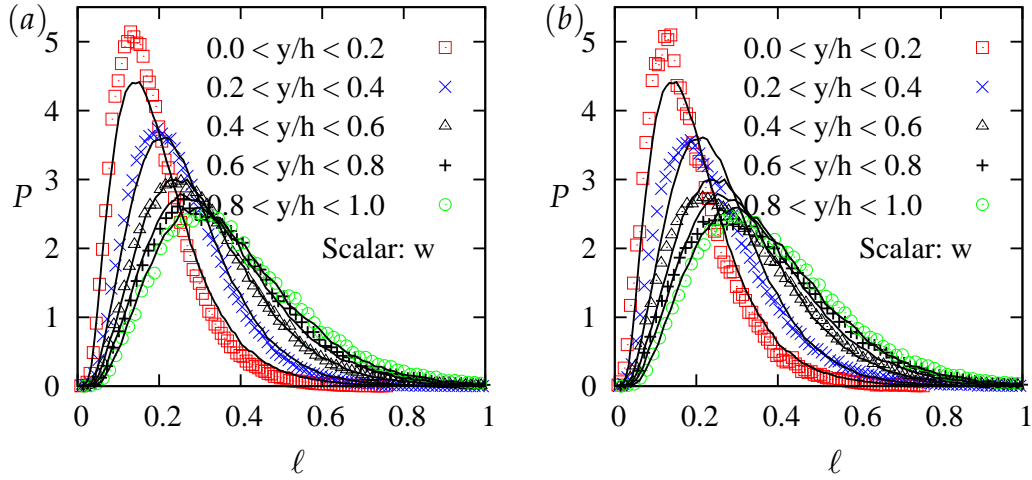


Figure 6.29: Pdf in equidistant layers for scalar  $w$ . (a)  $Ro_y = 0.011$ , (b)  $Ro_y = 0.072$ . Solid lines represent the case without rotation.

induced by the Coriolis force (figure 6.30). This flow type has been extensively addressed, e.g. by Oberlack, Cabot, Pettersson Reif & Weller (2006), Weller & Oberlack (2006) and Weller (2007).

Oberlack (2001) has shown that, in analogy to the classical non-rotating channel, self-similar mean velocity profiles can be found as following,

$$\bar{U} = C_1 \Omega_1 y + C_2, \quad (6.39)$$

$$\bar{W} = C_3 \Omega_1 y + C_4. \quad (6.40)$$

DNS data showed that the spanwise velocity profile is 'S'-shaped with a triple zero-crossing. Hence, the cross-flow appears to change the direction which is skew-symmetric about the centerline (see Weller & Oberlack (2006)).

We consider the streamwise rotating case at  $Re_\tau = 215$  with the rotation rate  $Ro_x = 10$ . The latter parameter is defined according equation 6.38.

Mean element length  $\ell_m$  is plotted in figure 6.31(a) for the three components of the velocity along the wall-normal direction. Their behavior at the origin is very different from the classical channel flow case as they rise much slower and uniformly up to  $y/h = 0.2$ . However, the profiles differ significantly hereafter. The transversal components change dramatically

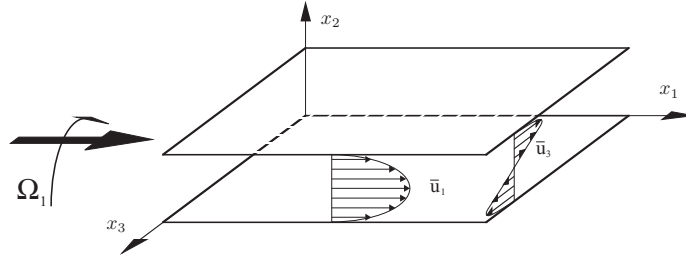


Figure 6.30: Sketch of the channel flow geometry with rotation about the streamwise direction.

at around  $y/h \approx 0.61$ , i.e. a strong increase takes place. It is interesting to note that this point corresponds to the wall-normal point where the spanwise velocity  $W^+(y/h)$  reaches a maximum between two zero-crossing points as shown in figure 6.34(a). This observation is further augmented by the results for the kinetic energy field. A sudden jump occurs at  $y/h \approx 0.46$  where the profile  $k^+(y/h)$  exhibits a saddle point (see figure 6.34(b)). Note that these statistics are plotted across the whole channel height  $2h$ . The mentioned 'S'-shaped spanwise velocity profile is confirmed. The saddle point in the  $k^+$ -profile is not reported for the classical non-rotating case. Hence, it can be concluded that it is due to the streamwise rotation effects. These results confirm the highly complex character of this flow type.

To recall the characteristic profile of the non-rotating case,  $\ell_m$  for the  $Re_\tau = 360$  case and the  $k$ -field is included. As such, it differs considerably from the rotating case having a persistent linear scaling range.

In figure 6.33, numbers of produced elements for different scalar variables are illustrated. The analytical approximation 6.26 for the non-rotating case and the scalar  $w$ , which was derived earlier, is plotted for  $Re_\tau = 215$  as comparison. Near the wall,  $N$  seems to be comparable in both cases while approaching the channel there are more  $DEs$  in the rotating case. Further, in the core region there exist fewer elements for the  $u$ -velocity, which are larger, than those of the other scalar variables. It can be concluded that, compared with the non-rotating flow, more  $DEs$  are created leading to smaller elements.

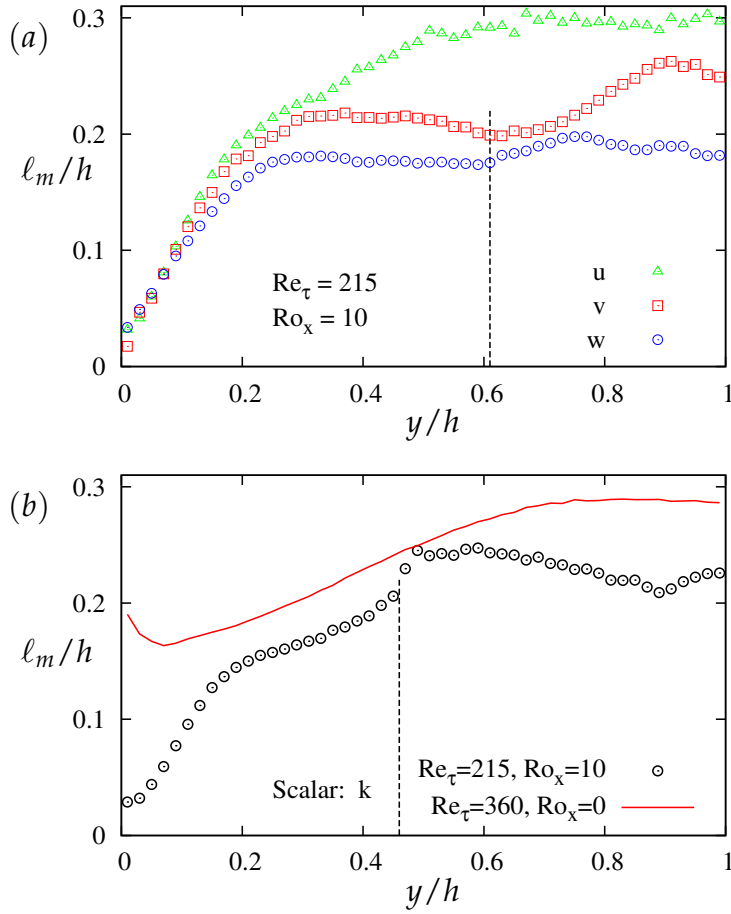


Figure 6.31: Mean *DE* length  $\ell_m$  for (a) velocity components and (b) kinetic energy as functions of the wall-normal direction. Vertical lines denote extremal points of  $W(y)$  and  $k(y)$  in (a) and (b), respectively (see figure 6.32).

Furthermore, it can be seen that  $N$ , as well, is affected by the extremal points mentioned above (see figure 6.32) causing remarkable changes of the curve characteristics.

The probability distributions of the *DE* length are seen to become very irregular under the impact of streamwise rotation as apparent from figures 6.34 and 6.35. The first layer is very narrow for all variables containing mainly small elements. All remaining far-wall layers, however, appear to have rather similar shapes than a gradually widening profile as known from the non-rotating case. The curves collapse especially for the two

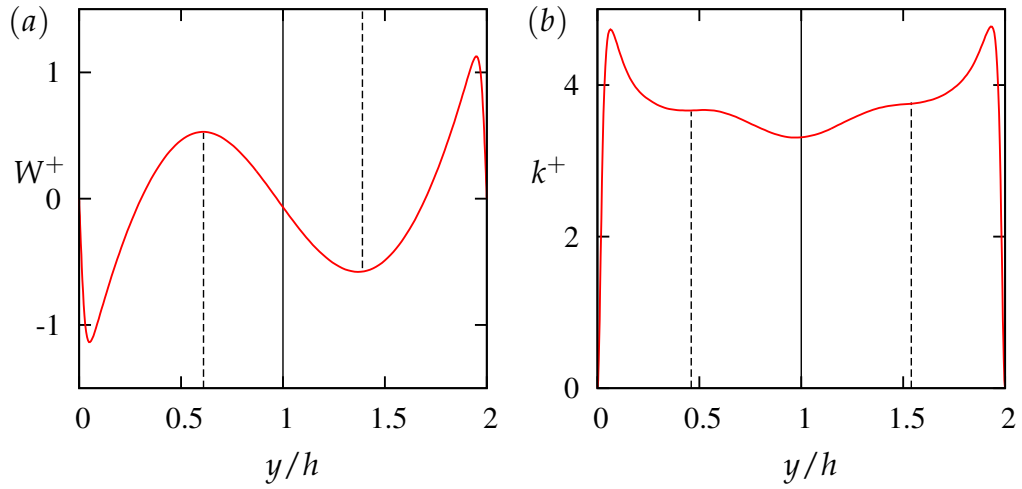


Figure 6.32: Spanwise velocity and kinetic energy in wall units as functions of the wall distance. Dashed lines mark the extremal points relevant to the changes in  $DE$  length profiles in figure 6.31.

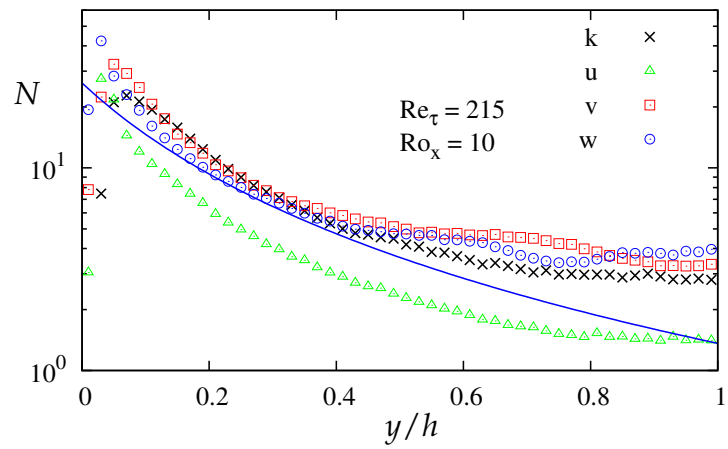


Figure 6.33: Number of  $DEs$  for various scalar fields. Blue line shows the analytical approximation for the non-rotating case as comparison.

transversal velocity components (see figure 6.35) which usually has been observed only for the rescaled  $pdf \tilde{P}(\tilde{\ell})$ . This can be explained by looking at the mean length distributions in figure 6.31. For  $P(\ell)$  to vary gradually with  $y/h$ ,  $\ell_m(y)$  needs to possess a clear non-constant scaling behavior as

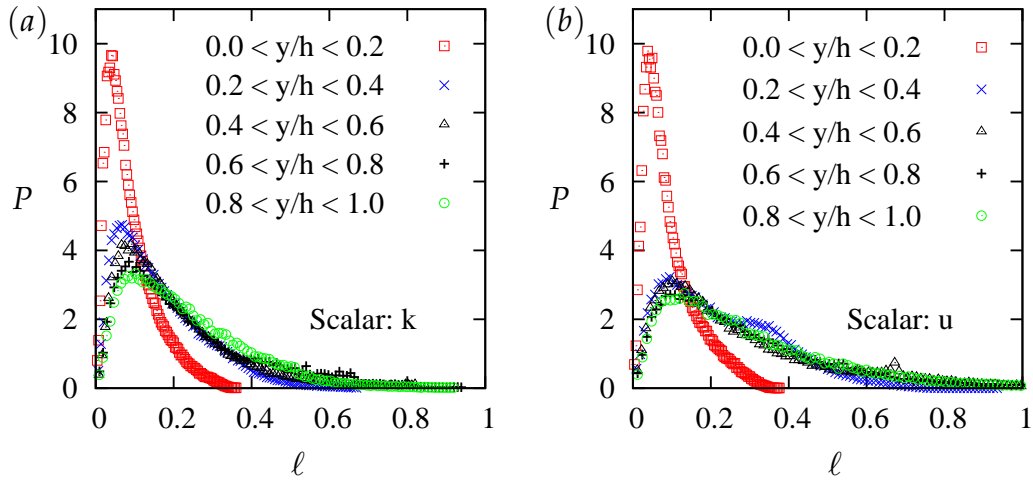


Figure 6.34: Pdf in equidistant layers for  $Re_\tau = 215$  and rotation rate  $Ro_x = 10$ .

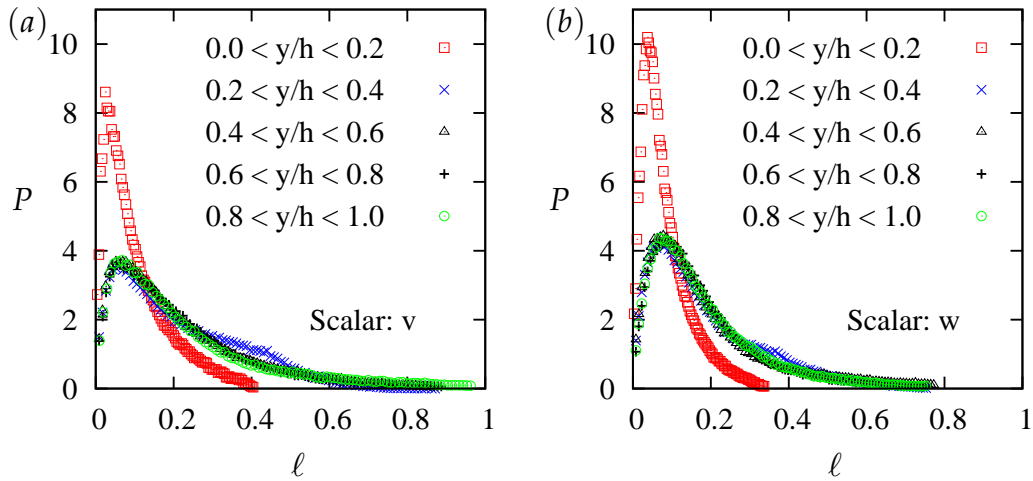


Figure 6.35: Same as in 6.34, but for  $v$  and  $w$ .

is the case for the classical channel flow. Though, this is not the case here. In fact, the mean lengths of  $v$  and  $w$ , in particular, fluctuate around a certain value which, at the end of the day, causes the observed collapse of the pdf profiles. Consequently, in the absence of a clear scaling between  $DE$  length and  $y$ , the self-similar attribute of the pdf  $\tilde{P}$  is noticeably impaired (not shown here).

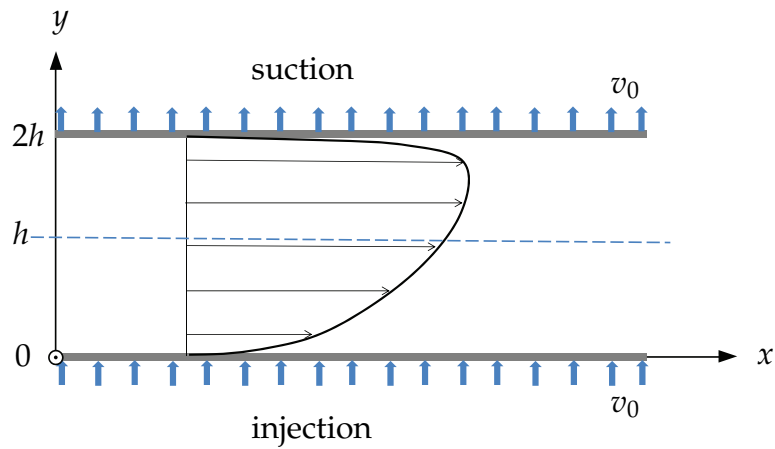


Figure 6.36: Sketch of the channel flow geometry with wall transpiration.

## 6.4 Turbulent Channel Flow with Wall Transpiration

As the final flow type, turbulent Poiseuille flow with wall transpiration is analyzed with the help of *DE* method. Figure 6.36 provides a schematic view of the mentioned flow. Unlike the classical channel configuration, the no-slip boundary condition at the walls is imposed only on the horizontal velocity components. A constant mean vertical velocity is introduced allowing a mass transfer normal to the porous wall boundaries (for more details see e.g. Vigdorovich & Oberlack (2008), Avsarkisov et al. (2011)). Here, the plane turbulent channel flow field at  $Re_\tau = 720$  has been used as initial restart file. The transpiration number  $v_0/u_\tau = 0.027$  was imposed.

Based on the velocity profile in figure 6.37(a), three different regions can be distinguished, namely the injection wall, the core and the suction wall regions. The shape of the velocity profile is asymmetric due to the changed boundary conditions where the velocity is damped at the injection side with higher degree of turbulence and grows towards the suction wall. The above authors show that a logarithmic mean flow scaling prevails in the outer flow region.

In figure 6.37(b), turbulence intensity statistics are seen to be asymmetrical as well. The injection side is obviously more turbulent than the suction side of the flow. These conclusions are important for the interpretation of the *DE* statistics because the generation of the latter is directly linked to turbulence activity. Hence, it is to be expected that at the injection side of

the flow more elements are produced which are smaller than those located at towards the suction side.

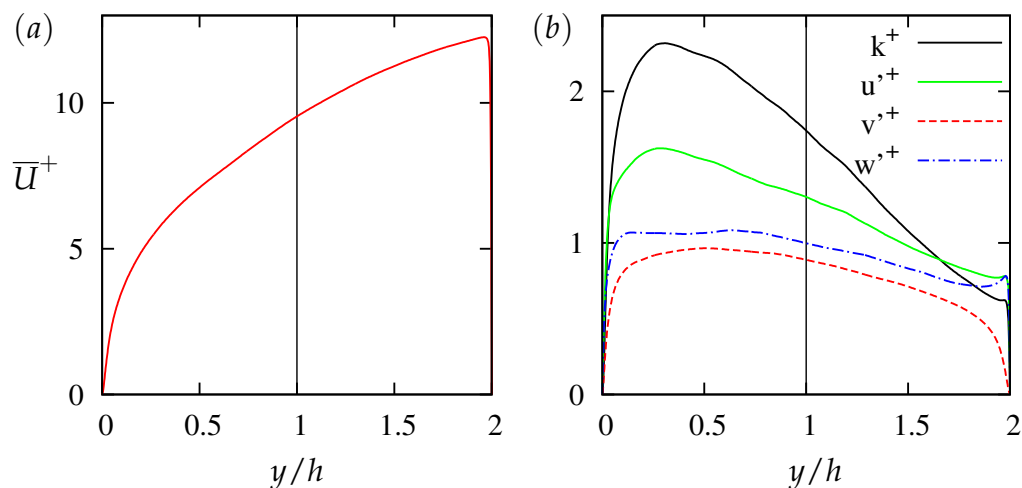


Figure 6.37: (a) Mean velocity and (b) turbulence intensities in wall units for turbulent channel flow with wall transpiration.

Indeed, figures 6.38 and 6.39 confirm these findings. The clear asymmetry of the flow is reflected in unbalanced profiles of  $DE$  length and number, respectively, across the channel height. As already assumed, the number of  $DEs$  decreases steadily approaching the suction wall side. In fact, one can notice a nearly perfect exponential decay. In the vicinity of the suction wall ( $y/h = 2$ ), where fluid is exhausted, there is a distinct jump in the number of elements. In general, the profiles of all scalar variables appear to be very similar in shape. The same applies to the mean length characteristics which are relatively ordered and nearly linear for the most part of the channel height. Due to the higher degree of turbulence, elements near the injection side are considerably smaller.

It is interesting to note that these findings support the logarithmic nature of the mean velocity profile in the same region postulated by the above authors.

In the light of the conclusions obtained in previous flow cases, a clear scaling behavior of the  $DE$  length is supposed to cause a collapse of the rescaled  $pdf$   $\tilde{P}(\tilde{\ell})$ . Accordingly, one would expect the latter to be self-similar throughout the whole channel height except for the two near-wall layers, of course.



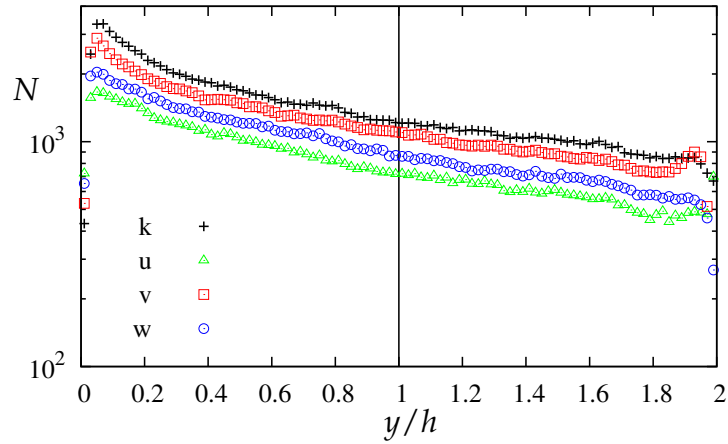


Figure 6.38: Number of *DEs* for various scalar fields. Note that the whole channel height is displayed.

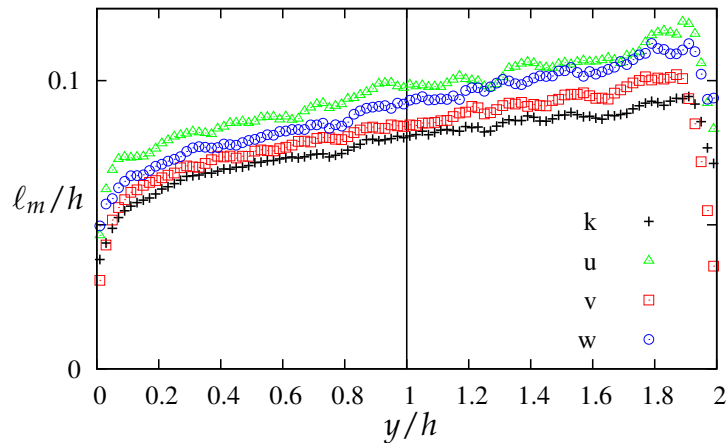


Figure 6.39: Mean *DE* length for various scalar fields.

According to figures 6.40 and 6.41, this assumption is indeed met. Note that in (a) the non-scaled *pdf* is shown whereas (b) shows  $\tilde{P}$  for ten equidistant layers from 0 to  $2h$ . For reasons of clarity, the labels are distributed between the two plots (a) and (b) where the lines show the suction side ( $> h$ ) and symbols show the injection side ( $< h$ ). Symbols and lines of the same color illustrate the corresponding mirrored wall-normal layers.

The *pdfs* of the linear scaling region agree with each other very well for all scalar variables considered here. This is interesting particularly because, due to the asymmetry, the analyzed range is double as long as in the clas-

sical case. Non-normalized *pdfs* for the velocity components  $v$  and  $w$  are depicted in figure 6.42 for the sake of the completeness. The gradually decreasing and widening profiles in the direction of the suction wall are in line with the above assertions indicating less/larger elements towards the suction wall.

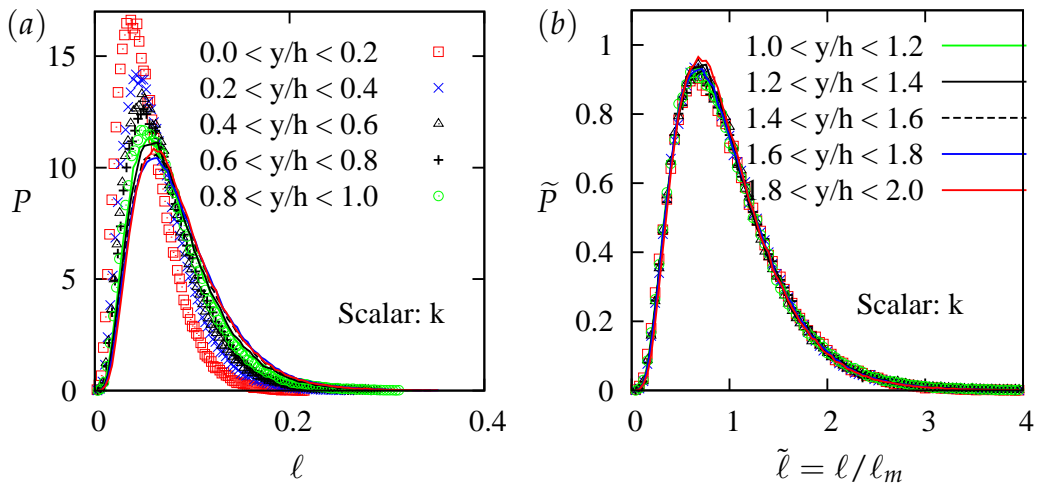


Figure 6.40: Pdfs of  $k$  where  $l$  is not-normalized in (a) and normalized with  $\ell_m$  in (b). Wall-normal layers of the injection and suction side are represented by symbols and lines, respectively.

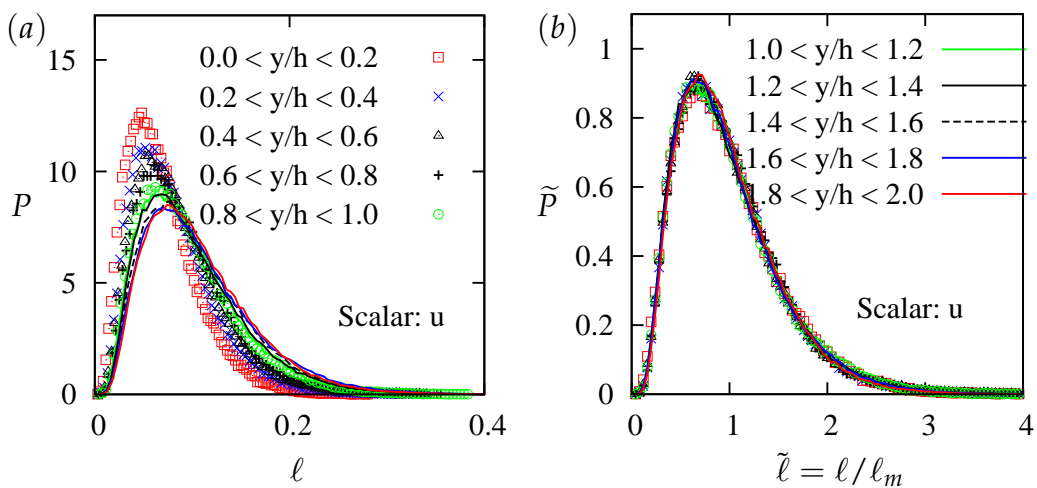


Figure 6.41: Same as in 6.40, but for scalar  $u$ .

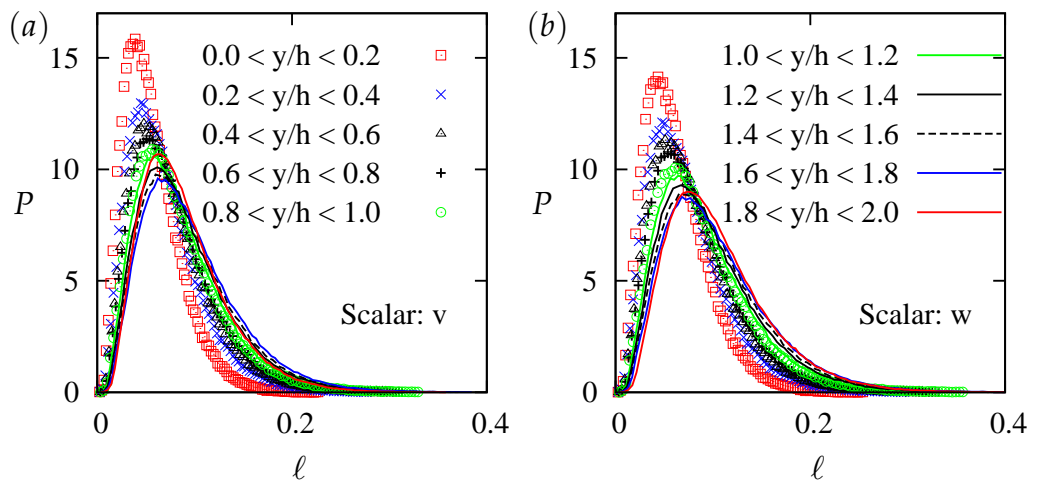


Figure 6.42: Pdfs  $P$  of the wall-normal and spanwise velocities.

## 7 Streamline Segments

The intention behind the Dissipation Element approach was to describe the flow field in terms of non-arbitrary sub-units whose definitions raise from the flow physics. With this in mind, other flow properties such as the streamlines may be suitable as well. Unlike *DEs*, streamlines (*SLs*) are associated with the velocity vector field where every fluid particle is subject to a distinct velocity magnitude and direction. In a three-dimensional instantaneous velocity field, *SLs* are everywhere tangent to the velocity vector defining the direction of the flow particles. Consequently, they do not intersect each other since, otherwise, fluid at intersection points would be multi-valued.

Following the direction of the local velocity vector at a given point in the flow field the respective streamline can be identified. In general, streamlines do not end within a flow in motion but extend along the flow domain. To obtain meaningful geometrical topologies from streamlines, one needs a natural definition of their bounding points similar to the *DE* approach. Wang (2010) proposed the idea of streamline segments defined as streamline fractions between two adjacent extremal points of the absolute velocity  $U_m$  at the curvilinear  $s$  along the streamline. Thus, extremal points with  $\partial U_m / \partial s$  connect two adjacent *SL* segments. Unlike dissipation elements, streamlines do not depend on the choice of the scalar but are related to the velocity field. Furthermore, while gradient trajectories in turbulent flows are of finite length, *SLs* theoretically can be infinitely long.

### 7.1 Numerical Algorithm

Extremal points of a segment, hence its ending points, are usually not located at the numerical grid points exactly but are rather located within a hexahedron (or cell) consisting of eight grid points at the corners. Thus, an appropriate method is needed to determine the appointed position of the sought point. To address this issue, we adopted a local tricubic interpolation scheme in three-dimensions to trace streamlines along the direction of the velocity vector. The advantage compared with trilinear interpolation

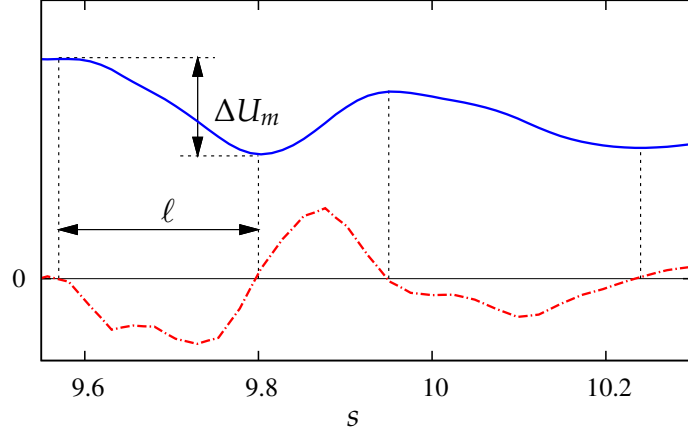


Figure 7.1: Absolute velocity  $U_m$  (solid line) and its derivative  $\partial U_m / \partial s$  (dot-dashed line) along a streamline. Dashed black lines show the bounding points of streamline segments.

is the improved accuracy while, at the same time, the method is computationally more expensive. Different to other tricubic interpolations which combine three separate one-dimensional interpolations, the interpolation method employed here is an integrated method first proposed by Lekien & Marsden (2005).

Given that the values and the respective first and second derivatives at the corners of the cell are known, a piecewise polynomial function  $f$  to be interpolated inside the cell can be constructed as follows,

$$f(x, y, z) = \sum_{i,j,k=0}^N a_{ijk} x_i y_j z_k , \quad (7.1)$$

where  $a_{ijk}$  are coefficients of the tricubic interpolant for the current cell. A specific  $64 \times 64$  matrix (see Lekien & Marsden (2005)) provides the relationship between these coefficients and the derivatives at the corners of the cell. This method is implemented into a FORTRAN 90 post-processing code which integrates the streamline path using a Runge-Kutta 4<sup>th</sup> order method.

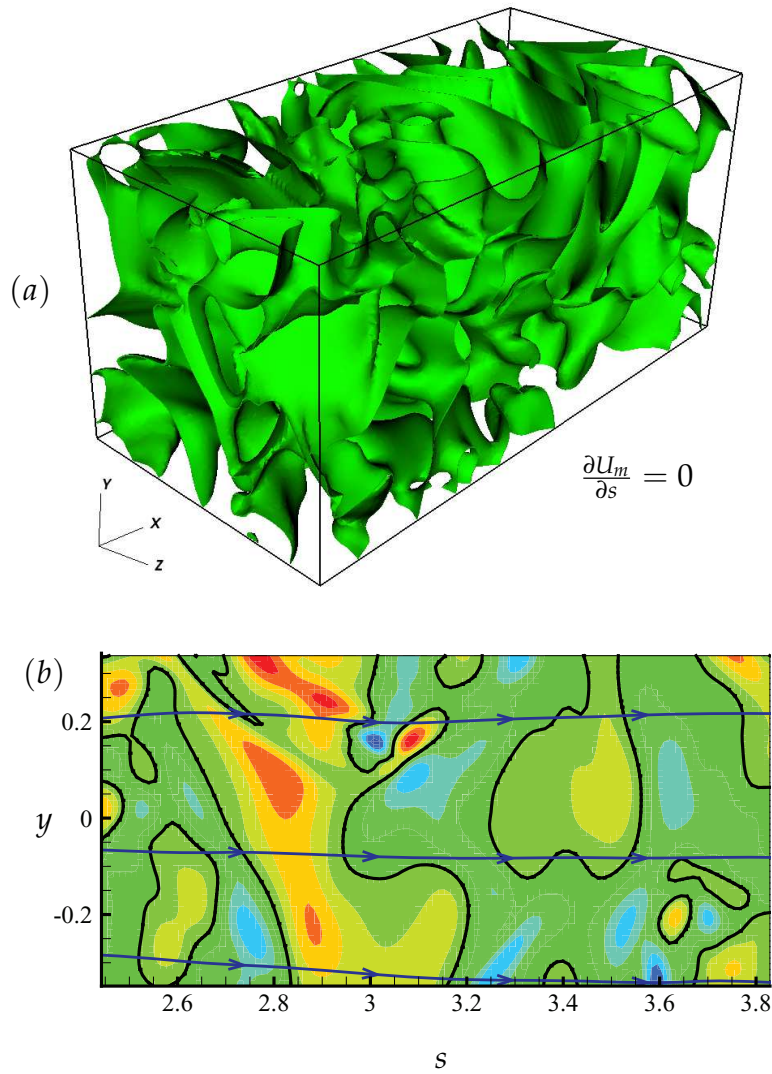


Figure 7.2: (a) Three-dimensional zero-gradient iso-surfaces of the velocity magnitude. (b) zero-gradient iso-lines (black) separating high and low gradient areas (colored red and blue) with streamlines (dark blue lines) in two-dimensions.

## 7.2 Streamline Segment Statistics

Figure 7.1 illustrates three segments with the statistical parameters  $\Delta U_m$  and the arc-length between the extremal points as examples. Solid line shows the profile of the velocity magnitude alongside with its derivative  $\partial U_m / \partial s$  whose zero-crossing points represent the transition between two *SL* segments as indicated by the dashed vertical lines. They can be further divided into positive and negative segments according to whether the sign of the derivative  $\partial U_m / \partial s$  is positive or negative.

In three-dimensional flows,  $\partial U_m / \partial s = 0$  forms iso-surfaces, as shown in figure 7.2(a), which separate the segments of the *SLs* penetrating them. Picture (b) displays a two-dimensional snapshot of the interaction between streamlines and, in this case, iso-lines of  $\partial U_m / \partial s = 0$ . Every intersection point marks the beginning point of a new segment which is, at the same time, the ending point of the preceding segment.

In the following, streamline segment analysis will be conducted in the case of turbulent channel flow for various  $Re$ . As in the *DE* analysis, effects of the Reynolds number and wall-distance variation will be examined. First, we will verify the existence of a characteristic scaling region of the mean segment length  $\ell_m$  with respect to the wall-normal direction  $y$ . It is worth remembering at this point that *DEs* reveal a self-similar behavior within wall-normal layers where *DE* length scales linearly with  $y$ .

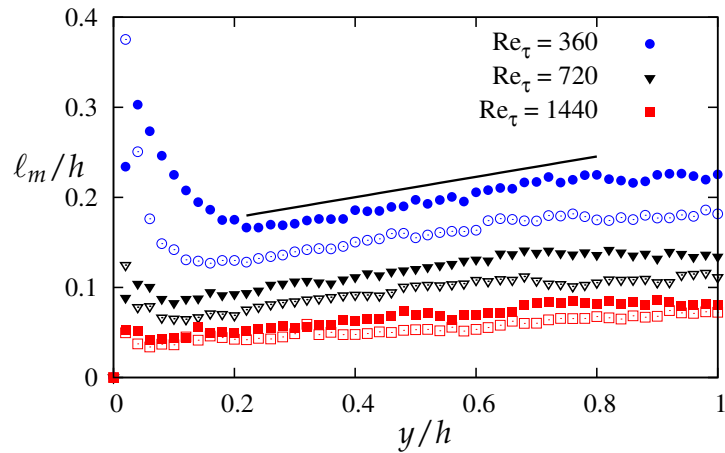


Figure 7.3: Mean length  $\ell_m$  of streamline segments along the wall-normal direction  $y$  for different  $Re$ . Filled symbols: positive segments, open symbols: negative segments.

Indeed, a similar result is found from figure 7.3 for the *SL* segments. For all  $Re$  considered here, the length of the segments seems to vary linearly with the distance from the wall, practically, in the same region as dissipation elements. Considering the similar shapes of the *DE*, *SL* segment and Kolmogorov length scales (see §5), a linear scaling range located between the near-wall and centerline regions of the channel can be considered as universal in the turbulent channel flow. Near the wall, around the buffer layer, the well-known maximum peak is observed which is more pronounced compared to the *DE* length distribution. Moreover, the flattening close to the centerline of the channel with relatively weak shear effects is also typical.

One interesting feature with regard to *SL* segments is that positive segments ( $\partial U_m / \partial s > 0$ ) are always larger than the negative ones. Only very close to the wall, the opposite is true, i.e. negative segments are larger. However, the difference between them apparently decreases as  $Re$  increases. *SL* segments are in average shorter at higher  $Re$ .

Next, marginal *pdfs* of *SL* segments are discussed separately for positive and negative segments, hereafter denoted as  $P_+$  and  $P_-$ . In figures 7.4 and 7.5, overall *pdfs* are plotted for different Reynolds numbers. The shape of the *pdfs* is similar to the log-normal distribution of the *DE pdf* to a large extent. However, revealing a very steep rise at the origin, their maxima occurs at smaller length scales, i.e. at around  $\approx 0.25\ell_m$  which is  $\approx 0.6\ell_m$  for *DEs*. In the far-tails *pdfs* decay exponentially as highlighted in semi-logarithmic subplots.

As indicated by the linear scaling character of the mean length, the rescaled *pdfs*  $\tilde{P}$  collapse for all  $Re$  cases. Hence, as in the case of *DE*, probability functions  $\tilde{P}$  of *SL* segments are insensitive to  $Re$  as well. This is true for both segment groups whereas the far-tail decaying exponent is somewhat higher for the negative segments. Another difference between the two segment groups is seen with respect to the peak value of  $P$  which is larger and slightly shifted away from the wall for negative segments.

To investigate the influence of the wall distance, we split the channel in five equidistant wall-normal layers as before. Again,  $P$  and  $\tilde{P}$  of positive and negative segments are plotted for different  $Re$  (figure 7.6).

The curves of unscaled *pdfs* show the strong influence of the wall-normal distance  $y$ . Approaching the wall, *pdfs* become narrower while moving towards smaller element sizes. After normalizing with  $\ell_m$  of the respective wall-normal layer the *pdfs* of the linear scaling range  $0.2 < y/h < 0.8$



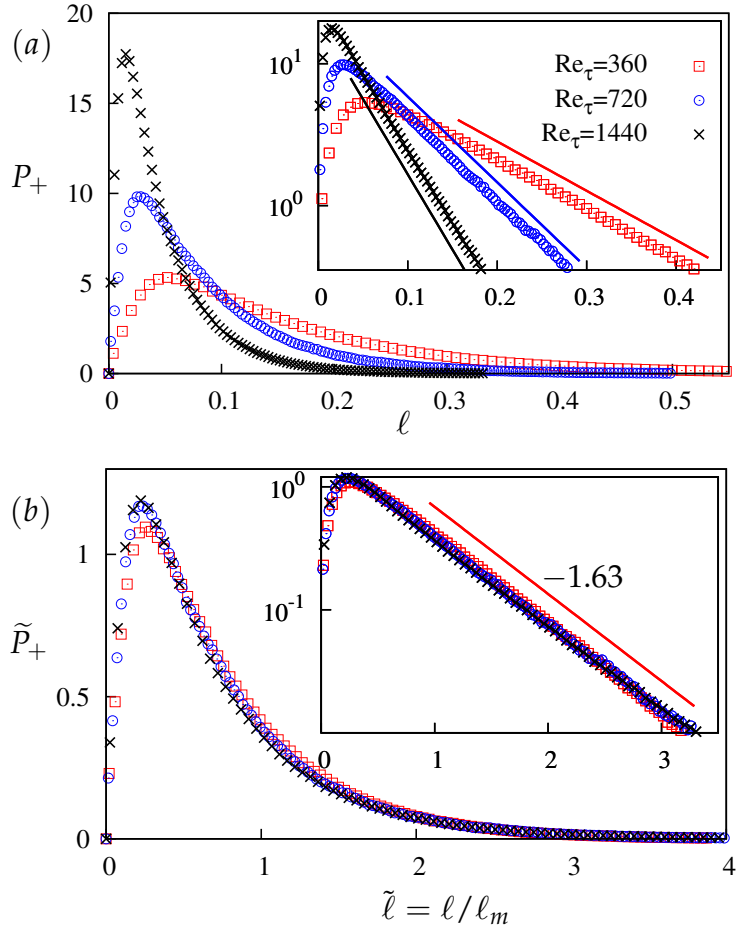


Figure 7.4: Overall *pdfs* of positive segment length for different  $Re$ . (a)  $\ell$  is not normalized while in (b)  $\ell$  is normalized with  $\ell_m$ .

collapse despite some minor deviations. This outcome is also analogous to the findings from *DE* analysis.

In section §6.1.3, we showed that the *pdf* of *DE* length obeys the log-normal distribution. Considering the similarity between both length scales, it can be assumed that the distribution of *SL* segment length may satisfy the log-normal distribution function as well (see equation 6.30). Both shape parameters have been adjusted to account for the variation of the wall-normal distance  $y$  such that  $\sigma = 0.92$  and  $\mu = 0.26 \ln(1.4 \cdot 10^{-5} y/h)$ . As in the *DE* case,  $\sigma$  is nearly constant whereas  $\mu$  is a function of  $y$ .

In figure 7.7, *pdfs* of wall-normal layers, where linear scaling is observed, are displayed exemplarily for  $Re_\tau = 1440$  alongside with the adapted log-

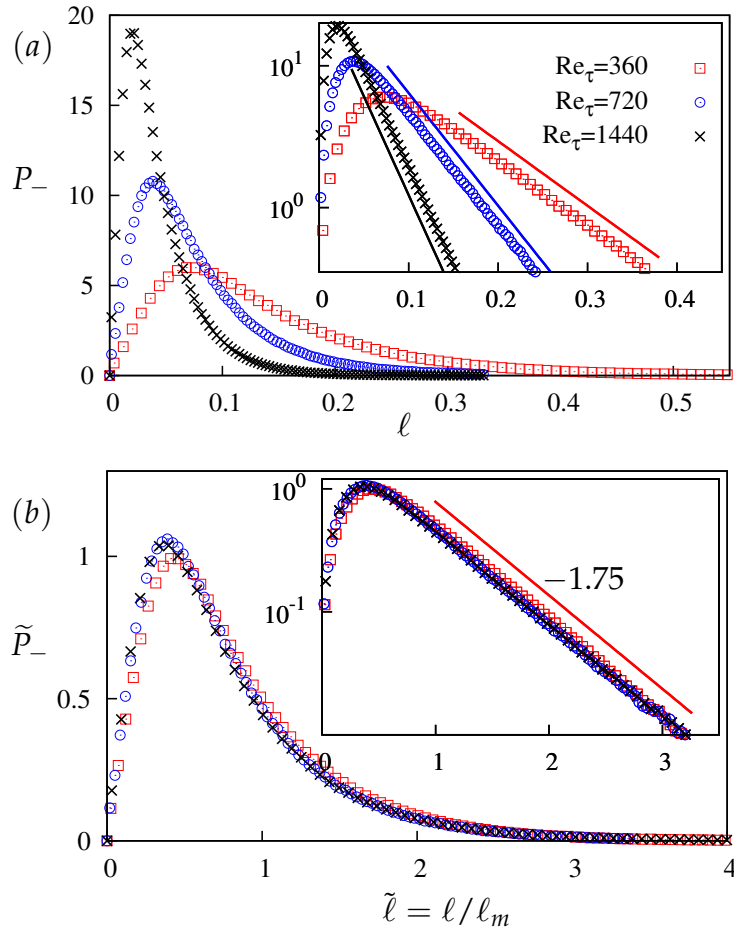


Figure 7.5: Same as in 7.4, but for negative segments.

normal *pdf* fits. It can be seen that, despite minor deviations, the *pdfs* are approximated satisfactorily for positive and negative segment length.

### 7.3 Conditional Mean Velocity Differences

Unlike gradient trajectories with positive definite scalar differences between their extremal points, velocity difference between the bounding points of *SL* segments can be positive or negative corresponding to the sign of the derivative  $\partial U_m / \partial s$ . Velocity differences conditioned on the segment length  $l$  are analyzed for both segment groups in different wall-normal layers as depicted in figure 7.8. Three *Re* are represented. Upper

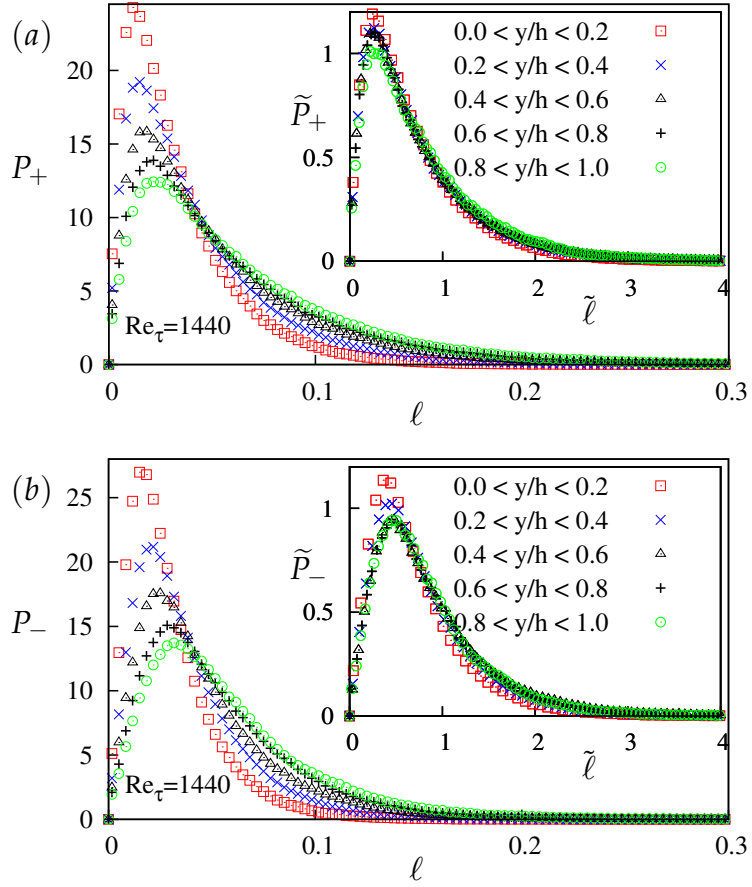


Figure 7.6: Pdfs for wall-normal layers at  $Re_\tau = 1440$ ; (a) positive, (b) negative segments.

parts of the pictures show positive segments while negative segments are seen in the lower parts.

First thing to be noted is that the profiles possess a distinct non-symmetry with regard to different segment groups although the shapes are similar. In all cases, the velocity differences show a linear behavior for large segments ( $\sim \ell_m$ ). Thereby, the mean velocity differences are larger for negative segments than for positive segments which is highlighted by the mean slopes of the curves. The numbers represent the slopes in the first near-wall ( $0 < y/h < 0.2$ ) and the central core ( $0.8 < y/h < 1$ ) regions. Near the wall, the mean slope of negative segments is approximately 35% larger at  $Re_\tau = 720$  and 29% larger in  $Re_\tau = 1440$  case. This discrepancy is even more intense in the central core of the channel where the respective values

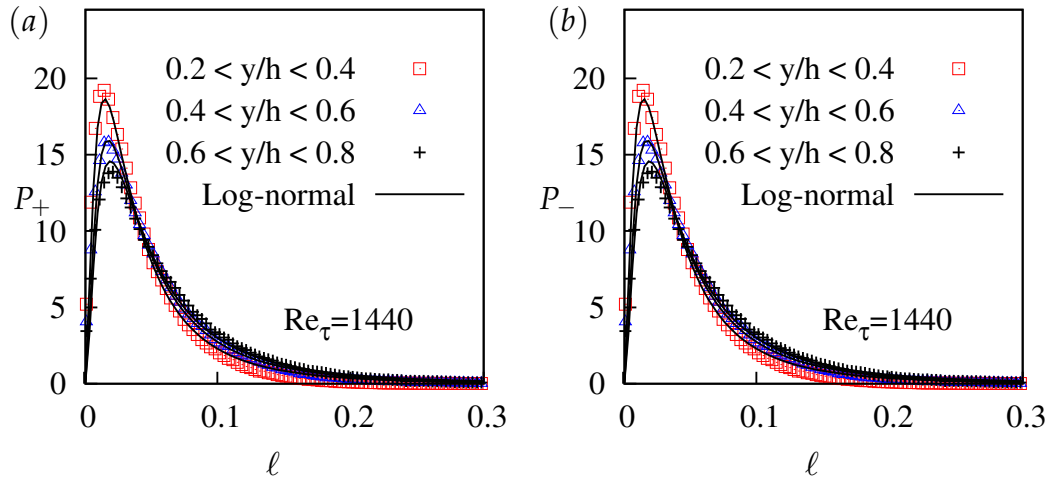


Figure 7.7: Pdfs of positive and negative segment length approximated with the log-normal distribution.

are 40% and 38%. This non-symmetric behavior can be seen as manifestation of a negative skewness of the conditioned velocity differences in the present turbulent flow regime.

It can be added that in layers close to the wall, velocity differences are larger as observed for DEs as well. Furthermore, the linear profiles of the conditional pdfs reveal that  $\Delta U_m$  is larger for large elements.

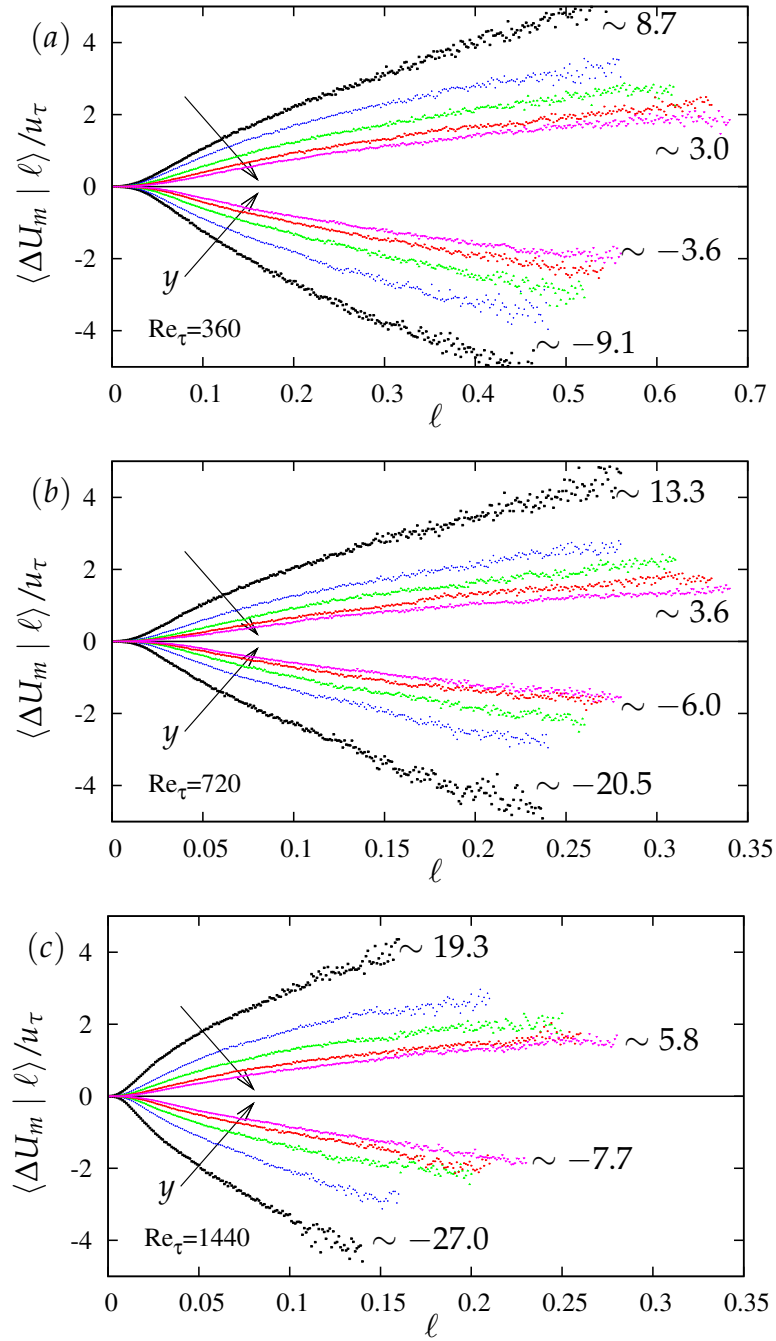


Figure 7.8: Conditional mean velocity differences normalized on  $u_\tau$  in wall-normal layers (direction indicated by arrows) for positive and negative segments. The numbers represent mean slopes of the curves in near-wall and central core regions.

## 8 Summary

The geometrical structure of turbulence in several turbulent channel flows employing the dissipation element approach has been investigated. Therefore, DNS data covering a relatively broad Reynolds number range is analyzed. The clear influence of solid walls at rest on the *DE* statistics has been demonstrated. On this note, it could be shown that in the presence of walls *DE pdf*, *DE* length  $\ell$  and the number of created elements are strongly coupled to the wall-normal distance  $y$ . In order to allow a deeper insight, we examined *pdfs* with ( $\tilde{P}$ ) and without ( $P$ ) rescaling. It is revealed that, particularly in the latter case, distinct deviations with respect to the wall distance can be observed, whereas rescaling the *pdfs* leads to a collapse of the *pdfs* at least for the outer flow regions. Near the wall, however, the similarity is broken due to strong anisotropy. Consequently, the number and the length of *DEs* are found to be functions of  $y$ .

This distinct behavior has been analyzed by Lie symmetry group methods together with known symmetries of Navier-Stokes equations and utilized for the core region of the flow, i.e. the flow region beyond the buffer layer. Therein, the *pdf* of the *DE* distribution exhibits an invariant functional form, in other words, self-similar behavior with respect to the wall distance. This is further enhanced by the scaling behavior of the mean *DE* length scale, which evidences a linear scaling with the wall distance. We outlined the relationship between *DE* and other classical length scales and found that *DE* length is proportional to the Taylor length scale for the core region of the channel.

Furthermore, the relations between *DE* statistics and the Reynolds number  $Re$  as well as the choice of the scalar variable  $\phi$  were analyzed. If rescaled, i.e.  $\tilde{P}$ , the *pdfs* show no dependency on both  $Re$  and  $\phi$  and hence exhibit an isotropic character. This is in strong contrast to classical Kolmogorov scaling laws which usually exhibit a strong dependence on shear and anisotropy. Both usually limit the range of the scaling law.

Contrarily, without rescaling, due to different number of produced elements in different scalar fields, the *DE* length and *pdf* are very sensitive to the choice of  $\phi$ . This is also true for the choice of  $Re$ . Utilizing a geomet-

ric analogy, a relation between the number of  $DE$ , on the one hand, and  $y$ ,  $Re$  and  $\phi$ , on the other hand, has been formulated and validated with the statistics from DNS data. In addition to this, analytical relations for the mean length of the  $DEs$  as functions of  $y$ ,  $Re$  and  $\phi$  were derived which are used to formulate a  $pdf$  model.

It could be shown that the  $pdfs$  of the  $DE$  length are essentially log-normal and derived a  $pdf$  model based on the log-normal distribution. Its shape parameters have been adjusted for the scalar fields  $k$  and  $u$  so that the model is a function of the wall-normal distance  $y/h$  and the Reynolds number. In conclusion, for the conditional mean scalar differences between the extremal points of  $DE$ , it could be shown that in the center regions of the channel Kolmogorov's  $2/3$  hypothesis holds, whereas layers close to wall feature a logarithmic law rather than a power law. However, scalar differences of the velocity components show noticeable deviations. Within these components, the transversal velocity differences are somewhat closer to  $1/3$  than the streamwise velocity.

It is known that flows are sensitive to rotation and transpiration effects. To better understand their influence, three turbulent Poiseuille flow regimes have been investigated in terms of  $DEs$ . The modifications include rotation in streamwise and wall-normal directions as well as vertical wall transpiration.

In the case of wall-normal rotating channel, the induced non-zero spanwise velocity strongly affects the flow statistics which becomes more obvious for higher rotation rates where laminarisation takes place. Interestingly, the self-similar behavior of the  $pdfs$  is still preserved. Also, imposing a spanwise rotation rate was shown to influence the flow characteristics. In this case, the profiles of the mean length appear to be extremely irregular as a consequence of which  $pdfs$  of the  $DE$  length are no longer self-similar. As the last modification, turbulent channel flow with wall transpiration has been studied. Different from previous cases, wall transpiration breaks the symmetry of the flow statistics with respect to the channel centerline as expected. Except for the near-wall regions, the size of the  $DE$  length scales is shown to increase linearly towards the suction side where the turbulence intensity is damped. Owing to this fact,  $pdfs$  of the  $DE$  length are self-similar. In the same region, the number of the  $DEs$  exhibits an exponential decay.

Furthermore, streamline segments have been analyzed based on their curvilinear length and the difference of the velocity magnitude between the ending points. It could be shown that in general mean segments length has

a similar characteristic as that of *DEs* with regard to both the wall-normal direction and *Re* variation. A linear scaling range between the near-wall and central core regions is observed. The slope of  $\ell_m$  in this region decreases when *Re* is increased. Hence, segments are shorter in higher *Re* case. The self-similar behavior of the marginal *pdfs* is also proven for *SL* segments which is well approximated by the log-normal probability distribution. Finally, velocity scalar differences conditioned on  $\ell$  have been examined. It is found that  $\langle \Delta U_m | \ell \rangle$  scales linearly with segment length  $\ell$  for large segments. The profiles are notably asymmetric for positive and negative segments, whereas the mean slope of the velocity difference increases towards the wall.

The streamline segment analysis could be applied to any vector field such as the vorticity field. In an analogous manner, vorticity vector field defined as the curl of the velocity vector  $\mathbf{U}$  would be analyzed by dividing vortex lines into vortex segments.



## A Lie theory for dissipation elements in wall-bounded shear flows

The starting point of Lie symmetry analysis is based on the two groups in the near-wall region of a turbulent channel flow, i.e.

1. scaling group (6.6)  $y^* = e^{a_1}y$  which in operator form writes

$$X_1 = y \frac{\partial}{\partial y} \quad (\text{A.1})$$

2. translation group (6.8)  $y^* = y + a_3$  having the operator form

$$X_2 = \frac{\partial}{\partial y}. \quad (\text{A.2})$$

The scaling group (A.1) together with (6.12) we may directly extend to the scaling symmetry for the *DE* which yields

$$X^{(l)} = y \frac{\partial}{\partial y} + l \frac{\partial}{\partial l} + l_m \frac{\partial}{\partial l_m}. \quad (\text{A.3})$$

For the *DE pdf* the scaling group is unknown and hence we may only assume a very general scaling group

$$X^{(P)} = nP \frac{\partial}{\partial P}. \quad (\text{A.4})$$

where  $n$  is to be specified subsequently.

Since Lie symmetries in infinitesimal form constitute a linear vector space we have the combined symmetry

$$X = c_1 X^{(l)} + c_2 X_2 + c_P X^{(P)} \quad (\text{A.5})$$

where  $c_1$ ,  $c_2$  and  $c_P$  are arbitrary constants.

The determination of  $n$  may in fact be done by applying the latter invariance group to the normalization equation (6.10), i.e.

$$X \left[ \int_0^\infty P dl - 1 \right] \Big|_{\text{eqn. (6.10)}} = 0. \quad (\text{A.6})$$

From (A.2)-(A.5) we see that only the second part of  $X^{(l)}$  and the group  $X^{(P)}$  is actively operating on (A.6). With this we get

$$c_P = -c_1 \quad (\text{A.7})$$

and hence, we obtain together with (A.5)

$$X = c_1 \left[ y \frac{\partial}{\partial y} + l \frac{\partial}{\partial l} + l_m \frac{\partial}{\partial l_m} - P \frac{\partial}{\partial P} \right] + c_2 \frac{\partial}{\partial y}. \quad (\text{A.8})$$

Though an explicit equation for  $P$  is not known at this point we may still construct invariant solutions. For this we apply  $X$  to the a priori unknown solution  $P = F(l, y)$

$$X [P - F(l, y)] \Big|_{P-F(l,y)=0} = 0. \quad (\text{A.9})$$

The latter is in fact a hyperbolic equation and its characteristic solution leads to the invariant surface condition in the form

$$\frac{dy}{c_1 y + c_2} = \frac{dl}{c_1 l} = \frac{dP}{-c_1 P}. \quad (\text{A.10})$$

The characteristics are in fact the invariants of the form

$$\tilde{l} = \frac{l}{y+c} \quad \text{and} \quad \tilde{P} = Pl. \quad (\text{A.11})$$

Since invariants may arbitrarily be combined we may rewrite the latter to obtain the central solution (6.17)

$$P = \frac{\tilde{P} \left( \frac{l}{y+c} \right)}{y+c} \quad (\text{A.12})$$

which may also easily extended to the alternative form (6.15) (see Aldudak & Oberlack (2012)).

## B Bibliography

- ALDUDAK, F., OBERLACK, M. (2009): Dissipation element analysis of scalar fields in wall-bounded turbulent flow. *Proceedings of EUROMECH Colloquium 512: Small Scale Turbulence and Related Gradient Statistics*, 9–11.
- ALDUDAK, F., OBERLACK, M. (2012): Dissipation element analysis in turbulent channel flow. *J. Fluid Mech.* 694, 332–351.
- AVSARKISOV, V. S., OBERLACK, M., KHUJADZE, G. (2011): Turbulent Poiseuille Flow with Wall Transpiration: Analytical Study and Direct Numerical Simulation. *Journal of Physics: Conference Series* 318, 2, 022004.
- BARENBLATT, G. I. (1993): Scaling laws for fully developed turbulent shear flows. I - Basic hypotheses and analysis. *J. Fluid Mech.* 248, 513–520.
- BENZI, R., CILIBERTO, S., TRIPICCIONE, R., BAUDET, C., MASSAIOLI, F., SUCCI, S. (1993): Extended self-similarity in turbulent flows. *Phy. Rev. E* 48, 29.
- BRADSHAW, P., HUANG, P. (1995): The law of the wall in turbulent flow. *Proceedings of the Royal Society of London Osborne Reynolds centenary volume*, 165–188.
- CHOI, H., MOIN, P. (1994): Effects of the Computational Time Step on Numerical Solutions of Turbulent Flow. *J. Comp. Phys.* 113, 14.
- CHONG, M., SORIA, J., PERRY, A., CHACIN, J., CANTWELL, B., NA, Y. (1998): Turbulence structures of wall-bounded shear flows found using DNS data. *J. Fluid Mech.* 357, 225–247.
- CORRSIN, S. (1951): On the spectrum of isotropic temperature fluctuations in isotropic turbulence. *J. Appl. Phys.* 22, 469–473.
- DEAN, R. (1978): Reynolds number dependence of skin friction and other bulk flow variables in two-dimensional rectangular duct flow. *ASME J. Fluids Eng.* 100, 215–222.

- FRISCH, U. (1995): *Turbulence: The Legacy of AN Kolmogorov*. Cambridge University Press.
- GIBSON, C. H. (1968): Fine structure of scalar fields mixed by turbulence I. Zero gradient points and minimal gradient surfaces. *Phys. Fluids* 11, 2305–2315.
- HOYAS, S., JIMÉNEZ, J. (2006): Scaling of the velocity fluctuations in turbulent channels up to  $Re_\tau = 2003$ . *Phys. Fluids* 18, 011702.
- HURST, D., VASSILICOS, J. C. (2007): Scalings and decay of fractal-generated turbulence. *Phys. Fluids* 19, 035103.
- KANEDA, Y., ISHIHARA, T. (2006): High-resolution direct numerical simulation of turbulence. *Journal of Turbulence* 7, 1–17.
- VON KÁRMÁN, T. (1930): Mechanische Aehnlichkeit und Turbulenz. *Nachr. Ges. Wiss. Goettingen, Math. Phys. Klasse* , 58–76.
- KIM, J., MOIN, P., MOSER, R. D. (1987): Turbulence statistics in fully developed channel flow at low Reynolds number. *J. Fluid Mech.* 177, 133.
- KOLMOGOROV, A. N. (1941): The local structure of turbulence in an incompressible viscous fluid for very large Reynolds numbers. *Dokl. Akad. Nauk SSSR* 30, 301–305.
- KOLMOGOROV, A. N. (1962): A refinement of previous hypotheses concerning the local structure of turbulence in a viscous incompressible fluid at high Reynolds number. *J. Fluid Mech.* 13, 82.
- LEKIEN, F., MARSDEN, J. (2005): Tricubic interpolation in three dimensions. *International Journal for Numerical Methods in Engineering* 63, 3, 455–471.
- LUNDBLADH, A., BERLIN, S., SKOTE, M., HILDINGS, C., CHOI, J., KIM, J., HENNINGSON, D. S. (1999): An efficient spectral method for simulation of incompressible flow over a flat plate. Technical Report 1999:11, KTH, Stockholm.
- MEHDIZADEH, A. (2010): *Direct Numerical Simulation, Lie Group Analysis and Modeling of a Turbulent Channel Flow with Wall-normal Rotation*. Ph.D. thesis, TU Darmstadt.
- MEHDIZADEH, A., OBERLACK, M. (2010): Analytical and numerical investigations of laminar and turbulent Poiseuille-Ekman flow at different rotation rates. *Physics of Fluids* 22, 10.

- MOCHIZUKI, S., NIEUWSTADT, F. T. M. (1996): Reynolds-number-dependence of the maximum in the streamwise velocity fluctuations in wall turbulence. *Exps. Fluids* 21, 218–226.
- MOSER, R., KIM, J., MANSOUR, N. (1999): Direct Numerical Simulation of Turbulent Channel Flow up to  $Re_\tau = 590$ . *Phys. Fluids* 11, 943–945.
- OBERLACK, M. (1999): Similarity in non-rotating and rotating turbulent pipe flows. *J. Fluid Mech.* 379, 1–22.
- OBERLACK, M. (2000): Symmetrie, Invarianz und Selbstähnlichkeit in der Turbulenz. *Habilitation thesis, RWTH Aachen* .
- OBERLACK, M. (2001): A unified approach for symmetries in plane parallel turbulent shear flows. *J. Fluid Mech.* 427, 299–328.
- OBERLACK, M., CABOT, W., PETTERSSON REIF, B. A., WELLER, T. (2006): Group analysis, direct numerical simulation and modelling of a turbulent channel flow with streamwise rotation. *J. Fluid Mech.* 562, 383–403.
- OBERLACK, M., ROSTECK, A. (2010): New statistical symmetries of the multi-point equations and its importance for turbulent scaling laws. *Discret. Contin. Dyn. S Series S* 3(3), 451–471.
- OBUKHOV, A. (1949): Pressure fluctuations in a turbulent flow. *Dokl. Akad. Nauk SSSR, Ser. Geojiz.* 3, 49–68.
- ORSZAG, S., PATTERSON, G. (1972): Numerical simulation of three-dimensional homogeneous isotropic turbulence. *Physical Review Letters* 82, (28), 76–79.
- PERRY, A. E., HENBEST, S. M., CHONG, M. S. (1986): A theoretical and experimental study of wall turbulence. *J. Fluid Mech.* 163, 163–199.
- PETERS, N., WANG, L. (2006): Dissipation element analysis of scalar fields in turbulence. *C. R. Mech.* 334, 493–506.
- POPE, S. B. (2000): *Turbulent Flows*. Cambridge University Press.
- RICHARDSON, L. F. (1922): *Weather Prediction by Numerical Process*. Cambridge University Press, Cambridge , xii+236.
- ROGALLO, R. (1981): Numerical experiments in homogeneous turbulence. *NASA TM-81315* .

- ROSTECK, A., OBERLACK, M. (2011): Lie algebra of the symmetries of the multi-point equations in statistical turbulence theory. *J. Nonlinear Math. Phys.* 18, suppl. 1, 251–264.
- SEOUD, R. E., VASSILICOS, J. C. (2007): Dissipation and decay of fractal-generated turbulence. *Phys. Fluids* 19, 105108.
- SHIH, T.-H., LUMLEY, J. L. (1993): Kolmogorov behavior of near-wall turbulence and its application in turbulence modeling. *Comp. Fluid Dyn.* 1, 43.
- SKOTE, M. (2001): *Studies of turbulent boundary layer flow through direct numerical simulation*. Ph.D. thesis, Royal Institute of Technology, Stockholm, Sweden.
- THEODORSEN, T. (1952): Mechanism of turbulence. In Proc. 2nd Midwestern Conf. on Fluid Mech. *Columbus, Ohio: Ohio State Univ.*, 17–19.
- TOMKINS, C. D., ADRIAN, R. J. (2003): Spanwise structure and scale growth in turbulent boundary layers. *J. Fluid Mech* 490, 37–74.
- ÜNAL, G. (1994): Application of equivalence transformations to inertial subrange of turbulence. *Lie Groups and their Applications* 1(1), 232–240.
- VIGDOROVICH, I., OBERLACK, M. (2008): Analytical study of turbulent Poiseuille flow with wall transpiration. *Phys. Fluids* 20, 55102–1–055102–9.
- WANG, L. (2010): On properties of fluid turbulence along streamlines. *Journal of Fluid Mechanics* 648, 183–203.
- WANG, L., PETERS, N. (2006): The length scale distribution function of the distance between extremal points in passive scalar turbulence. *J. Fluid Mech.* 554, 457–475.
- WANG, L., PETERS, N. (2008): Length-scale distribution functions and conditional means for various fields in turbulence. *J. Fluid Mech.* 608, 113–138.
- WELLER, T. (2007): *Lie Group Analysis, Direct Numerical Simulation and Wavelet Analysis of a Turbulent Channel Flow Rotating about the Streamwise Direction*. Ph.D. thesis, TU Darmstadt.
- WELLER, T., OBERLACK, M. (2006): DNS of a Turbulent Channel Flow with Streamwise Rotation - Investigation on the Cross Flow Phenomena. Springer Netherlands, 241–248.

- WRAY, A. A., HUNT, J. C. R. (1990): Algorithms for Classification of Turbulent Structures. *Topological Fluid Mechanics*, ed. by H. K. Moffat and A. Tsinober, Cambridge University Press, Cambridge, 95–104.
- YEUNG, P. K., POPE, S. B. (1989): Lagrangian statistics from direct numerical simulations of isotropic turbulence. *J. Fluid Mech.* 207, 531–586.
- ZAGAROLA, M. V., PERRY, A. E., SMITS, A. J. (1997): Scaling laws for fully developed turbulent shear flows. I - Basic hypotheses and analysis. *Physics of Fluids* 9(7), 2094–2100.

# CURRICULUM VITAE

**Fettah ALDUDAK**

PLACE OF BIRTH: Çermik, Turkey

EDUCATION:

08/07 -02/12

**PhD student**

Chair of Fluid Dynamics

Department of Mechanical Engineering

Technische Universität Darmstadt, Germany

10/99 -03/07

**Diplom Studies (Dipl.-Ing.)**

Department of Mechanical Engineering

Technische Universität Darmstadt, Germany

**Diploma thesis** (10/06 -03/07)

Fluid Mechanics and Aerodynamics

Department of Mechanical Engineering

Technische Universität Darmstadt, Germany

**Bachelor thesis** (09/04 -01/05)

CFD Lab, Department of Mechanical Engineering

University of California, Santa Barbara, USA

08/96 -06/99

**High school, Abitur**

Landgraf-Ludwig-Gymnasium

Gießen, Germany